

**ULTRASOUND STIMULATED HEXAGONAL BORON NITRIDES AS
CANCER DRUG NANOCARRIERS**

by
NİLAY ÇİÇEK

Submitted to the Graduate School of Engineering and Natural Sciences
in partial fulfilment of
the requirements for the degree of Master of Science

Sabancı University
January 2023

NİLAY ÇİÇEK 2023 ©

All Rights Reserved

ABSTRACT

ULTRASOUND STIMULATED HEXAGONAL BORON NITRIDES AS CANCER DRUG NANOCARRIERS

NILAY ÇİÇEK

MOLECULAR BIOLOGY, GENETICS AND BIOENGINEERING

M.Sc. THESIS, January 2023

Thesis Supervisors: Prof. Dr. FAZİLET VARDAR SUKAN
Dr. HÜLYA YILMAZ

Keywords: piezoelectricity, hexagonal boron nitride, drug loading, drug release, ultrasound stimulation, prostate cancer

Electrical stimulation, known to play an important role in cellular physiology, is widely used in therapeutic applications including cancer therapy and regenerative medicine. However, use of cables and electrodes causes difficulties in real life applications. Piezoelectric nanomaterials (NMs) can be used to generate electrical stimulation in a targeted manner through ultrasound (US) waves. Hexagonal boron nitrides (hBNs) are considered biocompatible NMs with their low toxicity and slow degradation profiles in aqueous media. Although it is not clear, one of their degradation products is thought to be boric acid (BA) with a therapeutic effect. With these features, hBNs are considered as good nanocarriers. In this thesis, hBNs were first synthesized by Chemical Vapor Deposition (CVD) and characterized using imaging, spectroscopic and thermal techniques. Then, their piezoelectric properties were investigated by Piezoresponse Force Microscopy (PRFM). Next, the loading efficiency and release of a chemotherapeutic drug, doxorubicin (Dox), at varying pHs and incubation times, and US exposure were evaluated. Finally, the influence of piezoelectricity of hBNs on its drug carrier potential was tested *in vitro* using PC3 human prostate cancer and PNT1A normal adult prostate epithelial cell lines. It was found that the US-induced hBN-Dox significantly inhibited the proliferation of prostate cancer cells. The results of this study suggest that hBNs with the application of US can be a potential drug nanocarrier.

ÖZET

KANSER İLAÇ NANOTAŞIYICILARI OLARAK ULTRASES İLE UYARILMIŞ HEGZAGONAL BOR NİTRÜRLER

NİLAY ÇİÇEK

MOLEKÜLER BİYOLOJİ, GENETİK VE BİYOMÜHENDİSLİK
YÜKSEK LİSANS TEZİ, MAYIS 2022

Tez Danışmanları: Prof. Dr. FAZİLET VARDAR SUKAN
Dr. HÜLYA YILMAZ

Anahtar Kelimeler: piezoelektriklik, hegzagonal bor nitrür, ilaç yüklenmesi,
ilaç salınımı, ultrases uyarımı, prostat kanseri

HücreSEL fizyolojide önemli bir rol oynadığı bilinen elektriksel uyarım, kanser tedavisi ve rejeneratif tıp olmak üzere terapötik uygulamalarda yaygın olarak kullanılmaktadır. Ancak gerçek hayattaki uygulamalarda, kablo ve elektrot kullanımı zorluklara neden olmaktadır. Piezoelektrik nanomalzemeler (NM'ler), kablo ve elektrot kullanımına gerek olmadan ultrases (US) dalgaları gibi hedeflenen şekilde elektriksel uyarım oluşturmak için kullanılabilir. Hegzagonal bor nitrürler (hBN'ler), düşük toksisiteli ve sulu ortamlarda yavaş bozunma profilleri ile biyouyumlu NM'ler olarak kabul edilmektedir. Kesin olmamakla birlikte hBN'nin bozunma ürünlerinden birinin borik asit (BA) olduğu düşünülmektedir. Bu özellikleri ile hBN'ler iyi nanotaşıyıcılar olarak kabul edilir. Bu tezde, hBN'ler ilk olarak Kimyasal Buhar Biriktirme (CVD) tekniği ile sentezlenmiş ve görüntüleme, spektroskopik ve termal teknikleri kullanılarak karakterize edilmiştir. Daha sonra piezo tepki kuvvet mikroskobu (PRFM) ile piezoelektrik özellikleri incelenmiştir. Ardından kemoterapötik bir ilaç olan doksorubisinin (Dox) yükleme etkinliği ve salınımı, değişen pH'larda ve inkübasyon sürelerinde ve US maruziyetiyle değerlendirilmiştir. İlaç taşıyıcı sistemi olarak kullanılan piezoelektrik hBN'lerin, US ile aktive edilerek hem PC3 insan prostat kanseri hem de PNT1A normal yetişkin prostat epitel hücre hatları üzerine etkisi *in vitro* olarak test edilmiştir. US ile hBN-Dox'un prostat kanseri hücrelerinin proliferasyonunu önemli ölçüde inhibe ettiği bulunmuştur. Bu sonuçlar, US uygulaması ile hBN'lerin potansiyel bir ilaç nanotaşıyıcısı olabileceğini düşündürmektedir.

ACKNOWLEDGEMENTS

First and foremost, I would like to express my gratitude to Prof. Dr. Mustafa ulha for giving me all of the opportunity to make this work possible. I would like to thank my supervisor Prof. Dr. Fazilet Vardar Sukan for being my supervisor. And I would like to thank Dr. Feray Bakan Mısırlıođlu for being my thesis jury member.

I feel very lucky to be part of a wonderful group. I always felt stronger within my team and never felt alone. I am grateful for my supervisor Dr. Hulya Yılmaz, for her guidance and encouragement throughout my study. I am thankful to Dr. Zehra obandede, for her continuous support though every step of my work. I owe a special thanks to Őevin Adıgzel for being more than just a colleague, always supporting me, being there for me whenever I need. I would like to thank my family from deep in my heart, their belief in me kept my motivation high against all of challenges. Words cannot express my gratitude to my husband. But I still want to thank him for always being by my side.

*To my husband
İdris Çiçek*

TABLE OF CONTENTS

ABSTRACT	iv
ÖZET	v
ACKNOWLEDGEMENTS	vi
TABLE OF CONTENTS.....	viii
LIST OF TABLES	xi
LIST OF FIGURES	xii
LIST OF ABBREVIATIONS	xv
1.INTRODUCTION	1
1.1 Piezoelectricity.....	1
1.1.1 Cancer Treatment	6
1.1.2 Targeting Cancer.....	9
1.2 Piezoelectric NMs.....	12
1.2.1 Hexagonal Boron Nitrides	14
2.MATERIALS & METHODS	16
2.1 Materials	16
2.1.1 Chemicals, Kits and Media Components	16
2.1.2 Equipment.....	17
2.1.3 Cell Lines.....	18
2.2 Methods.....	18
2.2.1 hBNs Synthesis.....	18
2.2.2 Characterization of hBNs and hBN-Dox.....	19
2.2.2.1 High Resolution Transmission electron microscopy (HRTEM).....	19
2.2.2.2 Fourier Transform Infrared Spectroscopy (FTIR)	19
2.2.2.3 X-Ray Diffraction (XRD)	19
2.2.2.4 Thermogravimetric Analysis (TGA)	20
2.2.2.5 Dynamic Light Scattering (DLS).....	20

2.2.2.6	Raman Spectroscopy.....	20
2.2.2.7	UV-Visible Spectroscopy	20
2.2.2.8	Atomic Force Microscopy and Piezoresponse Force Microscopy ..	20
2.2.3	Doxorubicin Loading to hBNs.....	21
2.2.4	Doxorubicin Release from hBN-Dox	21
2.2.5	Degradation of hBNs and hBN-Dox.....	22
2.2.6	Cell Culture.....	22
2.2.7	Ultrasound Exposure and Material Treatment of Cells	22
2.2.8	Cell Viability Assay	23
2.2.9	Reactive Oxygen Species (ROS) Measurement	24
2.2.10	Cellular Uptake.....	24
2.2.11	Intracellular Doxorubicin Amount Detection.....	25
2.2.12	Colony Formation Assay.....	25
2.2.13	Apoptosis and Necrosis Assay	26
2.2.14	Statistical Analysis.....	26
3.	RESULTS & DISCUSSION	27
3.1	Characterization of hBNs and hBN-Dox	27
3.1.1	Characterization of hBNs	27
3.1.1.1	Piezoelectric Properties of hBNs.....	29
3.1.2	Characterization of hBN-Dox.....	31
3.1.2.1	Piezoelectric Properties of hBN-Dox	33
3.1.2.2	Dox Loading Efficiency and Loading Capacity of hBNs.....	35
3.2	Degradation Profile of hBNs	37
3.3	Identification of Dox Release Profile	38
3.4	Cell Viability Analysis	39
3.5	ROS Analysis	44
3.6	Cellular Uptake Analysis.....	46
3.7	Detection of Intracellular Concentration of Doxorubicin	54
3.8	Colony Formation Assay	58

3.9 Identification of Apoptotic and Necrotic Cells	60
4.CONCLUSION AND FUTURE PERSPECTIVES.....	68
BIBLIOGRAPHY	70

LIST OF TABLES

Table 1. US application period on the cells	23
Table 2. Dox loading efficiency and capacity as percentage with increasing loading time intervals	36
Table 3. Calculated concentrations of hBNs and Dox inside obtained hBN-Dox.....	36
Table 4. Results of ICP-OES analysis of hBNs and hBN-Dox demonstrating ppm of released B.....	38
Table 5. Calculated IC50 values of hBNs, hBN-Dox, Dox, BA for PC3 and PNT1A cells according to cellular viability results	44

LIST OF FIGURES

Figure 1. Piezoelectricity in human body	3
Figure 2. Classification of ultrasound.....	4
Figure 3. Applications of piezoelectricity in biomedicine.....	5
Figure 4. Stages of prostate cancer progression.....	7
Figure 5. Classification of chemotherapeutic drugs	8
Figure 6. Hallmarks of cancer	10
Figure 7. Schematic representation of hBNs structure	15
Figure 8. Schematic representation of hBNs synthesis procedure.....	19
Figure 9. Sample preparation for PRFM measurements.....	21
Figure 10. TEM images of hBNs with increasing magnifications.....	27
Figure 11. Characterization of hBNs	29
Figure 12. PRFM measurement results for hBNs	31
Figure 13. Comparative characterization data of hBNs and hBN-Dox	33
Figure 14. PRFM measurement of hBN-Dox	34
Figure 15. Calibration curve of Dox.....	35
Figure 16. Percentage of released Dox from hBN-Dox	39
Figure 17. PC3 cells viability after 24 and 48h incubation with increasing concentration of hBNs, hBN-Dox and Dox, and US exposure	40
Figure 18. PNT1A cells viability after 24 and 48h incubation with increasing concentration of hBNs, hBN-Dox and Dox, and US exposure	42
Figure 19. PC3 cells viability results within 24 and 48h incubation with increasing concentrations of BA and US exposure.....	43
Figure 20. PNT1A cells viability results within 24 and 48h incubation with increasing concentrations of BA with and without US exposure.....	43
Figure 21. Detected ROS % inside PC3 and PNT1A cells	45
Figure 22. Detected ROS % inside PC3 and PNT1A cells in response to BA treatment	46
Figure 23. FSC vs SSC dot plots of cellular uptake analysis of hBNs and hBN-Dox with increasing concentrations by PC3 cells with and without US stimulation for 24h.....	47
Figure 24. Comparison of FSC vs SSC dot plots of cellular uptake analysis of hBNs and	

hBN-Dox with increasing concentrations by PC3 cells with and without US stimulation for 48h.....	48
Figure 25. Cellular uptake analysis results for PC3 cells with increasing concentrations of hBNs and hBN-Doxes	49
Figure 26. FSC vs SSC dot plots of cellular uptake analysis by PNT1A cells treated with increasing concentrations of hBNs and hBN-Dox within 24h time period with and without US stimulation	50
Figure 27. FSC vs SSC dot plots of cellular uptake analysis by PNT1A cells treated with increasing concentrations of hBNs and hBN-Dox within 48h time period with and without US stimulation	51
Figure 28. Cellular uptake analysis results for PNT1A cells with increasing concentrations of hBNs and hBN-Doxes.....	52
Figure 29. pH-dependent zeta potential change of hBNs and hBN-Dox.....	53
Figure 30. Detected of Dox containing cells as percentage. Histograms of hBN-Dox and Dox according to fluorescence signal coming from Dox inside PC3 cells that treated with hBN-Dox and Dox.....	55
Figure 31. Detected of Dox containing cells as percentage. Histograms of hBN-Dox and Dox according to fluorescence signal coming from Dox inside the PNT1A cells that treated with hBN-Dox and Dox.....	57
Figure 32. Results of colony formation assay and calculated colony number % values of hBNs, hBN-Dox and Dox in PC3 cells	59
Figure 33. Results of colony formation assay and calculated colony number % values of hBNs, hBN-Dox and Dox in PNT1A cells.....	60
Figure 34. Results of apoptosis necrosis detection assay on PC3 cell line with increasing doses of hBNs without US stimulation and with US stimulation.....	62
Figure 35. Results of apoptosis necrosis detection assay on PC3 cell line with increasing doses of hBN-Dox without US stimulation and with US stimulation	63
Figure 36. Results of apoptosis necrosis detection assay on PC3 cell line with increasing doses of Dox without US stimulation and with US stimulation.....	64
Figure 37. Results of apoptosis necrosis detection assay on PNT1A cell line with increasing doses of hBNs without US stimulation and with US stimulation	65
Figure 38. Results of apoptosis necrosis detection assay on PNT1A cell line with	

increasing doses of hBN-Dox without US stimulation and with US stimulation..... 66

Figure 39. Results of apoptosis necrosis detection assay on PNT1A cell line with increasing doses of Dox without US stimulation and with US stimulation 67

LIST OF ABBREVIATIONS

° Degree

°C Degree Celsius

2D Two Dimensional

AFM Atomic Force Microscopy

B Boron

BA Boric Acid

CVD Chemical Vapor Deposition

DLS Dynamic Light Scattering

DMEM Dulbecco's Modified Eagle's Medium

Dox Doxorubicin

FBS Fetal Bovine Serum

FTIR Fourier transform infrared

H⁺ Hydrogen Ion

H₃BO₃ Boric Acid

hBN Hexagonal Boron Nitride

hBN-Dox Doxorubicin Loaded Hexagonal Boron Nitride

IC₅₀ Half-Maximal Inhibitory Concentration

kHz Kilohertz

kV Kilovolt

MHz Megahertz

mV Millivolt

N Nitrogen

NH₃ Ammonia

NM Nanomaterial

nm Nanometer

NP Nanoparticle

PBS Phosphate-Buffered Saline

PC3 Human Prostate Cancer Cell Line

PRFM Piezoresponse force microscopy

PNT1A Adult Prostatic Epithelial Cell Line

ROS Reactive Oxygen Species

SiC Silicon Carbide

TEM Transmission Electron Microscopy

TGA Thermogravimetric Analysis

US Ultrasound

WST-8 Water-Soluble Tetrazolium Salt

XRD X-Ray Diffraction

μ Micro

μL Microliter

μL Microliter

μm Micrometer

μM Micromolar

π Pi

1. INTRODUCTION

1.1 Piezoelectricity

Piezoelectricity is the ability of materials including crystals, ceramics and some biological materials such as DNA and proteins to be defined as the production of electricity in response to an applied mechanical stimulation (*direct piezoelectric effect*) and vice-versa (*reverse piezoelectric effect*) (Kapat et al., 2020). The history of piezoelectricity relies on the mid-18th century. The Pyroelectric effect was explained by Carl Linnaeus and Franz Aepinus for the first time. Based on this knowledge, the connection between mechanical stimulation and the electric charge was put forward by René Just Haüy and Antoine César Becquerel, however their experimental efforts proved ineffective. By using the information on the pyroelectric effect, brothers Jacques and Pierre Curie, who were working at the Faculty of Sciences of Paris in 1880 discovered the *direct piezoelectric effect* (Curie & Curie, 1880). However, they could not estimate the *reverse piezoelectric effect*, which is a unique feature of a piezoelectric material that arises from reversibility. *Reverse piezoelectric effect* was theoretically proposed by Lippmann as an application of the electrical field resulting in a deformation of the crystal structure in 1881 (Lippmann, 1881). The deformation results with the polarization with the help of relative movement of positive and negative charge centers without any change on overall charge neutrality (Kapat et al., 2020). Drawing on this knowledge, reverse piezoelectricity was accepted and further investigated by Curies (Curie & Curie, 1881). For many years, piezoelectricity was only used in laboratories for the purpose of research until World War I that used piezoelectricity in sonars. Afterwards, piezoelectricity was employed in a wide variety of areas such as production of high voltage electricity, microscopy at atomic scale by scanning probe microscopes and sound production and detection. Additionally, the reversible nature of piezoelectric materials enable stimulation both electrically and mechanically by creating an advantage for sensing, and energy harvesting systems with the help of different energy sources (Marino et al., 2017). Recently, piezoelectricity and piezoelectric materials were paid attention by scientist for applications in the field of

biomedicine because of the importance of endogenous electric field for biological processes from early embryonic development to tissue regeneration (Burr & Northrop, 1939).

Direct piezoelectric effect arises from the deformation of a piezoelectric material causing asymmetric shift of charges which creates an electric polarization and electricity (Marino, A., et al. 2017), as well as linear interaction between the mechanical and electrical states in a crystalline material with the feature of non-centrosymmetry (Gautschi, 2002). While *direct piezoelectric effect* originates from the tension, shear and compression of the material causing formation of surface charges, *reverse piezoelectric effect* can be defined as an applied external electric field causing material deformation. The actual determinant of the piezoelectricity of a crystal is mainly dependent on symmetry features of unit cells. There are seven types of shapes that exist in unit cells: triclinic, monoclinic, orthorhombic, tetragonal, trigonal, hexagonal and cubic (Ballato, 1995). According to the electric dipole moments formation as well as crystal lattice sites having ions surrounded by asymmetric charge of piezoelectric materials, they can be divided into three main categories: piezoelectric ceramics, piezoelectric polymers, and piezoelectric composites. In addition to them, piezoelectricity can be found in human materials (Shamos & Lavine, 1967). Figure 1 summarizes the piezoelectric materials in the human body. Due to this feature of the tissues, piezoelectricity innates in those tissues aid in disease treatment in biomedicine. Moreover, processes causing reorientation and change in dipole moment that happens upon mechanical stimulation gives piezoelectricity to biological molecules (Lemanov et al., 2002). In recent decades, for emulating the natural materials, piezoelectric materials are used not only to diagnose, therapy of illnesses but also medical devices in biomedicine (Chen-Glasser et al., 2018). In the following section, importance and applications of piezoelectricity in biomedicine is discussed further.

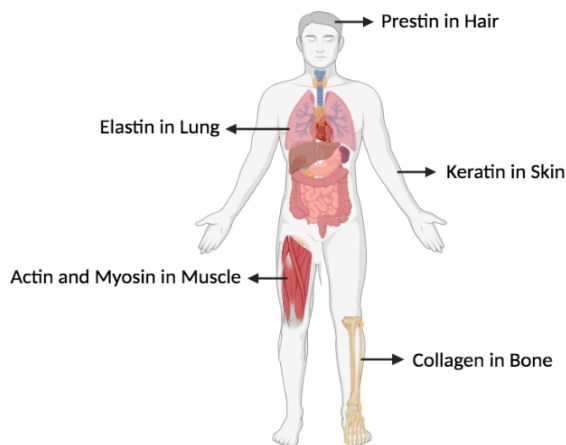


Figure 1. Piezoelectricity in human body

Effect of the endogenous electrical field is critical for various fundamental biological processes including cell migration, chemotaxis, proliferation and differentiation of cells (Marino et al., 2018). For a successful biomedical application employing piezoelectricity, choice of a safe and effective external mechanical stimulant such as *ultrasound (US)* is very critical. US is a kind of sound waves out of human hearing range which has frequency higher than 20 kHz (O'Brien 2007) as shown in Figure 2. Harmless, controllable and targeted as well as safe for operator and patient makes US an excellent tool for biomedical applications as well as proper external stimulant for piezoelectric materials. Frequency of therapeutic US is in the range of 0.5 to 5 MHz (Ter Haar & Coussios, 2007) and penetration of this type of US from the surface of skin reaches up to 15-20 cm into the body. Frequently used strategy in this range of therapeutic US is related to physical effects that are caused by US in cells and tissues such as damage to the cell membrane with different degree of severity ranging from temporary and repairable harm to death for drug and gene delivery (Mitragotri, 2005). These effects are depending on two important factors including frequency and intensity which are caused observable functional changes in proliferation, migration capacity of cells as well as secretion and synthesis (Doan, 1999). While intensity is related to production of heat, higher frequencies support formation of cavitation (Yu et al., 2004).

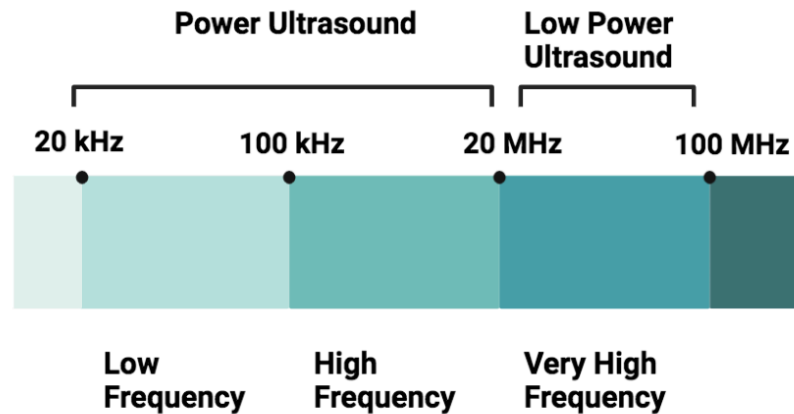


Figure 2. Classification of ultrasound

Even with low-intensity electrical stimulation, antiproliferation of various tumor cell lines can be affected (Janigro, 2006). Another group has shown the influence of low-intensity electrical stimulation on cytoskeletal elements by interfering with the organization of mitotic spindles during cell division (Kirson et al., 2004). Additionally, Stupp et al. indicated that the effectiveness of chemotherapy applied in a clinical trial of glioblastoma treatment increases through low-intensity and low frequency electrical stimulation (Stupp et al., 2015) which has been approved by Food and Drug Administration (Mun et al., 2018).

Proliferation of malignant cells is inhibited more seriously than non-malignant cells with exposure of low-intensity US stimulation by creating an important advantage for therapeutic applications in cancer (Lejbkowitz & Salzberg, 1997). For instance, the US is employed effectively to trigger drug release by stimulating drug delivery vesicles in a desired place for cancer treatment (Mo et al., 2012). In this thesis a potential application for prostate cancer treatment was designed with the help of piezoelectricity activated by US stimulation, therefore in the following section different aspects, challenges and applications in cancer treatment are discussed deeper.

Although as mentioned earlier piezoelectricity used in various bio-applications, traditional methods of electrical stimulation mostly include use of electrodes and wires to take the current from a source to a desired location limiting its potential and practical use by creating a huge challenge for biomedical applications. Piezoelectric materials have the ability to overcome that challenge when they are externally stimulated by a mechanical source due to their feature of electricity production in a wireless and targeted

way. In other words, they can communicate with living systems with this feature. Therefore, they were employed successfully in different biomedical applications including tissue engineering (Bettinger et al., 2009), regenerative medicine (Qian et al., 2012), health monitoring (Mokhtari et al., 2021) and cancer treatment (Marino et al., 2018) which are shown in Figure 3.

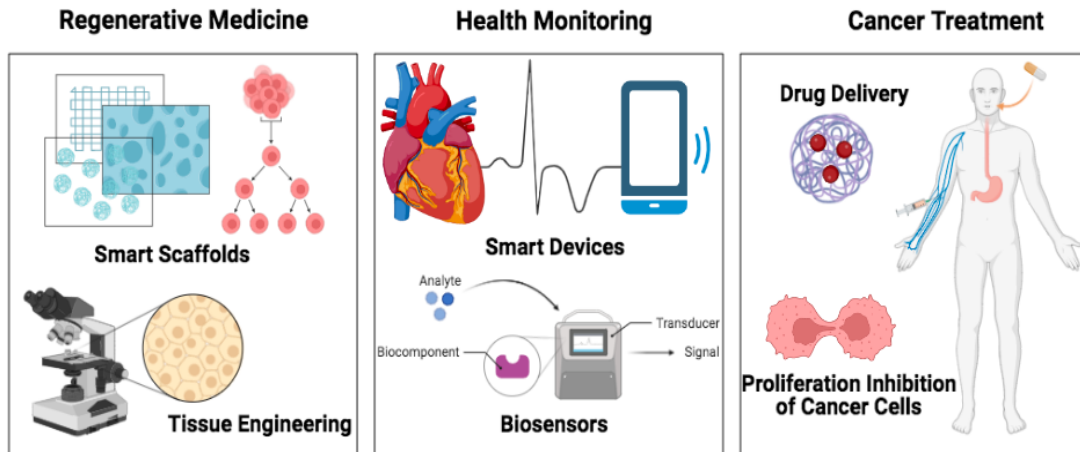


Figure 3. Applications of piezoelectricity in biomedicine

It is known that some type of cells can respond to electrical cues coming from the environment including neurons and muscle cells responding to action potential and contraction. But also, other cell types including fibroblasts, stem cells and cancer cells due to the presence of voltage-sensitive channels have electrical-responsive features (Cafarelli et al., 2021). That feature created an advantage of biomedical applications of piezoelectricity. Also, biological materials that have piezoelectric properties inside the cells such as collagen play a critical role in regeneration allowing their use in piezoelectricity-involved treatment regenerative medicine strategies (Rajabi et al., 2015). In addition to that, piezoelectric materials creating soft, flexible, and stretchable systems can successfully integrate into the piezoelectric devices for sensing, energy harvesting and cell stimulation applications (Salim et al., 2018). This type of material can successfully harvest energy from natural motions of integral organs. Therefore, they can be used as biosensors in biomedical applications as well as as diagnostic tools for different kind of diseases (Kamel, 2022). For instance, Li Su et al. have developed a piezoelectric biosensor for detection of cancer by using lead titanate zirconate ceramic (Su et al., 2013). In the area of cancer, due to the feature of site-specific effect, piezoelectricity is employed

successfully in strategies related to chemotherapy (Marino et al., 2017). Especially as a nanocarrier, piezoelectric materials can work selectively without any damage to healthy tissue and deliver the therapeutic drug easily with reduced off-target effects. Moreover, a stimuli responsive drug release can be achieved by the external mechanical stimulus of piezoelectric material successfully. For instance, ZnO as a piezoelectric material was used as a nanocarrier of paclitaxel to target specifically folate receptors of malignant cells and found useful as increasing anti-tumor efficacy (Puvvada et al., 2015). But still in vivo stability and insufficient loading of cargo creates concerns in the applications. In this thesis, piezoelectricity is employed in a prostate cancer chemotherapy related application. Thus, in the next coming section cancer treatment and prostate cancer were discussed further.

1.1.1 Cancer Treatment

Cancer defined the more than hundred types is one of the most common causes of death in the world (Koo et al., 2021). Several types of cancers such as lung, breast and prostate cancers are the most common types of cancers. The incidence rate for cancers can be relied on age, sex and environmental factors. For instance, the risk of developing age-related cancer is approximately 25% higher in men than in women (Dorak & Karpuzoglu, 2012). While lung, breast and colorectal cancers are caused half of the deaths from the cancer for women, lung, prostate and colorectal cancers are the most common type of cancer in men (Kabir & Donald, 2018). This thesis was focused on prostate cancer.

Prostate cancer is the most common cause of malignancy in men (Siegel et al., 2017). Risk factors in the development of prostate cancer can be summarized as race, family history and old age. With increasing life expectancy over the past few decades, it can be predicted that developing age-related prostate cancer in male will increase (Rawla, 2019). In that regard, understanding characteristics and development of that disease is highly crucial for success in diagnosis and treatment strategies.

Diagnosis of prostate cancer is based on abnormally dividing cells in the prostate gland causing extreme prostate gland growth because of malignancy originating from prostatic intraepithelial neoplasia which can be counted as the first step of malignancy. Localized prostate cancer comes after prostatic intraepithelial neoplasia which represents low grade carcinoma. The development of advanced prostate adenocarcinoma creates local harm and known as high grade carcinoma, finally turns into metastatic prostate cancer (Wang,

2018). Stages of prostate cancer progression are summarized in Figure 4.

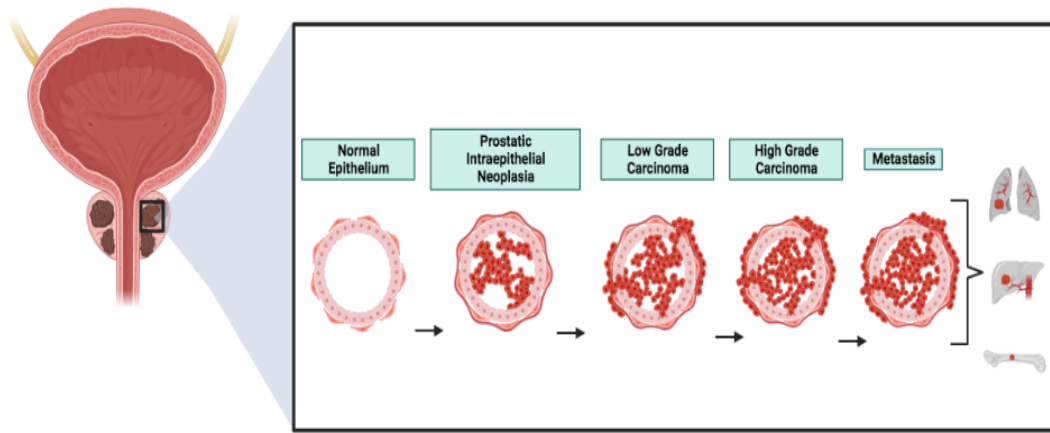


Figure 4. Stages of prostate cancer progression

Surgery, radiotherapy and chemotherapy are the most popular treatment strategies employed in all types of cancer treatment as well as prostate cancer. While surgery and radiotherapy are used for the treatment of local and non-metastatic cancers, chemotherapy is generally used for the types of cancer that have metastatic features. Chemotherapy uses a cytotoxic anti-cancer drug aiming to reduce tumor size by inhibiting division of cancer cells. Traditional chemotherapeutic drugs target mainly DNA, RNA and proteins aiming to impair macromolecular synthesis and function. These drugs can be classified according to their mechanism of action as alkylating drugs, antimetabolites, antitumor antibiotics, topoisomerase inhibitors, anti-microtubule drugs and plant alkaloids as seen in Figure 5 (Amjad et al., 2022). Alkylating drugs work by binding DNA, RNA and proteins, antimetabolites behave like naturally produced metabolites, antitumor antibiotics break DNA, topoisomerase inhibitors hinder DNA replication, anti-microtubule drugs inhibit microtubule production and plant alkaloids inhibit mitosis in by interrupting M phase of cell cycle to eventually prevent cancer cell proliferation.

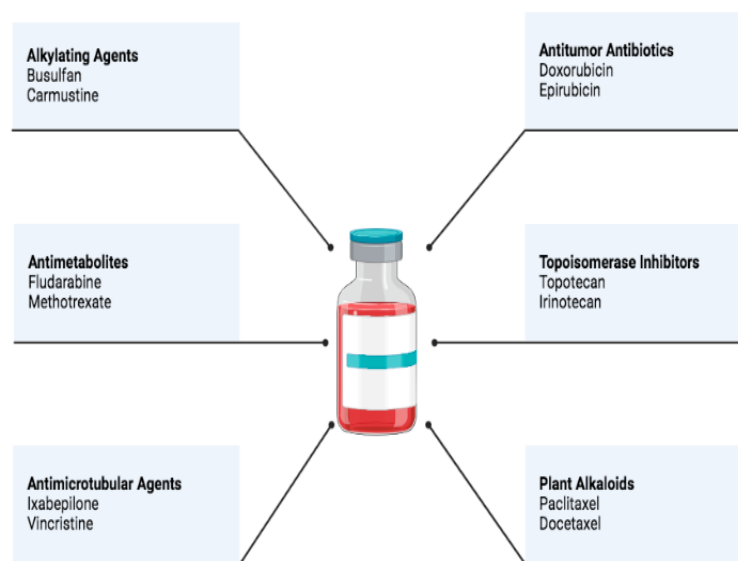


Figure 5. Classification of chemotherapeutic drugs according to their chemical nature and function with their examples

Doxorubicin (Dox) is a widely used chemotherapeutic active pharmaceutical ingredient (API)/drug that hinders tumor growth by triggering cell cycle arrest or apoptosis in the treatment for prostate cancer (SreeHarsha et al., 2019). It mainly prevents working of topoisomerase causing breaks in DNA double helix (Foglesong et al., 1992) and Dox-proteasome complex formation causes a successful accumulation of Dox inside the nucleus that results with cancer cell death (Sahay & Alakhova, 2010). However, it is a feature of causing dose-dependent cardiotoxicity (Frei & Soefje, 2008) and multidrug resistance (Goldstein et al., 1989) limit its use in a safe and effective way. Following development of drug resistance, unsuccessful chemotherapy rate reaches up to 90 %. Moreover, it causes reactive oxygen species production inside the cells (Keeney et al., 2015). Also, only 40 % of the Dox reaches the targeted site. Not only Dox but also all of the chemotherapeutic agents bring many challenges such as toxicity and side effects on healthy cells including hair follicles, bone marrow and gastrointestinal tract cells due to their non-selective working mechanism (Early Breast Cancer Trialists Collaborative Group, 2005).

Because of the problems related to chemotherapy, many attempts have been done to improve efficiency and decrease side effects (Manocha & Margaritis, 2008). The drug delivery system makes possible the release of the drug to achieve a desired therapeutic response. For this reason, safe and effective delivery and controlled release of loaded drug

on desired side by applying to the body through the different ways are vital. Ideal characteristic of drug delivery systems is to increase bioavailability of the drug. However, traditional drug delivery systems including ointments, capsules, syrups, tablets etc. have poor bioavailability and fluctuations in plasma drug level and are unable to achieve sustained release. In recent years, nano-drug delivery, targeted and smart drug delivery systems using stimuli-responsive and intelligent biomaterials have gained attention to overcome challenges and side effects of chemotherapy (Cheng et al., 2021). For that aim, it is crucial to understand not only drugs and drug carrier systems behavior into the body but also targetable characteristics of cancer cells, tumors and microenvironment. Further, the controlled drug delivery systems are discussed in detail.

1.1.2 Targeting Cancer

Cells that express cancerous features significantly differs from the normal cells. Large and nuclei in different shapes, disorganized arrangement, abnormal overall size with abnormal cell membrane and loss of normal cellular functions are observable features of cancer cells. In addition to these features, to identify cancer cells, we can list acquired features of cancer cells as follows; i) loss of contact inhibition ability by abnormal cell adhesion feature resulting unlimited cell division, ii) non-functional cell cycle check points and/or growth suppressors causing failure to undergo apoptosis, iii) overreaction to growth inducers and decreased responsiveness to growth regulators, iv) no respond to immune reactions, v) abnormal angiogenesis, and vi) immortalization by telomerase activity (Hanahan, D., & Weinberg, R. A. 2011). Tumor development processes were summarized in Figure 6. Cancerous cells life process can be briefed as occur with tumor growth and spread to other parts of body which is followed by metastasis and death (Cerqueira et al., 2015). It should be kept in mind that examining the characteristics of cancer cells alone is not sufficient to fully understand cancer. Because cancer cells do not stand alone to take action (Baghban et al., 2020) They are in a dynamic relationship with the cells and non-cellular elements around them (Baghban et al., 2020).

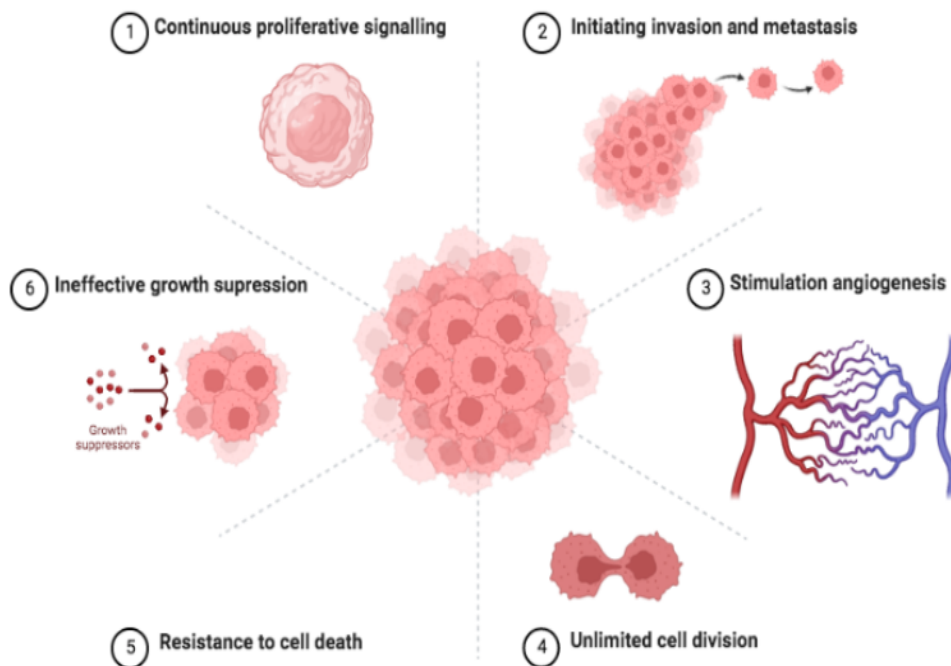


Figure 6. Hallmarks of cancer can be listed under six main categories which occur in tumor development processes as listed. Acquisition of these hallmarks gives a normal cell the feature of tumorigenic and eventually malignant. (Hanahan & Weinberg, 2011).

Tumor formation and development is directly dependent on genetic and epigenetic factors as well as components of tumor microenvironment with a highly dynamic crosstalk (Jahanban-Esfahlan et al., 2017). Tumor cells, immune cells, tumor stromal cells and non-cellular components of extracellular matrix are members of tumor microenvironment. In that complex microenvironment, tumor cells work like a brain to govern every cellular and noncellular elements for their benefit. As a rapidly growing mass, tumors need excessive amount of oxygen and nutrition for counterbalance of bioenergetic and biosynthetic requirements. These actions require complex signaling networks that results with some targetable characteristics of tumor microenvironment in treatment strategies such as acidity. Basically, comparing the healthy cells with malignant cells, acidity of tumor microenvironment arises from the increased cell proliferation. This effect results with an increase in the rate of glucose uptake causing an increase in lactate and H^+ production when cell proliferation rate increases (Swietach et al., 2014).

Aerobic glycolysis in cancer cells differs significantly from healthy cells. Because of the almost 90 % of the produced pyruvate is used for the conversion of lactate and these lactates finally left the cell by going outside of the cell membrane (Gatenby et al., 2004). In addition to that, from the processes of glycolysis, ATP hydrolysis, and glutaminolysis

created H^+ ions left the cell by going outside of the cell membrane. In normal conditions, these accumulated lactates and H^+ ions are balanced with the help of blood circulation making interstitial pH stable (Kallinowski et al., 1989). However; in tumor site because of the formation of abnormal vasculature, blood flow rate becomes insufficient to keep pH at normal level. This makes H^+ ions accumulation inevitable. Also, over produced and accumulated carbonic acid contribute acidity in tumor microenvironment (Tian & Bae, 2012). The acidic tumor microenvironment plays a critical role in repression of immune response to tumor antigens by impairment of healthy extracellular matrix with H^+ ion flow from the tumor area to healthy tissue according to concentration gradient (Estrella et al., 2013). Moreover, it causes tumor volume increase and decrease in uptake of chemotherapeutic drugs. Abnormal vascularization plays other critical roles in addition to contribution of acidity in tumor microenvironment.

In most of the solid tumors, abnormal vascularization causes formation of porous walled vessels as a result of fast development of tumor finalized enhanced permeability and retention effect (Bagherifam et al., 2015). This effect causes easy passage of many macromolecules, lipids and nanoparticles (NPs) up to size around 400 nm and allow their retain in that area longer by the help of the abnormal porous-walled vessels (Torchilin, 2010). From the negative side these features can be counted as only characteristics of cancer, but on the positive side these features can be successfully used in targeted treatment strategies. While acidity indicates a targetable difference between healthy and cancer cells for a treatment strategy, abnormal vascularization and impaired cell membrane feature could be used for benefit of a drug carrier.

Nanomaterials (NMs) have been widely used over the past few decades in biomedical applications with their unique properties, small size and biocompatibility (Hoop et al., 2017). In addition to that, NMs working as drug carrier have important advantages such as targeted effect and on-demand release depend on specific parameters such as pH and temperature (Reinisova et al., 2019). Therefore, use of NMs offers a promising treatment strategy to overcome challenges of conventional chemotherapy by decreasing proliferation of tumor cells and toxic side effects (Cerqueira et al., 2015). However, to create a safe and successful clinical application for cancer treatment, NM-cell interaction must be fully understood. Size, shape, charge, hydrophobicity and surface modification can be listed as physiochemical properties of NMs which are able to affect cellular

internalization as well as nano-bio interface interactions formed between NM and cell membrane (Zhang et al., 2021). NM and cell interaction can be summarized as three important aspects. These are (i) cellular uptake of NM, (ii) intracellular trafficking of the particle and (iii) kinetic properties of cellular and subcellular interactions (Donahue et al., 2019). Cellular uptake efficiency of a NM is highly depending on the size, geometry and charge of the material (Herd et al., 2013). An effective targeted drug delivery approach has ability to increase cellular internalization by a specific strategy designed for targeted area and used carrier. Also, it can decrease acute toxicity and side effect of the drug by a suitable release profile responding a certain stimulus (Yang et al., 2016). Difference between tumor microenvironment and normal physiological pH causes an increase in treatment efficiency when pH responsive drug release systems are employed (Popova et al., 2021). It should be noted that, not only it is enough to understand features of targeted area in the use of a successful nano-sized drug delivery system. But also features of selected nano-carrier must be fully understood with its unique properties. In that regard, NMs which have piezoelectric feature, that was employed as a drug carrier in this thesis, were deeply discussed in the following section.

1.2 Piezoelectric NMs

Piezoelectric NMs have ability to generate electricity when they are exposed a mechanical stimulation or vice versa. They are named as smart NMs because of their ability to respond external stimulus by changing their properties. Piezoelectric NMs can create the electric stimulation successfully with the correct choose of mechanical stimulation strategy to desired place by creating desired effect. Thus, they are found useful for many different fields including space, robotics, energy conversion and medicine (Falconi et al., 2012). Scaling a piezoelectric material into a nanometric size especially for the field of cancer nanomedicine increases the potential of that material by reducing side effects and increasing efficiency with an excellent advantage for targeted and controlled drug release applications (Kapat et al., 2020). Moreover, the nano-sized piezoelectric materials have high surface energy due to its high surface-area-to-volume ratio and high potential to create cell specific-response compared to bulk materials for all kinds of biological

applications (J. Li, et al 2017). In that regard, barium titanate as a scaffold in tissue engineering applications and zinc oxide as an anticancer and antimicrobial have become very popular piezoelectric materials for biomedical applications in recent years (Shuai et al., 2020; Wang, 2004).

Boron nitride NMs such as boron nitride nanotube gained special attention due to their excellent piezoelectricity employed in different applications (Ciofani et al., 2010) can be defined as structural analogue of carbon-based materials. Also similar to carbon, boron nitrides exist in amorphous and crystalline forms (Jedrzejczak-Silicka et al., 2020). Wide variety of nano-sized and carbon-based materials have been used in drug delivery (Zhang et al., 2010), bioimaging (Liu et al., 2009) and biosensing (Heller et al., 2005) applications. Besides their effectiveness, toxicity concerns are still existing. For an ideal biological application, selected NMs must be biocompatible, nonimmunogenic, safe and nontoxic. Compared to them, boron nitride NMs offer higher stability and lower toxicity for biomedical applications due to the feature of superior chemical inertness. Several investigations have been performed that proves safety of boron nitride NMs (Emanet, et al., 2017; Chen et al., 2009; Taskin et al., 2020). It should be noted that a large part of this success of boron nitrides depends on the element boron, which is one of their main elements. It is a semiconductor element that carry both metal and nonmetal features. This element is present in nature in different forms including boric acid (BA), borax, colemanite (Rondanelli et al., 2020). Boron itself is employed in wide variety of areas as biomaterial including implants in joints, pacemaker leads. Investigations have performed related to effect of boron on human health and resulted positively proving its effect of antioxidant, anti-mutagenic, anti-microbial, anti-inflammatory and anticancer (Aydin et al., 2022). In addition to that, it was demonstrated a reducing feature on prostate cancer risk (Zhang et al., 2001; Barranco et al., 2007).

Boron nitride NMs appear in different forms including cubic, hexagonal, wurtzite, and rhombohedral boron nitride form which are are known as electrical insulators. Whereas hexagonal boron nitrides (hBNs) and rhombohedral boron nitrides have denser structure due to the sp^2 hybridized B–N bonds, cubic and wurtzite boron nitrides have more relaxed structure due to the presence of sp^3 hybridized bonds. The most stable form of boron nitride NMs is hBNs at room temperature (Izyumskaya et al., 2017) due to its high

stability. In the following section, hBNs were discussed deeper with its unique features including piezoelectricity.

1.2.1 Hexagonal Boron Nitrides

Structurally, hBNs include alternating boron and nitrogen atoms in a hexagonal basal plane with strong sp^2 hybridized and polarized covalent B-N bonds. (Pacilé et al., 2008). It exhibits a two-dimensional (2D) atomic layered structure (Geim & Novoselov, 2007). These layers are held together by van der Waals interactions which is represented in Figure 7. The biggest difference between hBNs and graphene is the presence of electronegative nitrogen atoms making them strongly polarized and non-centrosymmetric.

hBNs exhibit the feature of electrical insulating (Watanabe et al., 2004), unique mechanical (Hernandez et al., 1998) and high thermal conductivity (Zhi et al., 2009; Zhi et al., 2010). Additionally, in the mid-infrared range, hBNs in room temperature have unique photonics properties with their ability of defect-induced single photon emissions near room temperature (Sajid et al., 2020). Also, hBNs exhibit unique electromechanical properties with the feature of piezoelectricity (Ares et al 2020). hBNs with odd number of layers are thought to be piezoelectric because lack of a center of symmetry is a characteristic feature of piezoelectric materials (Ares et al 2020). With all of these properties, hBNs are popular in the research areas of electrochemical energy storage, photonics, substrates and dielectric layer for 2D devices, thermal applications, anti-corrosion and catalytic application, chemical protection (Roy et al., 2021) and waste treatment (Lu et al., 2013).

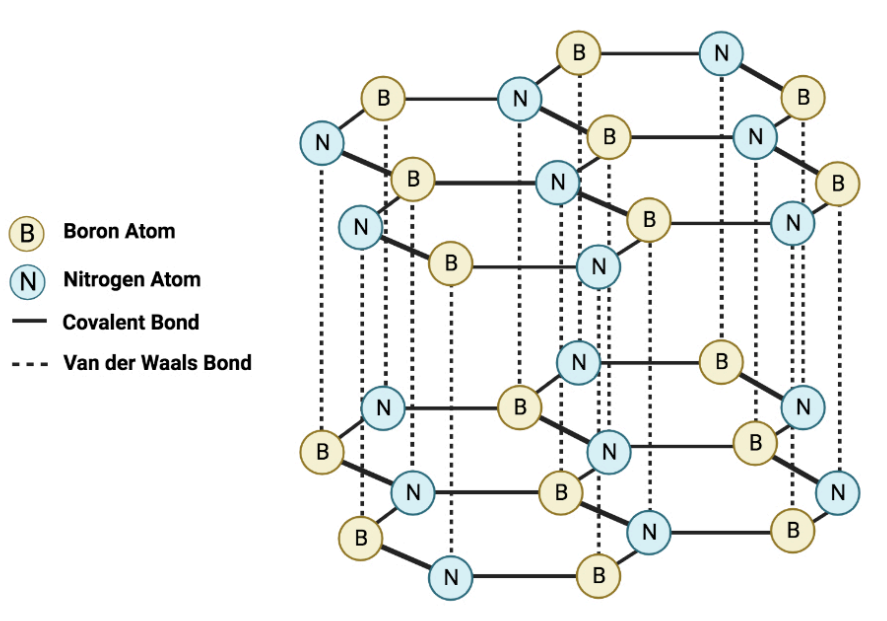


Figure 7. Schematic representation of hBNs structure

hBNs with the features of high surface area, biocompatibility, atomically flat surface and high stability in aqueous solutions are seen as promising tool for biomedical applications such as molecular imaging (Chen et al., 2015) and biological sensors (Lu et al., 2016). Thin 2D structure of hBNs creating high surface area to volume ratio gives them cargo loading ability (Ciofani et al., 2013) for cancer drug delivery and photodynamic therapy (Jedrzejczak-Silicka et al., 2018). Moreover, existing and possible surface interactions of hBNs assist drug delivery to desired site (Cheng et al., 2019). For a successful application, synthesis method of hBNs to obtain different properties including size, layer number of hBNs is the most important and fundamental step. There are two main strategies in the synthesis of hBNs including top-down (Gao et al., 2018) and bottom-up methods (Wang et al., 2019). Top-down processes can be summarized under the two-broad title as mechanical and chemical exfoliations. Top-down methods gives higher possibility in the control of structure size and position of desired NMs (Alexe et al., 2004). But still, this technique can cause high amount of defect in the structure that can cause a decrease in piezoelectric property. On the other hand, bottom-up strategies can create smaller structures with reduced defect amounts and proved as effective in the synthesis of piezoelectric NPs (Jacob et al., 2003). On the other hand, chemical deposition (Eda, et al., 2011), chemical vapor deposition (Shi et al., 2010) and micromechanical cleavage (Li, et al., 2011) can be listed as examples of synthesis strategies of bottom up processes. Chemical vapor deposition (CVD) is a practical bottom-up and useful technique for the

production of high quality, high amount and thin hBNs. Parameters of CVD synthesis method directly affect formation of high quality hBNs. These parameters can be listed as substrate, gas composition, flow rate, and growth temperature. Different types of substrates are employed in the CVD synthesis process to grow hBNs such as copper, nickel, gold, iron and silicon carbide (SiC) (Zhang et al., 2021; Dai et al., 2018).

In this thesis, hBNs were synthesized on SiC substrate to obtain a nanocarrier system by using CVD method, and loaded with Dox, a chemotherapeutic drug, chosen as a model drug. Synthesized hBNs and Dox loaded hBNs (hBN-Dox) were characterized with imaging, spectroscopic and thermal techniques. After the characterization of NMs, piezoelectric features of hBNs and hBN-Dox were comparatively tested using piezoresponse force microscopy (PRFM). Afterwards, release profile of Dox from hBN-Dox and degradation of hBNs and hBN-Dox were identified at varying pHs, incubation times, and US exposure. Finally, potential of US activated piezoelectric hBNs as nanodrug carrier were tested *in vitro* by using human prostate cancer (PC3) and normal adult prostate epithelial cell lines (PNT1A).

2. MATERIALS & METHODS

2.1 Materials

2.1.1 Chemicals, Kits and Media Components

6-Well Plate (ISOLAB, Germany)

96-Well Plate (ISOLAB, Germany)

Ammonia (Sigma Aldrich, USA)

Apoptosis Necrosis Detection Kit (Biolegend, USA)

Boric Acid (Sigma Aldrich, USA)
Crystal Violet (Sigma Aldrich, USA)
DMEM High Glucose (Sigma Aldrich, USA)
DMSO (PanReac AppliChem, Barcelona)
Doxorubicin Hydrochloride (Biosynth, Switzerland)
Falcon Tubes (ISOLAB, Germany)
Fetal Bovine Serum (Sigma Aldrich, USA)
Gluteraldehyde (Merck, USA)
L-Glutamine (Pan Biotech, Germany)
PBS (Pan Biotech, Germany)
Penicillin-Streptomycin (Capricorn Scientific, Germany)
RPMI (Capricorn Scientific, Germany)
Serological Pipettes (ISOLAB, Germany)
Silicon Silicon Carbide Substrate (Civelek Porselen, Turkey)
Tissue Culture Flasks (ISOLAB, Germany)
Triton X-100 (Bioshop, Switzerland)
Tryphan Blue (Pan Biotech, Germany)
Trypsin (Sigma Aldrich, USA)
WST-8 Reagent (Cell Counting Kit-8, CCK-8, Sigma Aldrich, USA)

2.1.2 Equipment

Plate Reader (Bio-Rad, USA)
Ultrasonic Bath (ISOLAB, Germany)
Tubular Furnace (Protherm, PTF 16/50/610, Germany)
Flow Cytometer (BD Biosciences, USA)
UV-Visible Spectrophotometer (Varian, USA)
Light Microscope (Carl Zeiss, Germany)
Incubator (Thermo Scientific, Germany)
Centrifuge (Eppendorf, Germany)
pH Meter (Mettler Toledo, Switzerland)
High Resolution Transmission Electron Microscope (Fei Talos F200S, USA)

Raman Spectrophotometer (Renishaw, UK)

Dynamic Light Scattering (Malvern Panalytical, UK)

Inductively Coupled Plasma Optical Emission Spectrometry (Agilent Technologies, USA)

X-ray Diffractometer (Bruker AXS GmbH, Germany)

Atomic Force Microscope (NanoMagnetics Instruments, UK)

2.1.3 Cell Lines

PNT1A, American Type Culture Collection (ATCC)

PC3, American Type Culture Collection (ATCC)

2.2 Methods

2.2.1 hBNs Synthesis

As seen in Figure 8, 2 gram of boric acid (H_3BO_3) and 3 mL 13.38 M ammonia (NH_3) were mixed. The mixture was spread onto a SiC substrate and NH_3 was evaporated for 20 minutes at 150 °C. Following the evaporation of NH_3 , the SiC plate was placed into center of a tubular furnace. hBNs were synthesized under NH_3 atmosphere at heating rate of 8 °C/min until 1100 °C for 2 hours. When the reaction was completed, the furnace was cooled down at the rate of 8 °C/min until 500 °C and closed. hBNs were collected from onto the SiC plate and stored at room temperature for furthest tests.

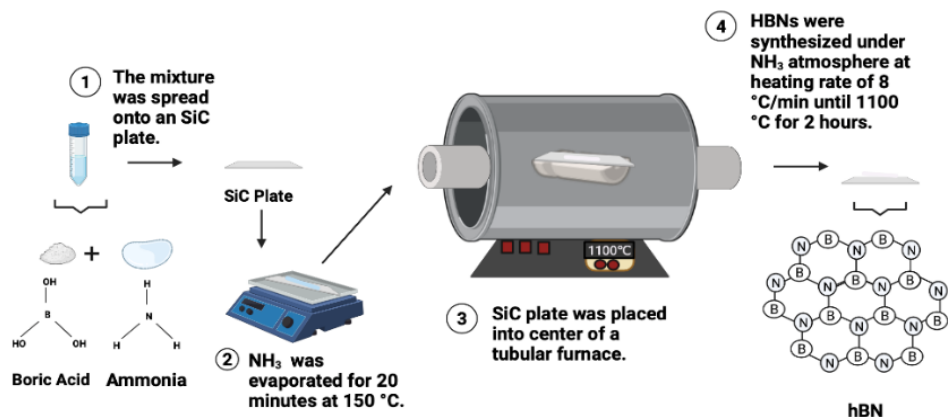


Figure 8. Schematic representation of hBNs synthesis procedure

2.2.2 Characterization of hBNs and hBN-Dox

hBNs and hBN-Dox were characterized using imaging, spectroscopic and thermal techniques

2.2.2.1 High Resolution Transmission electron microscopy (HRTEM)

HRTEM was used to observe size, distribution, and morphology of NMs at an 80 keV accelerated voltage. NMs were analyzed on a carbon-coated copper grid.

2.2.2.2 Fourier Transform Infrared Spectroscopy (FTIR)

Chemical composition of hBNs were characterized by FTIR. All of the NMs analysis was performed in powder form and scanned 20 times with a resolution of 4 cm^{-1} at 600-4000 cm^{-1} region.

2.2.2.3 X-Ray Diffraction (XRD)

Crystal structure of hBNs were assessed by XRD with using $\text{CuK}\alpha$ radiation. Step scanning mode that applies 30 kV voltage and 10 mA tube current. In that mode, the step size was 0.02° and a scan speed was 1 sec per step. The measurement was recorded in the range of $2\theta = 5-90^\circ$.

2.2.2.4 Thermogravimetric Analysis (TGA)

Thermal stability of hBNs was analyzed by TGA. Analysis was performed within argon atmosphere and with heating rate of 10 °C per min up to 800 °C.

2.2.2.5 Dynamic Light Scattering (DLS)

DLS was used for determination of hydrodynamic size and surface charge of hBNs and hBN-Dox. For the DLS measurements, 1 mg of hBNs and hBN-Dox separately dispersed in deionized water (diH₂O)/cell culture media were used.

2.2.2.6 Raman Spectroscopy

Raman spectrum of hBNs was obtained by using 532 nm laser. Analysis was performed with materials in powder form within the region of 100-3200 cm⁻¹. Exposure time and laser power were arranged to 10s and 1, respectively.

2.2.2.7 UV-Visible Spectroscopy

Uv-vis analysis was done for all materials at a range of 200-800 nm. Prior to analysis materials were dispersed with the help of ultrasonic bath within a proper solvent.

2.2.2.8 Atomic Force Microscopy and Piezoresponse Force Microscopy

Topography of hBNs and hBN-Dox was analyzed by AFM. Prior to analysis, 1 mg/mL of hBNs and hBN-Dox were dispersed in deionized water (diH₂O) for 30 min and dropped onto gold-coated silicon wafer. The ability of AFM that measures local piezoelectric response parallel to the information that was obtained from topography was used to measure the piezoelectricity of hBNs and hBN-Dox. This mode of operation with AFM is called as Piezoresponse Force Microscopy (PRFM). Visualization is done with the help of a sharp, conductive probe making a contact with the surface of a piezoelectric material and scanning the surface. To create conductivity between the gold-coated silicon wafer and the magnetic plate, silver paste was used by adhering gold-coated silicon slide to magnetic plate. A multimeter was used to test and prove conductivity. This sample

preparation strategy was shown in Figure 9.

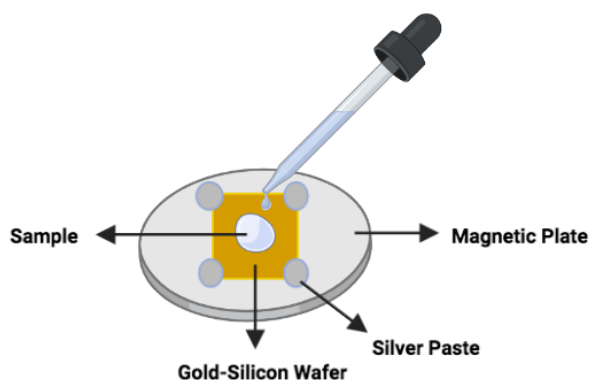


Figure 9. Sample preparation for PRFM measurements

2.2.3 Doxorubicin Loading to hBNs

Dox loading to hBNs was performed at a pH of 7.4 for increasing time to determine the maximum amount of Dox loaded to hBNs. In brief, 0.91mM Dox in 1 mL of 1x PBS was prepared. Then, 10 mg hBNs was added into the Dox solution was stirred at room temperature for 6, 24 and 48h at 500 rpm. Following to the incubation, the dispersion was centrifuged at 10000 rpm for 8 minutes. The precipitate was washed three times with diH₂O and PBS by dispersing in every repeat and all supernatants and precipitate were separately collected for further analysis. Whereas supernatants were used to determine the free Dox amount by UV-vis for calculations of drug loading efficiency and capacity according to intensities of the absorption of free Dox after removal of all hBN-Dox, precipitates were used for the characterization by FTIR and *in vitro* studies.

The standard curve of Dox was derived from the serial dilutions by a customary way by UV-vis at 480 nm. 250 µg/mL Dox solution was diluted to 10, 25, 50, 100 and 125 µg/mL. For all analysis, PBS spectrum was used as a background.

2.2.4 Doxorubicin Release from hBN-Dox

Determination of amount of released Dox from hBN-Dox was performed at different pHs to clarify effect of pH. For the drug release, 1 mg hBN-Dox in 1 mL PBS was dispersed at pH values of 3, 5, 7.4, 9. The dispersions were shaken at 37°C for 6, 24 and 48h at 220

rpm. After incubation, the dispersions were centrifugated at 10000 rpm for 10 min and washed two times. All supernatants were collected for the UV-visible spectrophotometer analysis to determine released free Dox from hBN-Dox.

2.2.5 Degradation of hBNs and hBN-Dox

The degradation profile of hBNs and hBN-Dox upon the different conditions including pH (3, 5, 7.4, 9), time (6, 24 and 48h) and US exposure was assessed by Inductively Coupled Plasma Optical Emission spectroscopy (ICP-OES) technique. Calibration of device was done by multi-element standard stock solution containing (1000 $\mu\text{g} / \text{ml}$) B, Na, Mg, Al, Fe, Sr, Zn, Ca. With this standard stock solution, calibration curve was created for each metal. For the measurements, 1 mg from each sample was weighted and dispersed in 1 mL PBS at pH values of 3, 5, 7.4, 9. The dispersions were shaken at 37°C for 6, 24 and 48h at 220 rpm. When the incubations were completed within designed time period, the dispersions were centrifugated at 10000 rpm and supernatants were collected. Then the collected supernatants were diluted 100 times with 1 % HNO_3 and final volume was 10 mL (margins of error are given as \pm standard deviation, $n = 3$).

2.2.6 Cell Culture

PC3 and PNT1A cells were cultured in Dulbecco's Modified Eagle's Medium (DMEM) with high glucose supplemented with 10 % fetal bovine serum (FBS), 1 % Penicillin Streptomycin (10000 U/mL-10 mg/ml) and 1 % L-Glutamine (2mM). When the cells reached 80 % confluency, they were collected from the flask. Cell culture media was removed, and cells were washed with 1x PBS. Then, 3 mL trypsin/EDTA was added to detach the cells at 37 °C for 5 min. After detachment, cells were collected with cell culture media, and centrifuged at 1500 rpm for 5 min. The flasks are kept in an incubator at 37 °C with 5 % CO_2 and 95 % air in a humidified atmosphere.

2.2.7 Ultrasound Exposure and Material Treatment of Cells

US applications were carried out with the frequency of 37 kHz, 240 Watt and 100 % power using ultrasonic bath at room temperature. Duration of each exposure was 10 s by direct placing of well plate into the ultrasonic bath. As seen on the Table 1, cells were

exposed to US one time for 6h cells incubation, 4 times for 24h cells incubation, 8 times for 48h cells incubation. During US exposure by ultrasonic bath, any temperature change was observed.

Table 1. US application period on the cells

Incubation Time of Cells	US Exposure							
	3h	6h	9h	24h	27h	30h	33h	48h
6h	10 s	X	X	X	X	X	X	X
24h	10 s	10 s	10 s	10 s	X	X	X	X
48h	10 s	10 s	10 s	10 s	10 s	10 s	10 s	10 s

All of the following *in vitro* methods including US exposure and material treatments were followed the same procedure that is explained in that section. Before each material treatment, dispersion of hBNs and hBN-Dox were done by sonication in ultrasonic bath and to achieve final concentration, serial dilution method was employed. hBNs, hBN-Dox and Dox were fresh prepared for the analysis.

2.2.8 Cell Viability Assay

Cell viability was measured to detect the effect of hBNs, hBN-Dox, Dox, and BA (M. Emanet, et al 2017) as a potential degradation product of hBNs with and without US exposure on PC3 and PNT1A cells by WST-8 assay. This assay is based on the amount of formazan dye formed which is directly related to the metabolic activity of cells (Chamchoy, K., et al 2019). The assay was carried out as described in the manufacturer's instructions. Cells were seeded at the density of 5×10^3 cells/well in 96-well plate and incubated for 24h. After that, the cells were treated with increasing concentrations (5, 25, 125, 625 $\mu\text{g/mL}$) of hBNs, hBN-Dox, Dox, BA for 24h and 48h. Following the incubation, the media were removed and replaced with a fresh media containing 5 % WST-8 reagent and incubated for 3h. From each of the wells having 5 % WST-8 reagent, 80 μL was taken and placed in a new 96 well plate to read the absorbance. Percentage of cell viability calculated by the absorbance at 450 nm from plate reader. 10 % DMSO was used as a positive control. Cells without any US exposure or/and treatments were used as

a negative control. The cells viability calculations were performed according to negative control. IC50 values were calculated by nonlinear regression using GraphPad Prism (GraphPad Software, USA).

2.2.9 Reactive Oxygen Species (ROS) Measurement

2',7'-Dichlorodihydrofluorescein diacetate (DCFDA) which is cell a permanent reagent was used to detect formation of reactive oxygen species (ROS) after treatment of hBNs, hBN-Dox, Dox and BA with and without US exposure to the cells. To conduct experiment, PC3 and PNT1A cells were seeded in 96-well plates with a density of 5×10^3 cells/well. After overnight incubation, cells were treated with increasing concentrations (5, 25, 125, 625 $\mu\text{g}/\text{mL}$) of hBNs, hBN-Dox, Dox and BA and while control groups did not get any US exposure, other groups treated as shown in Table 1. Material treatments and US exposure were completed in 24h period. Following that, cell culture media were removed, and cells were washed with PBS. DCFDA was given to the each well with concentration of 10 μM per mL in a final volume of 100 μL . And then plates were incubated at 37 °C and 5 % CO_2 for 45 min. At the end of this period, results were taken from microplate reader by taking absorbance of every tested well at excitation of 485 nm and emission of 535 nm wavelengths.

2.2.10 Cellular Uptake

Flow cytometry was employed to analyze cellular uptake and material adsorption on cell membrane. Forward scatter (FSC) versus side scatter (SSC) signals were used in the analyses with the help of Flowjo Program. At the beginning, cells were seeded at 6 well plates at the density of 3×10^5 cells/well. Following the incubation, cells were treated with increasing concentration of hBN-Dox (5, 25, 125 $\mu\text{g}/\text{mL}$) and hBNs (4.76, 23.80, 119.04 $\mu\text{g}/\text{mL}$). To be equal to the amount of hBNs contained in the hBN-Dox, the concentrations of hBNs were calculated the amount of hBNs existing in the corresponding hBN-Dox concentration. With and without US treatment on the cells were compared on the same conditions to clarify the effect of US on cellular uptake. After 24 and 48h, the cells were trypsinized and suspended in PBS to analyze by flow cytometry. Negative control group of cells were not treated with materials and gated to evaluate SSC signal increase

representing endocytic or adsorptive NPs interaction. Data were collected with 10.000 events and gating was done according to FSC and SSC signals. Results were analyzed by FlowJo software (BD Life Sciences, USA) and given in the form of percentage according to control group.

2.2.11 Intracellular Doxorubicin Amount Detection

Intracellular amount of Dox was analyzed by flow cytometry. The cells were seeded at 3×10^5 cells per well in 6-well plates. Following the overnight incubation, the cells were treated with increasing concentration of hBN-Dox (5, 25, 125 $\mu\text{g}/\text{mL}$) and Dox (0.24, 1.20, 5.96 $\mu\text{g}/\text{mL}$) contained in hBN-Dox. US was applied to detect the effect of US on as seen in Table 1, within the incubation period of 24 and 48h.

Control group did not exposure to US. The signal of natural fluorescence of Dox was measured using excitation with a 488 nm blue laser and detection with a 530 nm \pm 30 nm filter (Karukstis et al., 1998). Data were collected with 10000 events and gating was done according to forward and side scatter signals. Results were analyzed by FlowJo software and given in the form of percentage according to control group.

2.2.12 Colony Formation Assay

Clonogenic assay was performed according to protocol of Franken (Franken, 2006). After exposure to US and material treatment, colony forming ability of a single cell tested by that method. At the beginning, cells were seeded at density of 3×10^5 cells per well into 6-well plates. And treated with increasing concentrations of hBN-Dox, hBNs and Dox. For the treatment procedure like other experiments method of US exposure and material treatment were followed. Concentration of hBNs and Dox were calculated according to concentration of hBN-Dox formulation. hBNs and Dox amount inside the hBN-Dox formulation was used for treatment of cells. Concentrations of hBN-Dox were 5, 25, 125 $\mu\text{g}/\text{mL}$, hBNs were 4.76, 23.80, 119.04 $\mu\text{g}/\text{mL}$ and Dox were 0.24, 1.20, 5.96 $\mu\text{g}/\text{mL}$. The treatments of hBN-Dox, hBNs and Dox were done with and without US stimulation within time periods of 24 and 48h. Following the treatment procedure, cells were harvested by using trypsin and re-plated at the density of 2×10^3 cells per well into 6-well plates. And then the cells were left for growing inside incubator until the control wells

have proper colonies which have at least 50 cells inside. With this strategy, potentially lethal damages that caused by the treatment procedure was assessed. When incubation period was completed, media was removed, and cells were washed with PBS. Cell fixation and dying was done with 6.0 % v/v glutaraldehyde and 0.5 % w/v crystal violet. Colonies were counted by ImageJ software (NIH, USA).

2.2.13 Apoptosis and Necrosis Assay

Apoptosis and necrosis are the two separate modes of cell death based on differences in the molecular changes, biochemical and morphological of the dying cell. Apoptosis and necrosis assays were performed to detect apoptotic and necrotic cells within the same cell population by using flow cytometry according to manufacturer's protocol. Initially, the cells were seeded into the 6-well plate with the density of 3×10^5 cells per well and left for 24h incubation. The protocols of materials treatment and US exposure explained in section 2.2.5 were followed. Control groups were not exposed with US to evaluate the effect of US stimulation. When the 24h material treatment and US exposure period was completed, cells were washed with PBS, trypsinized and collected. After that, the cells were centrifuged and washed with cell staining buffer two times, and then, resuspended in Annexin V binding buffer. 100 μ L of cell suspension were transferred inside a test tube, 5 μ L of FITC Annexin V and 10 μ L of Propidium Iodide (PI) solution was added to the cells. To obtain homogeneous mixture, the cells were gently vortexed and stained for 15 min in darkness at 25 °C. Following to that, 400 μ L of Annexin V binding buffer was added to each test tube to analyze samples in flow cytometer. PI dye was detected by a laser light excitation at 488 nm and PE/Texas Red channel was used. Annexin V was analyzed by using 640 nm laser for excitation with APC channel. Data for all of the samples was collected with 10.000 events. Results were analyzed by FlowJo software according to the control group.

2.2.14 Statistical Analysis

All of the obtained results were presented as mean \pm standard deviation (SD). Statistical significance of changes compared to negative control calculated by two-paired Student's t test and marked with asterisks. A p value of *p \leq 0.05, **p \leq 0.01, ***p \leq 0.001 was

shown as significant. * and ** were shown in Figures, *** were not shown.

3. RESULTS & DISCUSSION

3.1 Characterization of hBNs and hBN-Dox

hBNs were synthesized using the CVD method and characterized with imaging, thermal and spectroscopic techniques before the study of their interaction with Dox.

3.1.1 Characterization of hBNs

TEM images of hBNs with increasing magnifications were shown in Figure 10. As seen, hBNs have platelet-like morphology with lateral size dimension between 50 and 100 nm.

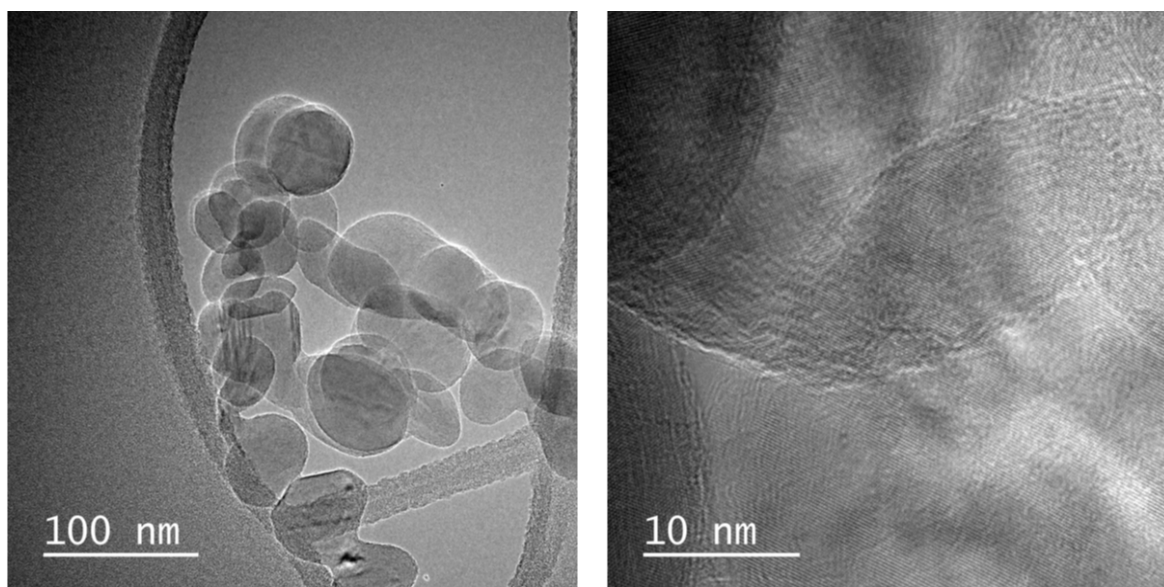


Figure 10. TEM images of hBNs with increasing magnifications

Figure 11 shows the characterization results using by FTIR, Raman, DLS, UV-vis spectra,

TGA plot and XRD spectrum. As vibrational spectroscopic techniques, FTIR and Raman spectroscopies provide valuable information about their chemical structures and they are routinely used to confirm their formation. The characteristic of structural features of sp^2 bonded B and N atoms of hBNs is shown on FTIR spectrum in Figure 11-a. The presence of bands at around 661 cm^{-1} , 775 cm^{-1} and 1363 cm^{-1} attributed to out-of-plane B-N-B bending, B-N bonding and in-plane B-N stretching vibrations, respectively, proving the successful syntheses of hBNs (Moon et al., 2004). The Raman spectrum of hBNs is shown in Figure 11-b. The band at 1367 cm^{-1} is attributed to the G band caused by a mode of out-of-plane vibrations (E_{2g}) of B and N atoms (Lu et al., 2013), which supports the FTIR data. Their hydrodynamic sizes and surface charges are characterized by using DLS technique. The size distribution of hBNs was found to be around 70 nm in diH_2O as shown in Figure 11-c. Polydispersity index (PDI) value was found as 0.256 ± 0.02883 that proves proper dispersion of hBNs. The PDI value ranging from 0 to 1 demonstrates the variation in size and aggregation status in the aqueous media. As the low PDI indicates better dispersion and a more homogeneous suspension. PDI index bigger than 0.7 demonstrates that the tested particle has very large hydrodynamic size which is not suitable for DLS measurement (Danaei et al., 2018). The surface charge of hBNs is found to be highly negative of $-27.9\pm 1.52\text{ mV}$. This value shows that the suspension of hBNs in diH_2O is stable. The UV-vis spectrum is shown in Figure 11-d with a band of 203 nm indicating an optical band gap of 5.86 eV, which is consistent with the literature (Li et al., 2021; Zhang et al., 2013). For further verifying phase identification of hBNs, XRD measurements were done. As shown in Figure 11-f, a total of five diffraction bands present. $2\theta = 26.7^\circ$ peak appears corresponding to (002) planes of BNs. The main peak is at Bragg angle (Zhu et al., 2008). The other peaks are $2\theta=41.6^\circ$ corresponding to (100), $2\theta = 43.9^\circ$ corresponding to (101), $2\theta=55.8^\circ$ corresponding to (004) planes of hBNs structure. The XRD data supports the FTIR and Raman spectroscopy findings. The TGA plot demonstrating the weight/mass change (loss or gain) in response to heating of a hBNs sample at a constant rate is shown on Figure 11-e. As seen, the characteristic thermal stability feature of hBNs was observed through 800°C . The observed 1.54 % weight loss can be explained with humidity loss (Ysiwata-Rivera et al., 2020).

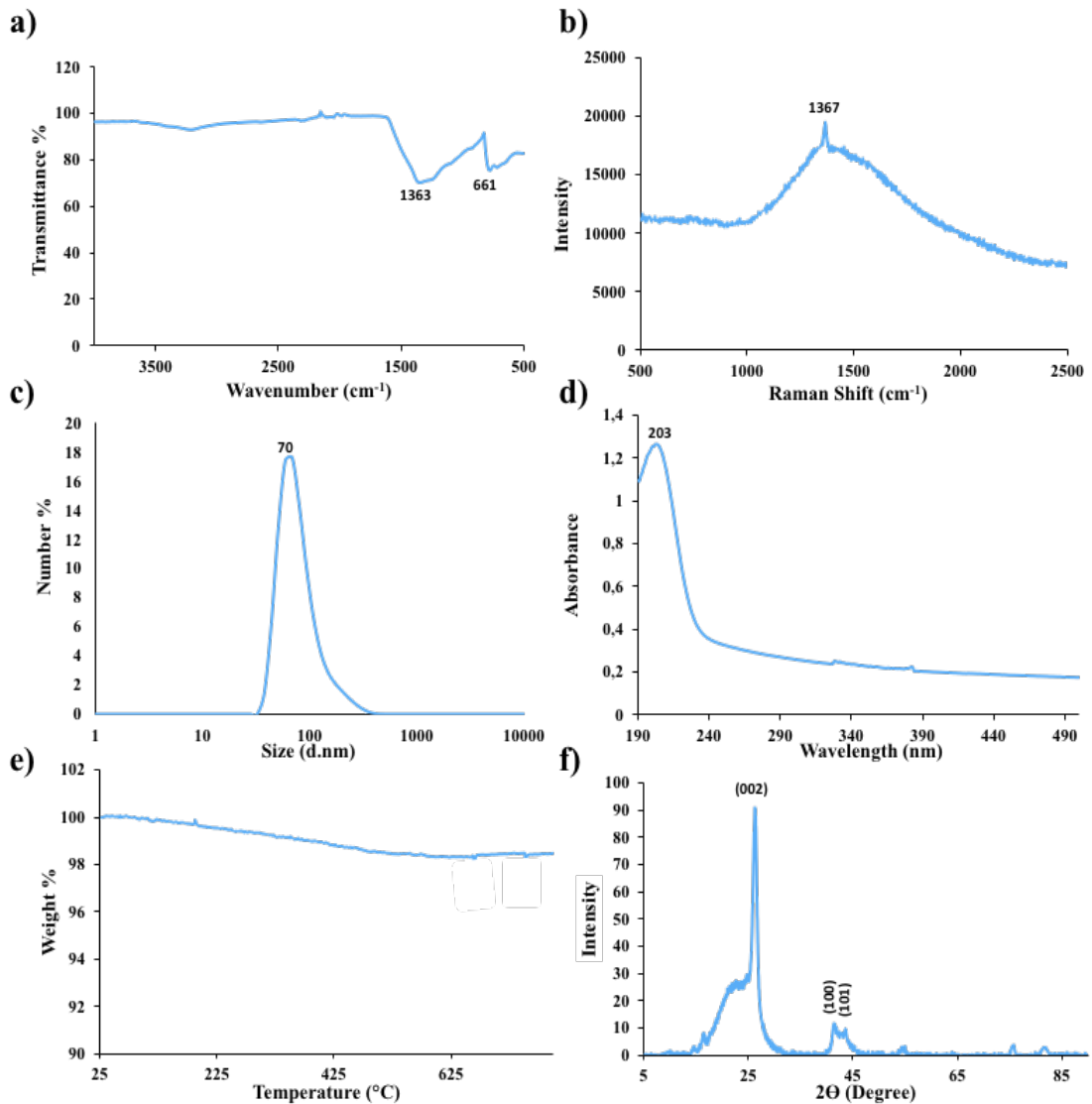


Figure 11. a) FTIR, b) Raman, c) DLS, and d) UV-Vis, f) XRD, and e) TGA spectra of hBNs

3.1.1.1 Piezoelectric Properties of hBNs

PRFM is a standard characterization technique for analyzing piezoelectric properties of material in size of nano and micrometer (Uršič & Prah, 2019). This technique comes with many advantages including high resolution, ability to make local measurements in complex structures and working without any damage to sample material. In this mode of operation, cantilever is in contact with surface of the sample at a constant force. While amplitude graph gives results related to the strength of piezoelectric signal of the material, phase shows direction of polarization. The contrast in amplitude and phase images

provide information about the degree of polarization. Regions with high contrast represent high polarization and regions where contrast is low represents low polarization. The topography, amplitude and phase images were recorded as shown in Figure 12-a, b and c, respectively. As seen in Figure 12-a, the size of hBNs is not uniform indicating possible aggregation as they dry from their suspension on the substrate surface. Although, a uniform distribution of hBNs grains is desired it may not be possible due to drying dynamics of a suspension droplet. Indeed, Figure 12-b demonstrating the PRFM amplitude image obtained 2 mV values depending on the position shows the presence of aggregates of hBNs grains. The two lines (green and blue) on the amplitude image were drawn between opposite contrasts to obtain the graphs (right side of image) shown the maximal degree of polarization through that position. The maximum PRFM amplitude response of hBNs was obtained as 2 mV. In Figure 12-c PRFM phase contrast image was shown and again two lines were drawn along the scanned area to obtain maximal degree of angle of polarization. Piezoelectric response of materials directly depends on the angles within crystal structure of the material. These angles are originated from the atoms of the material and in response to applied external mechanical stimulation which creates a direction of elongation. According to related graph, the maximum phase contrast was found as higher than 300° and high contrast proves spontaneous electrical polarization feature of hBNs.

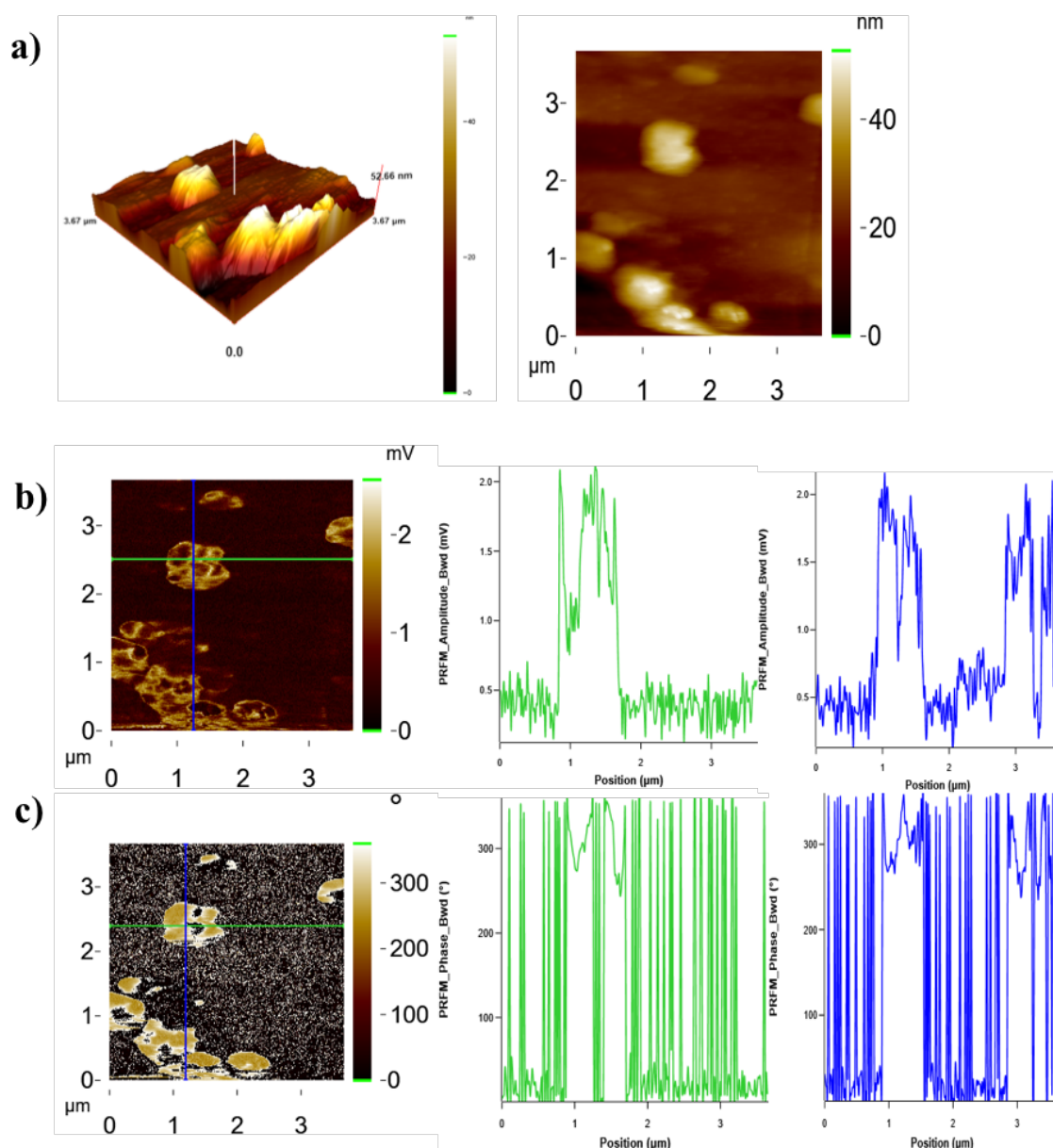


Figure 12. PRFM measurement results for hBNs a) Topography, b) piezoelectric amplitude, and c) PRFM phase images of hBNs All images were taken at the same 3.5x3.5 μm^2 scan area at room temperature

3.1.2 Characterization of hBN-Dox

Functionalization and loading applications of NMs are critical steps to bring new characteristics to a desired material. π - π stacking is a type of non-covalent/electrostatic interaction occurring between aromatic moieties that has benefits for biological applications such as strong binding ability, non-disruptive fabrication procedure and simple operation steps (Chen et al., 2018). With this way, different types of materials

proteins, polymers, and inorganic groups can be loaded successfully on the surface of structurally suitable NMs. The non-covalent interactions were used as a strategy of Dox loading onto hBNs to create hBN-Dox.

After the loading onto hBNs, their characterization was performed using FTIR, UV-vis spectroscopy and DLS techniques to determine the Dox loading success. To confirm the successful binding, the washing steps were repeated several times to eliminate free Dox molecules that not bonded strong enough to hBNs. After the washing steps, supernatants and precipitations were used for further analysis. While the dried precipitate was used for FTIR measurements, it was redispersed in diH₂O for DLS measurements. The supernatants were analyzed by UV-vis spectroscopy at 480 nm to determine the unbonded free Dox. The Figure 13-a shows the comparison of FTIR spectra of hBNs, hBN-Dox and Dox. As seen, the FTIR spectrum of Dox has the multiple bands observed at 3338 (N-H stretching), 3522 (O-H stretching), 2926 and 2893 (C-H stretching), 1730 (C=O stretching), 1612, 1579 and 1411 (C=C ring stretching), 1112 and 1070 (C-O-C stretching), 802 and 686 (C-H bond), 1278, 1203 (O-H), 2926 and 2893 cm⁻¹ (C-H stretching), and 1149 cm⁻¹ (C-O-C stretch or C=C ring) (Bansal et al., 2021).

As explained in section 2.3.1, the characteristic bands of hBNs, out-of-plane B-N-B bending and in-plane B-N stretching vibrations appear at around 669 and 1327 cm⁻¹, respectively (Moon et al., 2004). When hBNs and hBN-Dox spectra are compared, hBN-Dox differs from hBNs with C-H bands at 2908, 2947 cm⁻¹, O-H bands at 1280, 1207 cm⁻¹ and C-O-C band at 1107 cm⁻¹ indicating the binding of Dox onto hBNs.

Comparison of UV-vis spectra of Dox, hBNs and hBN-Dox are shown in Figure 13-b. As seen, the one of the maximum absorption peaks of Dox is around 234, 255, 297 and 480 nm (Yao et al., 2013) while the that of hBNs is at around 203 nm (Liang et al., 2018). The UV-vis spectrum of hBN-Dox has both characteristics bands of hBNs and Dox around 203, 234, 255 and 480 nm indicating a successful loading.

The hydrodynamic size of hBN-Dox was measured by DLS and is shown in Figure 13-c and it was found to be around 197 nm while the size hBNs was around 70 nm. The surface charge of hBNs and hBN-Dox was measured as -27.9±1.52, -7.39±2.1 mV, respectively and shown in Figure 13-d.

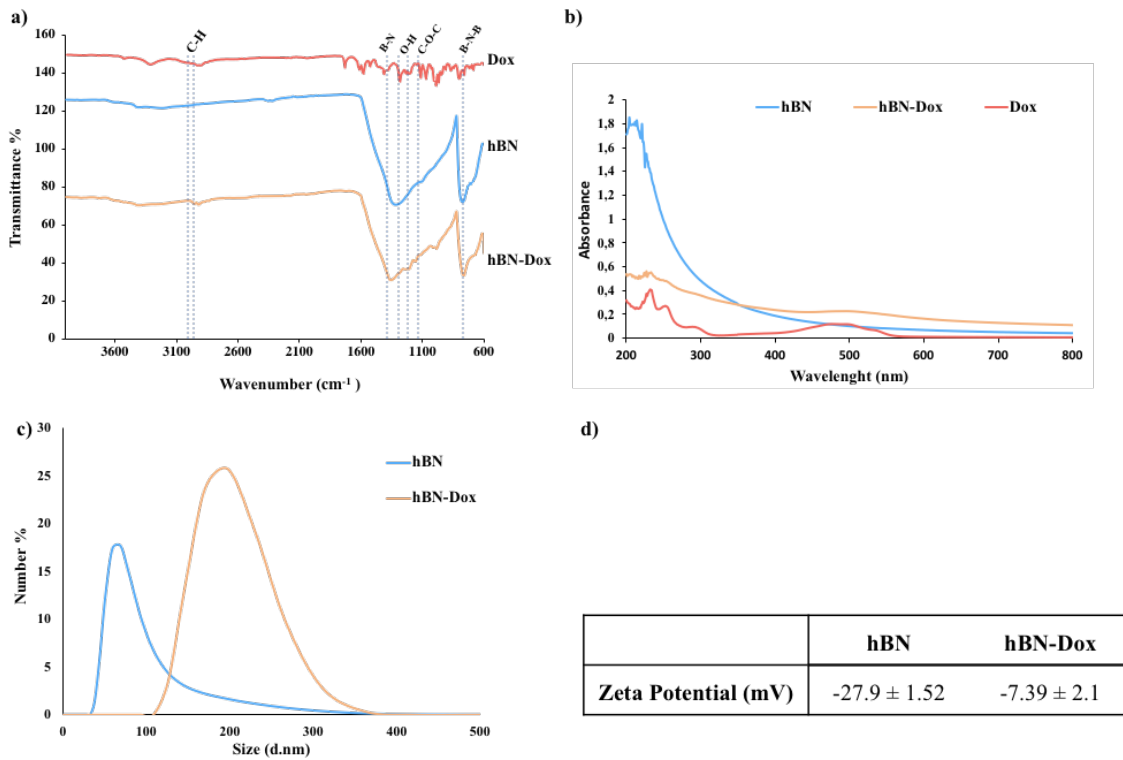


Figure 13. Comparative characterization data of hBNs and hBN-Dox in diH₂O with a) FTIR b) UV-vis spectroscopy c) DLS and d) Zeta potential values (margins of error are given as ± standard deviation, n = 3)

3.1.2.1 Piezoelectric Properties of hBN-Dox

AFM was used to analyze topography of hBN-Dox and the results are shown in Figure 14. As seen, the topography images indicate that the hBN-Dox is in the form of aggregates similar to hBNs case as a result of droplet drying dynamics on the substrate surface. Thus, the expected sizes are much larger (224.05 nm) than the single grain size. Their piezoelectricity was characterized with PRFM mode as discussed before. The amplitude and phase images with their graphs for quantitative analysis are shown in Figure 14-a and b, respectively. Two lines on the images are drawn to measure the strength of piezoelectric signal according to contrast differences in detected positions and an amplitude graph was obtained. According to the graph, the maximum PRFM amplitude value was measured as 50 mV. Compared to hBNs, hBN-Dox has higher piezoelectric response, which may be explained Dox loading causing hBNs structure to decrease in the centrosymmetry. It is also possible that the defects on hBNs structure can increase during the loading process

as result of sonication. In Figure 14-c, the PRFM phase image with two lines drawn through the scanned area to detect maximum angle of direction of polarization is shown. According to the graph, PRFM phase is more than 300° in both lines indicating high spontaneous electrical polarization of hBN-Dox.

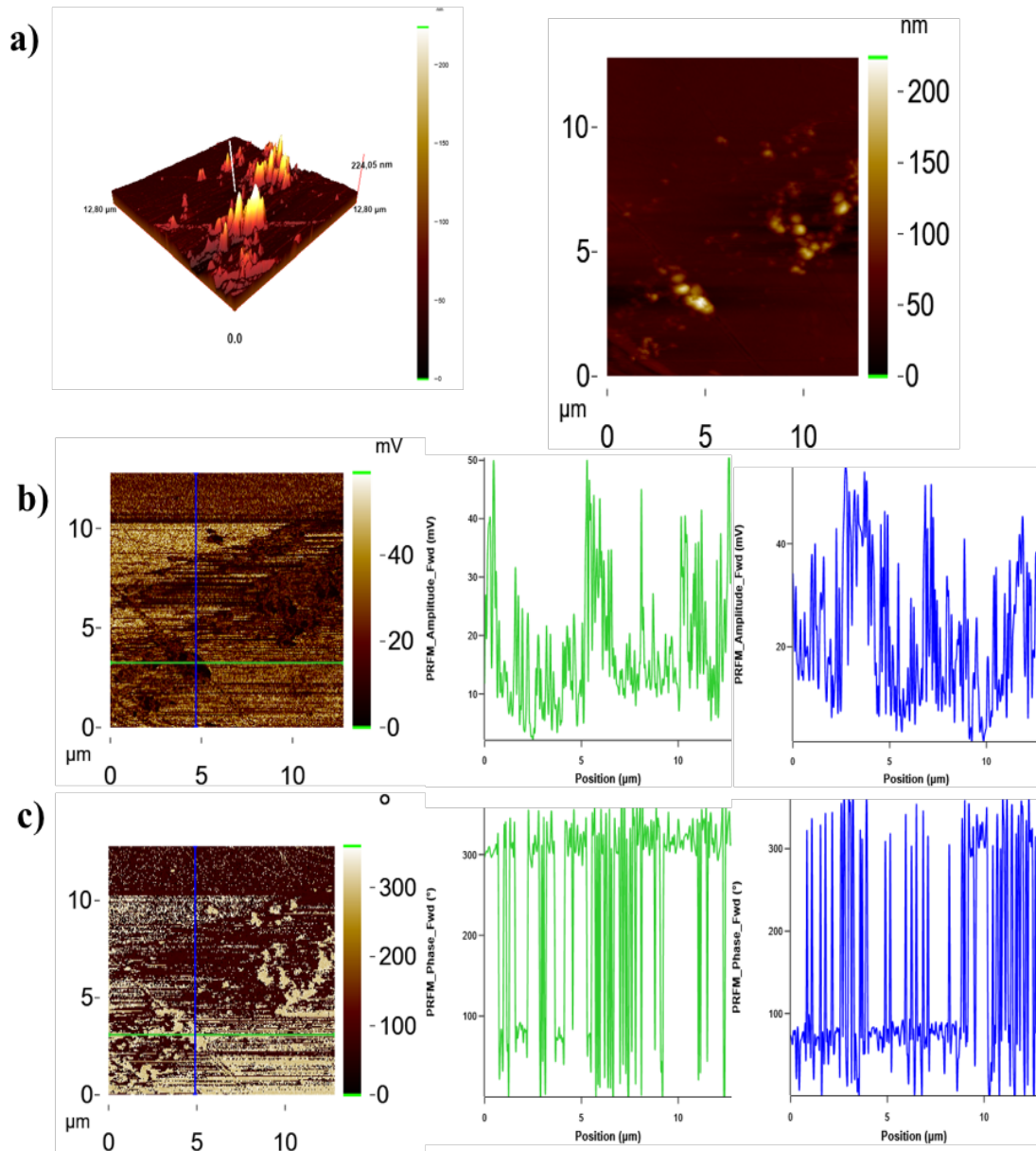


Figure 14. PRFM measurement results of hBN-Dox a) Topography, b) piezoelectric amplitude, and c) PRFM phase images of hBNs. All images were taken at the same $12.3 \times 12.3 \mu\text{m}^2$ scan area at room temperature.

3.1.2.2 Dox Loading Efficiency and Loading Capacity of hBNs

After confirming the Dox loading onto hBNs and their piezoelectricity, the drug loading efficiency and loading capacity were calculated. The drug loading efficiency is defined as the ratio of the amount of drug bound to NMs to the total amount of drug attempted to load and is expressed as the Equation 1. Drug loading capacity represents percentage of particles that carries the drug and was calculated by Equation 2.

$$\text{Drug Loading Efficiency \%} = \frac{(\text{Weight of initial drug} - \text{Weight of final drug})}{\text{Weight of initial drug}} \times 100$$

Equation 1. Formula of drug loading efficiency

$$\text{Drug Loading Capacity \%} = \frac{(\text{Weight of initial drug} - \text{Weight of final drug})}{\text{Weight of carrier}} \times 100$$

Equation 2. Formula of drug loading capacity

UV-vis spectroscopy was used to obtain the calibration curve of Dox by plotting the mean absorbance value versus the concentration of Dox. The calibration curve of Dox is shown in Figure 15. Based on the $y=0.0138x+0.3194$ equation, the concentration of the free Dox is calculated from the supernatants, where y is the absorbance value, and x is the concentration of Dox.

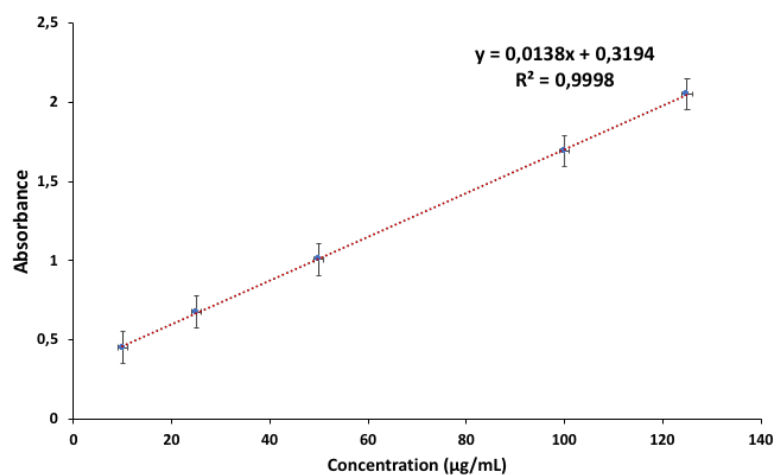


Figure 15. Calibration curve of Dox

Dox was demonstrated the excellent loading efficiency in every tested time intervals as shown in Table 2. The highest loading efficiency of Dox (99.8 %) was obtained at 6h loading time. Because of that, it was chosen for further experiments owing to the time

and energy efficiency. Table 3 summarizes the amounts of hBNs and Dox in a certain dose of hBN-Dox, calculated according to the calibration curve and Dox loading efficiency values.

Table 2. Dox loading efficiency and capacity as percentage with increasing loading time intervals

	6h	24h	48h
Dox Loading Efficiency % \pmSD	99.8 % \pm 1.13	95.3 % \pm 3.53	90.65 % \pm 9.4
Dox Loading Capacity % \pmSD	4.9 % \pm 0.05	4.7 % \pm 0.17	4.5 % \pm 0.42

Table 3. Calculated concentrations of hBNs and Dox inside obtained hBN-Dox

hBN-Dox (μg/mL)	hBNs (μg/mL)	Dox (μg/mL)
625	595.24	29.76
125	119.05	5.95
25	23.81	1.19
5	4.76	0.24

The high affinity of Dox to hBNs can be attributed to aromatic ring in the structure of Dox facilitating interaction with hBNs. Also, electrostatic interaction plays an important role in hBN-Dox interaction. Dox is positively charged drug at neutral pH, which is the condition loading performed. Therefore, with its ionizable amino group, it can easily interact with negatively charged hBNs under the same experimental conditions. In order to prove electrostatic interactions between hBNs and Dox, the zeta potential measurements were performed in the same pH of hBNs and hBN-Dox. As seen in Figure 13d, whereas the zeta potential value of hBNs is -27.9 ± 1.52 mV, hBN-Dox is -7.39 ± 2.1 mV. These results further proved the existence of electrostatic interactions between hBNs and Dox.

3.2 Degradation Profile of hBNs

Boron-based compounds gained special attention due to findings related to boron supplementation that has inhibitory effect on prostate cancer cell proliferation and tumor growth (Barranco & Eckhert, 2004; Gallardo-Williams et al., 2004). However, the constant administration of boron-based compounds brings many challenges due to their short half-life, inadequate bioavailability and need for a continuous administration as well as insufficient reach of B to the tumor site resulting with low efficiency in the prostate cancer treatment (Li et al., 2017). It is thought that the boron-based NMs with low-solubility can overcome this challenge by creating targeted, increased permeability and retention effects (Li et al., 2017).

hBNs as boron-based NMs were proposed as a therapeutic agent because of its boron content and slow degradation profile (Şen et al., 2018). The degradation profiles of hBNs and hBN-Dox by the application of US were analyzed by ICP-OES. As seen in Table 4, the released boron from hBNs and hBN-Dox within 6, 24, 48h for increasing pHs was determined comparatively. It was found that although the boron release from hBNs was stable at both increasing times, and pHs, the boron release of hBNs exposed to US was found to increase significantly at all pHs and times. On the contrary, a sharp decrease of boron release from hBN-Dox was determined which can be explained that the non-specific interaction of hBNs and Dox increased as stability of hBNs in aqueous environments. This is possibly due to the fact that hBNs loaded with Dox gained more stability against the US exposure.

Table 4. Results of ICP-OES analysis of hBNs and hBN-Dox demonstrating ppm of released boron

		6h (ppm±SD)	24h (ppm±SD)	48h (ppm±SD)
hBNs	pH 3	4.15±0.01	4.16±0.01	4.18±0.01
	pH 5	4.09±0.02	4.13±0.01	4.19±0.02
	pH 7.4	4.09±0.02	4.27±0.01	4.19±0.01
	pH 9	4.13±0.01	4.12±0.02	4.20±0.01
hBN+US	pH 3	17.94±0.11	14.71±0.05	14.89±0.05
	pH 5	17.00±0.03	18.39±0.01	14.84±0.06
	pH 7.4	15.30±0.19	17.08±0.15	18.79±0.02
	pH 9	15.09±0.08	15.16±0.03	17.76±0.05
hBN-Dox	pH 3	0.52±0.01	0.56±0.01	0.66±0.01
	pH 5	1.13±0.01	1.22±0.07	1.19±0.01
	pH 7.4	0.84±0.03	0.93±0.07	3.67±0.13
	pH 9	0.42±0.05	0.57±0.06	3.75±0.21
hBN-Dox+US	pH 3	0.53±0.01	0.61±0.43	0.85±0.04
	pH 5	1.17±0.01	0.99±0.07	1.36±0.01
	pH 7.4	0.89±0.05	0.94±0.01	3.69±0.37
	pH 9	0.67±0.01	0.46±0.43	4.01±0.03

3.3 Identification of Dox Release Profile

pH and US dependent Dox release of hBN-Dox was investigated at increasing pHs of 3, 5, 7.4, 9 and times of within 6, 24 and 48h with and without US exposure. pH 7.4 is used to mimic physiological pH (Li et al., 2012) while pH 5.0 was used to mimic tumor microenvironment (Vaupel et al., 1989) and pH 3.0 to mimic gastric pH (Sammon et al., 2015). pH 9.0 was tested to clarify effect of pH fully by mimicking higher pHs that are found in human body such as small intestine. The pH-dependent release profile of Dox from hBN-Dox is represented in Figure 16. While the highest Dox release reaches up to 60 % at pH 3, the release decreases to 35 % at pH 9. Due to the presence of an ionizable amino group on its structure, the interaction of Dox with hBNs is strongly affected from pH changes. Because Dox has protonable amino group, it demonstrates hydrophilic feature and its release is favoured at lower pHs (Swiech et al., 2020). Decreased level of

Dox release in higher pH values including blood pH, could bring a critical advantage in reduction of toxic side effects of chemotherapeutic Dox. Moreover, the low level of release can enhance half-life in blood circulation by increase the change of reaching higher amount of Dox to the tumor site. In addition to that, effect of US treatment within different time intervals also investigated. It can be seen from Figure 16 that in every tested time with US exposure, Dox release was increased. It is known that local delivery and triggered release of an anticancer drug increase effect of therapy and decrease side effects (Goldberg et al., 2002). In that regard, the obtained results were proved that the hBNs have high potential as a drug carrier system to deliver targeted and triggered release of Dox. In next section, *in vitro* behavior of hBN-Dox were investigated of hBN-Dox in a potential therapeutic application.

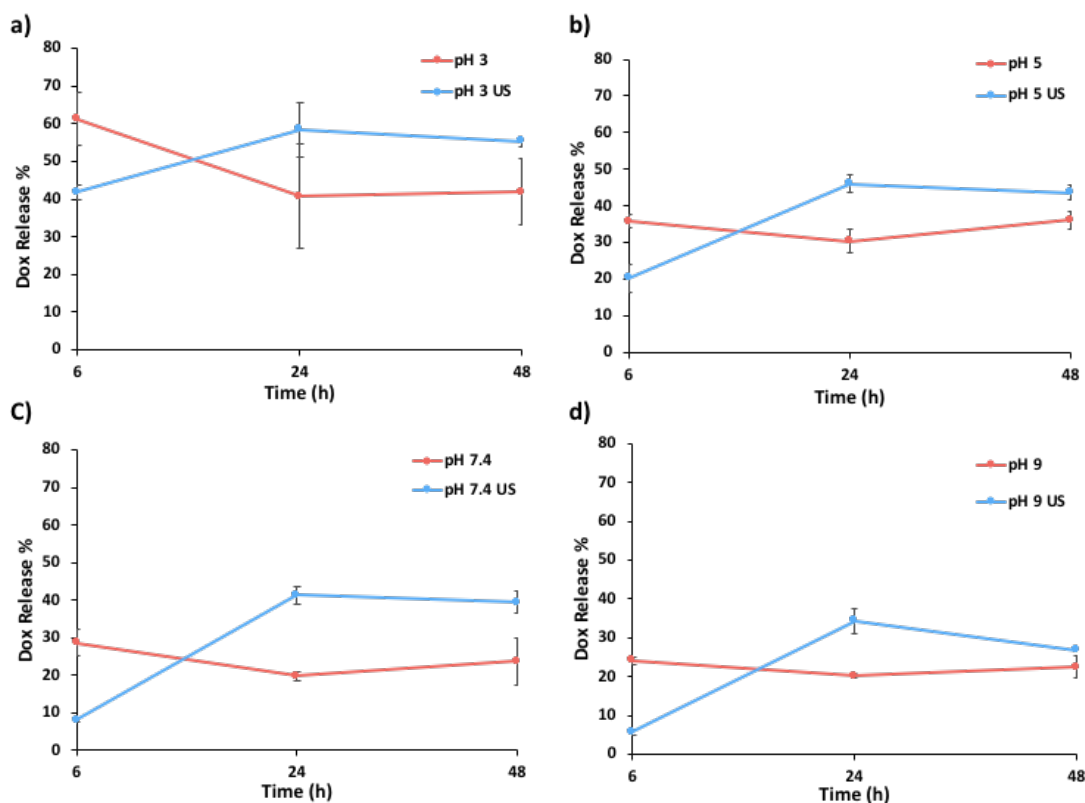


Figure 16. Percentage of released Dox from hBN-Dox in PBS at a) pH 3 b) pH 5, c) pH 7.4, d) 9 with and without US exposure within the incubation time of 6, 24 and 48h

3.4 Cell Viability Analysis

WST-8 assay was employed to investigate the effects of hBNs, hBN-Dox, Dox and BA,

and US on the number of live PC3 and PNT1A cells. WST-8, a water-soluble tetrazolium, is converted to an orange formazan dye as result of reduction in response to mitochondrial activity. WST-8 tetrazolium salt is reduced by cellular dehydrogenases (NADPH), the produced orange formazan dye is accepted as an indicator of cellular viability (Chamchoy et al., 2019). Figure 17 represents the viability of PC3 cells treated with hBN, hBN-Dox and Dox for 24 and 48h. It was found that the effect of NMs on the cell viability was dose dependent. While the dose increased, the cell viability was decreased. US exposure for 24h incubation was caused 19 % decrease the cell viability compared to untreated control. In connection with this effect, the cells toxicity caused by materials caused a decrease of cell viability up to 10 % by applying US. Within 48h, US exposure was caused 22 % increase of the cell viability. While hBNs treatment in the highest dose (625 $\mu\text{g/mL}$) caused a decrease in cell viability incubation period up to 61 % for 48h, hBN-Dox was caused up to 4.7 % reduction and Dox caused 3 %. If we compare effect of hBN-Dox and Dox within 24h in the highest treatment dose (625 $\mu\text{g/mL}$), while hBN-Dox caused a reduction in cell viability up to 7.9 %, Dox was caused 5.9 % reduction. When the amount of Dox that is found inside hBN-Dox is considered, within 625 $\mu\text{g/mL}$ hBN-Dox only 29.7 $\mu\text{g/mL}$ Dox exists. It can be concluded from the results that by using around 21 times less Dox, hBN-Dox created almost same cell viability reduction effect on PC3 cells with the help of US exposure. This effect can be seen as promising for dose reduction with any significant decrease on effectiveness of chemotherapeutic Dox.

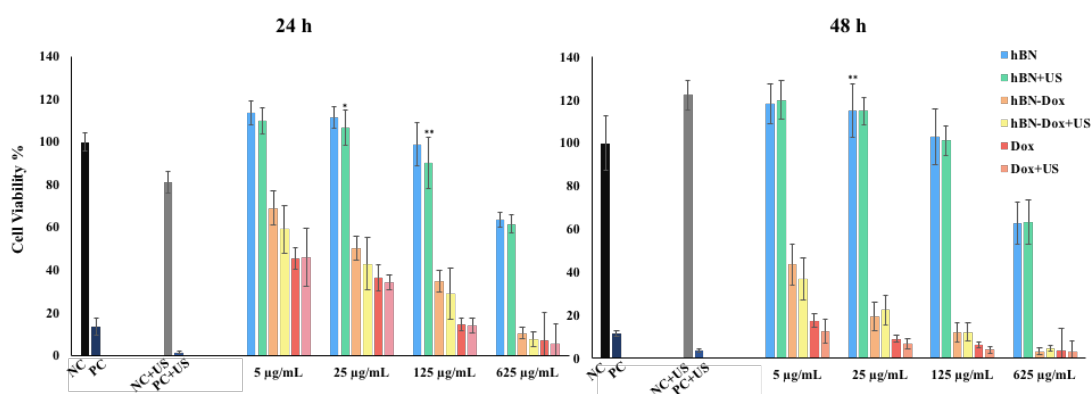


Figure 17. PC3 cells viability after 24 and 48h incubation with increasing concentration of hBNs, hBN-Dox and Dox, and US exposure

It was found that the cell toxicity caused by NMs directly depends on cell type,

physicochemical properties of NMs, exposure concentration and time (Sohaebuddin et al., 2010). Thus, the same conditions of NMs treatment and US exposure were applied to PNT1A cells, which are used as healthy control. Figure 18 represents the results of cellular viability of PNT1A cells within 24 and 48h incubation treated with hBNs, hBN-Dox and Dox with and without US exposure. Compared to the untreated control group while US exposure within 48h, it caused 24 % decrease in cell viability within 24h incubation period and caused 14 % increase in cell proliferation. Literature supporting that finding, it was found that low intensity pulsed ultrasound has ability to enhance cell proliferation of different kinds of cell lines including skin fibroblasts (Zhou et al., 2004), chondrocytes (Zhang et al., 2003) and osteoblasts (Sena et al., 2005). Material treatments on this cell caused dose dependent effect in both 24 and 48h incubation period. In the highest dose (625 µg/mL) hBNs caused cell viability reduction up to 27 % with US stimulation. In treatments with doses of 5, 25 and 125 µg/mL, hBNs increased proliferation of cells by US stimulation within 24h. And the same doses did not cause any damage on the cells within 48h. While Dox treatment of 5, 25 and 125 µg/mL doses higher decrease in viability with up to 4 %, hBN-Dox treatment within the same concentrations can be considered as safer with up to 12 % cell viability reduction in every tested time interval.

Compared to PC3 cells with PNT1A cells, within 24h US exposure caused viability decrease in cancer cell line while increase cell proliferation of healthy control. Similar findings can be found in literature. For instance, it was found that low intensity US exposure damages cytoskeleton of cancer cells while healthy cells are not affected (Mittelstein et al., 2020). Also, it is found that chronic electrical stimulation has ability to inhibit cancer cell proliferation by affecting Ca^{2+} homeostasis and arrangement of mitotic spindles during mitosis (Marino et al., 2018). In that regard, apart from molecular markers cancer cells can be targeted for therapeutic applications with their mechanical properties. Moreover, US stimulation stimulate cytokine and chemokine release from cancer cells proving therapeutic efficiency of that strategy from many perspectives (Lee et al., 2020). While 5 µg/mL hBN-Dox causes, 41 % decrease in PC3 cell line, it caused 20 % viability decrease in PNT1A. In 25 µg/mL, hBN-Dox causes, 57 % decrease in cell viability of PC3 cell line, in healthy control it is found as 37 %. While 125 µg/mL hBN-Dox treatment of PC3 cells reduced viability to 28 %, in PNT1A cells it was found as 46 %. It can be

concluded from these findings that, hBN-Dox treatment can reduce viability of cancer cell and still be safe for healthy cell lines. This effect is originating from not only US exposure, but also electrical signals created by piezoelectric hBN-Dox in response to US exposure. Parallel to these findings Sersa et al. found that electrical signals on tumor cells increase effect of chemotherapeutic drugs by causing formation of holes that facilitates drug uptake inside the cells (Sersa et al., 1996).

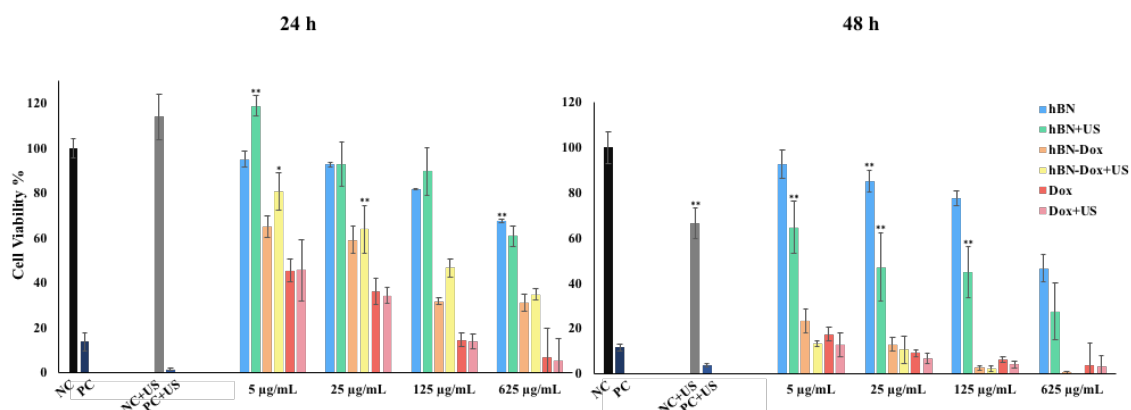


Figure 18. PNT1A cells viability after 24 and 48h incubation with increasing concentration of hBNs, hBN-Dox and Dox, and US exposure

BA is considered as potential degradation product of hBNs. And it is the most frequently seen form of B in plasma (Li et al., 2017). Therefore, the biocompatibility and of BA was investigated on PC3 and PNT1A cells within 24 and 48h incubation period and increasing concentrations. Viability results of PC3 cells were shown in Figure 19. As seen, BA in the highest dose (625 µg/mL) caused decrease in cell viability up to 66 %. In the lowest dose (5 µg/mL), it causes an increase in cell proliferation. In every tested time period US stimulation decreased the viability of BA treated cells. And viability decrease was observed as dose dependent. Similar to those findings, BA was found as inhibitor of cell proliferation of prostate cancer cells (Barranco & Eckhert, 2004).

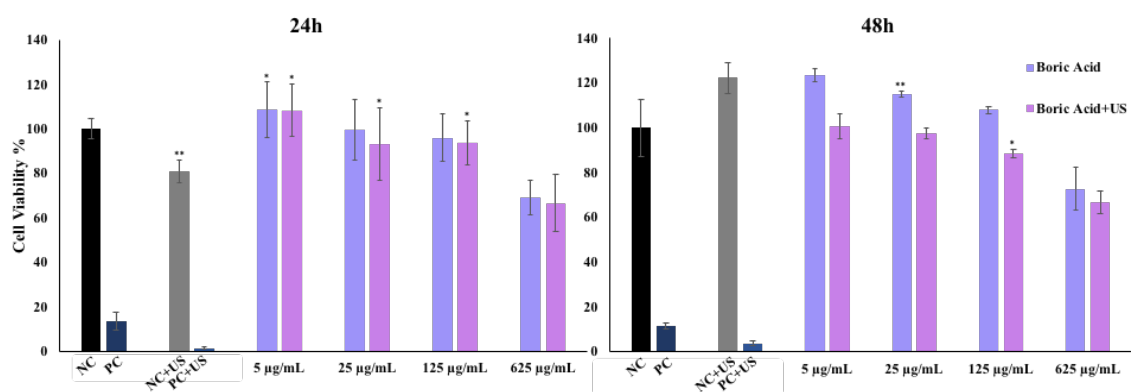


Figure 19. PC3 cells viability results within 24 and 48h incubation with increasing concentrations of BA and US exposure

Results of the assay testing viability after treatment of PNT1A cells with increasing concentrations of BA were shown in Figure 20. It can be seen from the graphs that, while BA was not toxic for 24h incubation, it caused dose and time dependent toxicity for 48h. The lowest dose (5 µg/mL) for both time points increased the cell proliferation and can be considered as safe. In 24 and 48h, US exposure to BA treated cells demonstrated a decrease in the cell viability. The highest dose (625 µg/mL) treatment resulted with viability decrease up to 22 %.

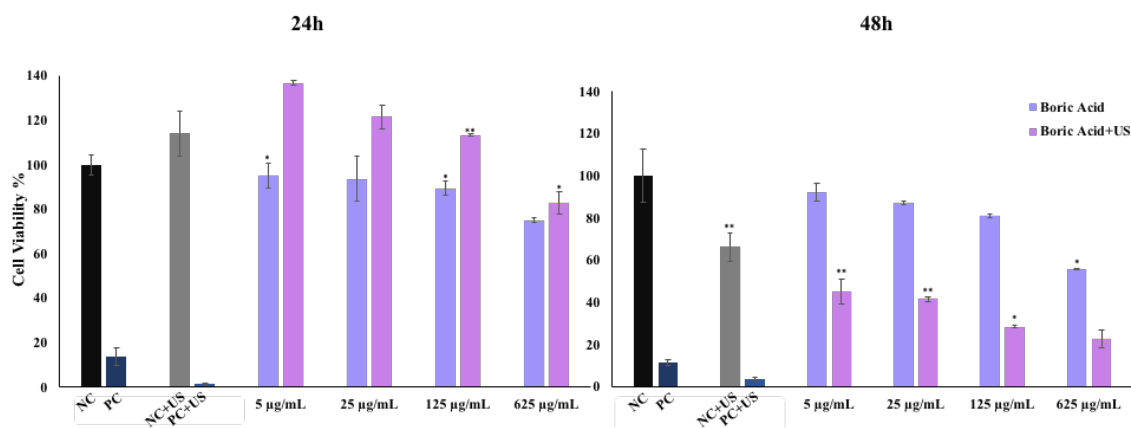


Figure 20. PNT1A cells viability results within 24 and 48h incubation with increasing concentrations of BA with and without US exposure

The half maximal inhibitory concentration (IC50) value is defined as a concentration reduces a certain biological or biochemical function by 50 % (Liu et al., 2014). This value has great importance in pharmacological studies as an informative measurement of potency of a tested pharmacological agent (Aykul & Martinez-Hackert, 2016). In that

context, IC50 value is concentration that reduces half of the cellular viability. Table 5 summarized calculated IC50 values of hBNs, hBN-Dox, Dox and BA within 24 and 48h with and without US exposure to PC3 and PNT1A cells. According to table in PC3 cells, IC50 value of hBN-Dox was calculated as 19.7 $\mu\text{g/mL}$ and it decreased to 12.51 with US exposure in 24h. In PNT1A cells, IC50 value of hBN-Dox was 8.94 $\mu\text{g/mL}$ and it increased to 18.26 $\mu\text{g/mL}$ with US in 24h proved IC50 value of PC3 cells with US exposure in 24h has less detrimental effect for PNT1A healthy cell line. This finding was very promising for a treatment strategy including a chemotherapeutic drug. In addition to that, While IC50 value of hBN-Dox is 12.51, Dox alone is 6.54 with US in 24h. According to drug loading efficiency and calibration curve in 12.51 $\mu\text{g/mL}$ hBN-Dox, 0.59 $\mu\text{g/mL}$ Dox exists. Comparing to 6.54 $\mu\text{g/mL}$ Dox as inhibitor of half of the cancer cells, only 0.59 $\mu\text{g/mL}$ Dox was enough to kill half of the cancer cells. With Dox loading to hBNs, compared to Dox alone, effectiveness of that drug increased around 11 times and demonstrated high potential of formulated hBN-Dox.

Table 5. Calculated IC50 values of hBNs, hBN-Dox, Dox, BA for PC3 and PNT1A cells according to cellular viability results

	IC50 Values ($\mu\text{g/mL}$) – 24h				IC50 Values ($\mu\text{g/mL}$) – 48h			
	PC3		PNT1A		PC3		PNT1A	
		US		US		US		US
hBNs	159.4 \pm 4.49	144.5 \pm 3.27	80.64 \pm 5.11	54.45 \pm 5.04	163.9 \pm 3.51	159.4 \pm 4.38	99.14 \pm 9.48	8.79 \pm 5.02
hBN-Dox	19.7 \pm 5.71	12.51 \pm 6.36	8.94 \pm 7.90	18.26 \pm 4.84	4.682 \pm 6.69	3.815 \pm 7.07	3.54 \pm 9.11	3.41 \pm 4.60
Dox	6.456 \pm 4.08	6.544 \pm 5.98	8.48 \pm 2.94	21.91 \pm 8.76	3.527 \pm 1.58	3.492 \pm 3.23	3.58 \pm 7.84	3.47 \pm 5.51
BA	167.8 \pm 2.97	101.4 \pm 7.19	97.43 \pm 8.43	50.76 \pm 6.19	169.3 \pm 4.67	155.5 \pm 7.39	87.25 \pm 8.22	3.56 \pm 4.58

3.5 ROS Analysis

ROS, superoxide anion (O_2^-), singlet oxygen ($^1\text{O}_2$), hydroxyl radicals (OH), peroxides (ROOR'), hydroperoxides (ROOH) and hydrogen peroxide (H_2O_2), are constantly generated as a result of aerobic metabolism of cells (Eruslanov & Kusmartsev, 2010). DCFDA is the most popular technique aiming to detect intracellular ROS. DCFDA itself

is a nonfluorescent and cleaved by intracellular esterases to produce H₂DCF and due to oxidation H₂DCF turns into a fluorescent DCF (Ng & Ooi, 2021). Thus, increase in the fluorescent signal directly enable us to analyze intracellular ROS. With this technique, ROS generated in response to hBNs, hBN-Dox, Dox and BA treatment with increasing concentrations, and with and without US exposure within 24h time interval was detected on PC3 and PNT1A cell lines. Figure 21 represents ROS % calculated according to untreated control group. As seen, while US exposure of cells causes 11 % increase in ROS generation in PC3 cells, this percentage is 3 % in PNT1A cells supporting the data come from cell viability assay. Decrease in cell viability caused by only US exposure lowers PC3 cells viability % of cells while it did not cause any damage on PNT1A cells. In every tested concentration and material US exposure resulted with an increase in ROS generation in PC3 cells. In PNT1A cells, except for the highest dose (625 µg/mL), ROS generation decreased in response to US exposure after treatment with hBNs and hBN-Dox. Also, in every tested concentration ROS % was lower after treatment with hBN-Dox in PNT1A cell line proving its potential for a therapeutic application. These findings contain similar results with previous experiments performed by our group. In that previous study, hBNs were able to lower ROS generated by Dox treatment on cells (Taskin et al., 2020). In this study, this effect was further shown with piezoelectric hBN activated by US exposure as well as hBN-Dox.

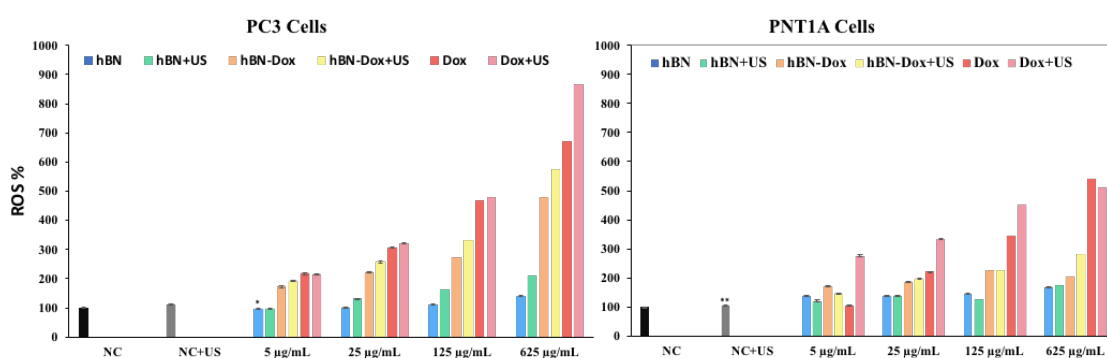


Figure 21. Detected ROS % inside PC3 and PNT1A cells

Effect of BA treatment with increasing concentration on cells with and without US treatment within 24h time interval was calculated according to untreated control group and shown in Figure 22. According to the graphs, BA caused an increase in ROS production in every tested concentration and cell line with increasing concentration. After

US exposure ROS % increased in every tested concentration and cell line. Supporting these results and cell viability results, BA found as cancer cell proliferation inhibitor by hampering receptor activated Ca^{2+} release (Handerson et al., 2009).

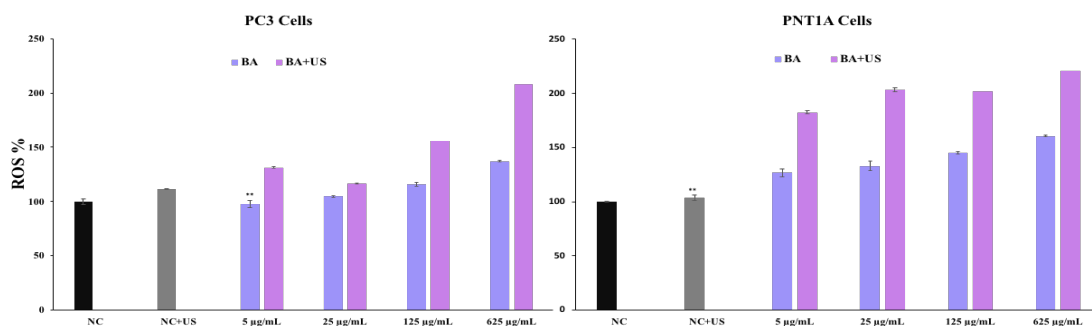


Figure 22. Detected ROS % inside PC3 and PNT1A cells in response to BA treatment

Different ROS % in response to hBNs, hBN-Dox, Dox and BA can be explained by both features of selected cell lines and properties of tested materials. While hBNs and hBN-Dox are able to be activated by US and produce electricity due to their piezoelectric feature, Dox and BA do not have this effect.

It is known that electrical stimulation has ability to affect several different cellular processes including affect cell migration, cell proliferation, and cell differentiation (Chen et al., 2019). Also, alternating current can lower cancer cell proliferation by affecting calcium and potassium channels (Janigro et al., 2006). Analysis of cellular uptake of tested material was critical to clarify reasons of this effect. Therefore, in next section cellular uptake was analyzed.

3.6 Cellular Uptake Analysis

Location of the NMs inside the cell is critical to see desired effect arising from the materials. Therefore, the cellular uptake analysis by flow cytometry was performed to understand relative uptake of NMs by the cells. Flow cytometer allows single cell analysis by the help of two optical detectors that measures two main parameters including FSC and SSC signals. FSC signal performs the measurement through the path of laser and gives information related to size of cells while SSC signal comes with 90-degree

angle and is related to internal complexity and granularity of cells (McKinnon, 2018). To assess cellular uptake of hBNs, PC3 and PNT1A cells were treated with increasing doses of hBNs and hBN-Dox within 24 and 48h with and without US exposure. Doses of hBNs were given the cells according to amount of hBNs that is found inside hBN-Dox to fully clarify cellular uptake before and after Dox loading to hBNs. FSC vs SSC dot plots of PC3 cells treated for 24h were shown in Figure 23 and the cells that treated for 48h were shown in Figure 24. In these figures, the change in the spread of cells can be seen in response to treatment.

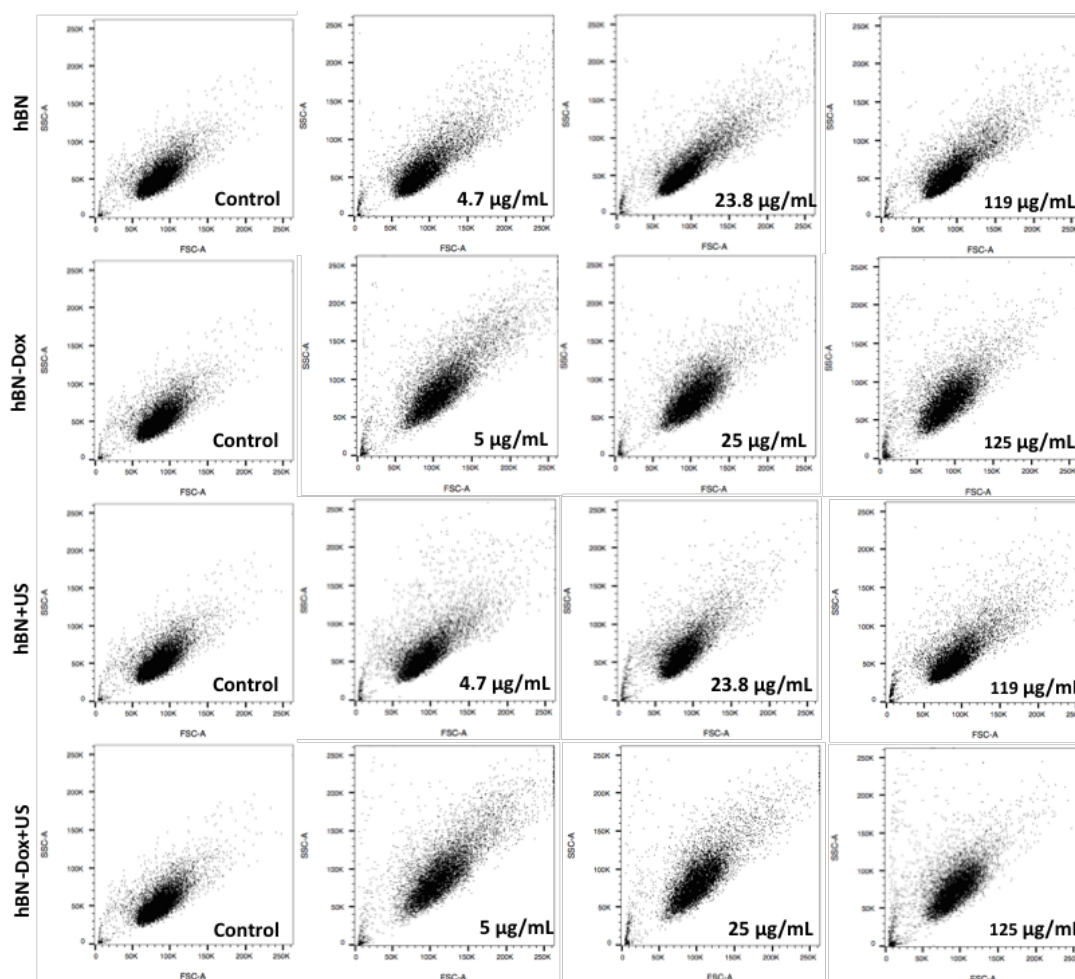


Figure 23. FSC vs SSC dot plots of cellular uptake analysis of hBNs and hBN-Dox with increasing concentrations by PC3 cells with and without US stimulation for 24h

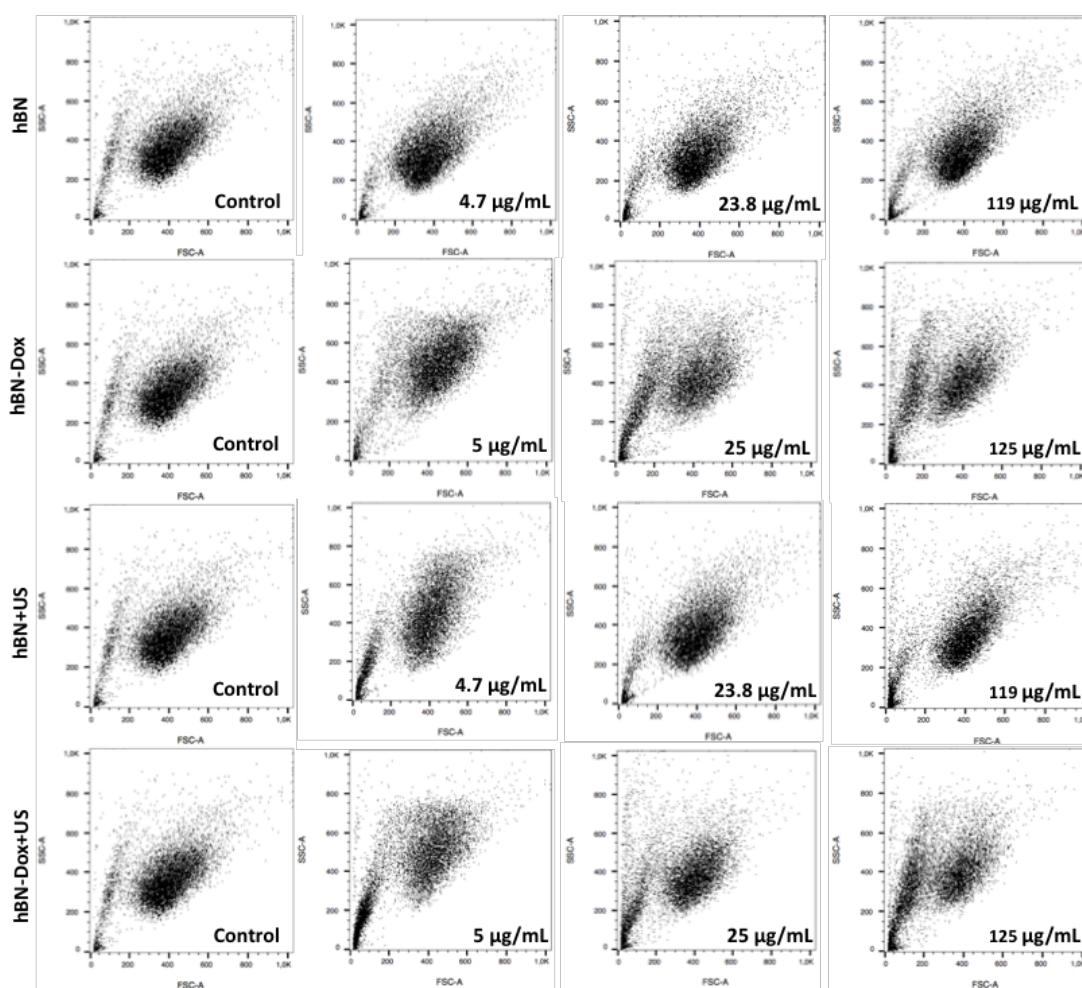


Figure 24. Comparison of FSC vs SSC dot plots of cellular uptake analysis of hBNs and hBN-Dox with increasing concentrations by PC3 cells with and without US stimulation for 48h

In order to determine of cellular uptake of hBNs and hBN-Dox according to granularity and internal complexity of PC3 cells, SSC signal change was calculated according to untreated control group and the results were shown as graphs in Figure 25. It can be seen from the graphs that within 24h all of the tested material uptakes were calculated as significant according to control group. While US exposure resulted with an increase in cellular uptake of hBN-Dox in 24h, it did not create similar effect for hBNs. On the contrary, US exposure to the cells within 48h increased the cellular uptake of hBNs while it decreased the uptake of hBN-Dox. In every tested concentration and time periods, hBN-Dox caused higher cellular uptake compared to hBNs. It means that, by Dox loading to hBNs cellular uptake was increased.

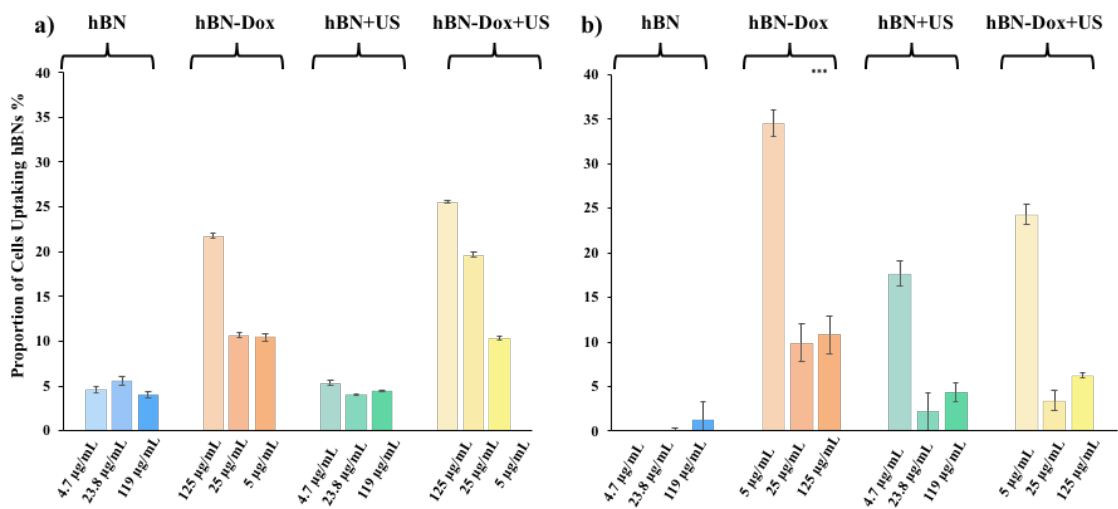


Figure 25. Cellular uptake analysis results for PC3 cells with increasing concentrations of hBNs and hBN-Dox. a) in 24h time period b) in 48h time period

FSC vs SSC dot plots of PNT1A cells treated 24h were shown in Figure 26 and the cells that treated 48h were shown in Figure 27. Change in the scatter and spread of cells can be observed in these figures in response to treatment.

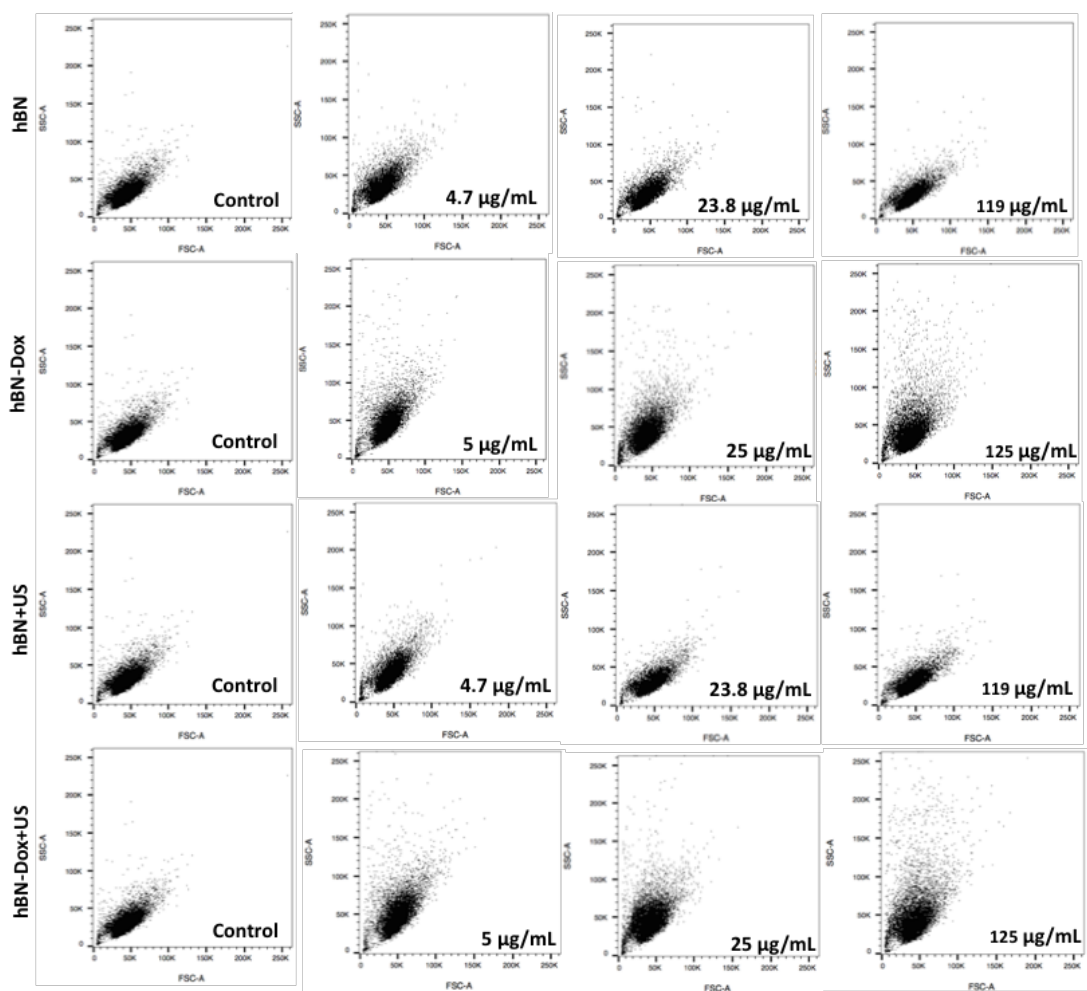


Figure 26. FSC vs SSC dot plots of cellular uptake analysis by PNT1A cells treated with increasing concentrations of hBNs and hBN-Dox within 24h time period with and without US stimulation

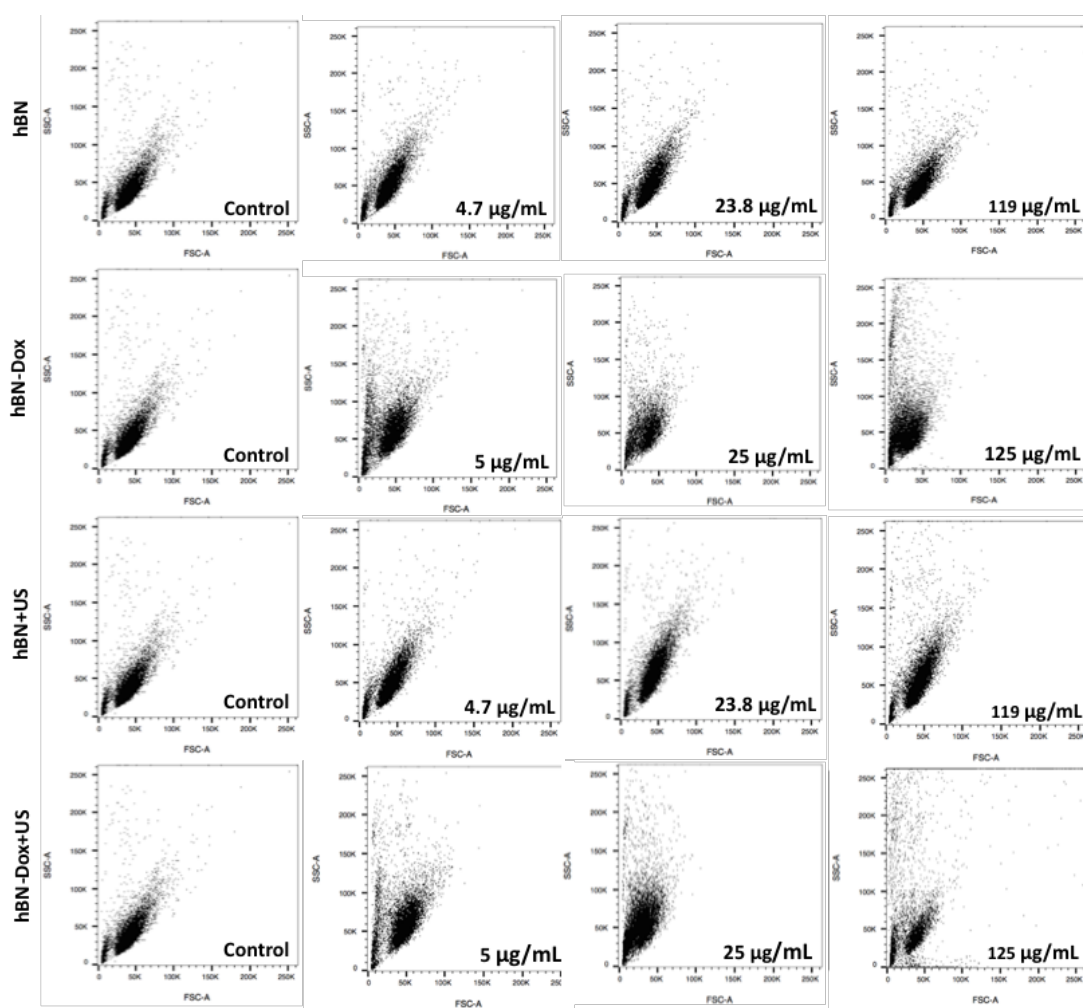


Figure 27. FSC vs SSC dot plots of cellular uptake analysis by PNT1A cells treated with increasing concentrations of hBNs and hBN-Dox within 48h time period with and without US stimulation

These results were summarized in a graph that is shown in Figure 28. The graphs were created according to SSC signal difference that is caused by granularity and internal complexity of cells in response to treatment. According to graphs, hBN-Dox in every tested concentration and time interval was uptake by the cells higher than hBNs. In 24 and 48h, all of the material uptakes were increased in response to US exposure with the exception of only hBN-Dox treatment in the concentration of 25 µg/mL in 24h.

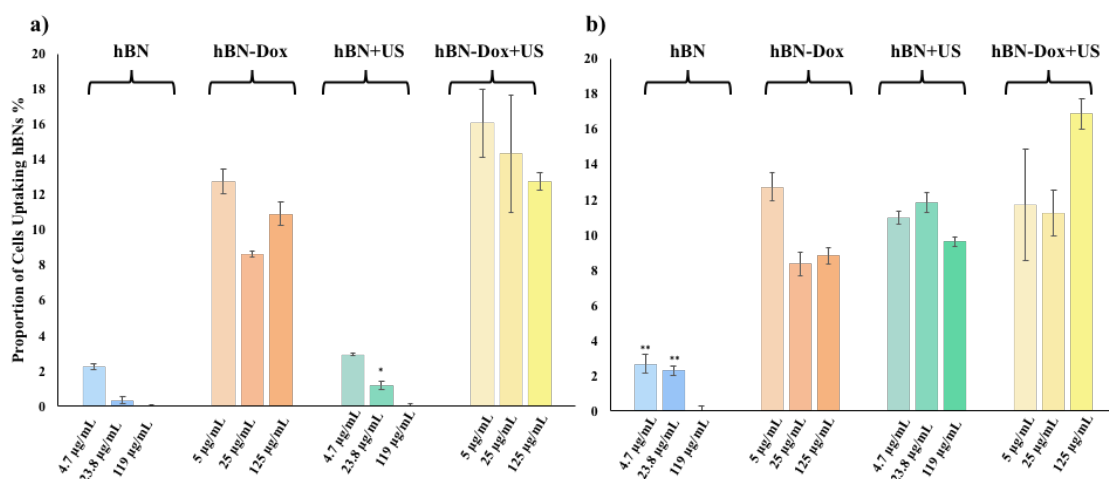


Figure 28. Cellular uptake analysis results for PNT1A cells with increasing concentrations of hBNs and hBN-Dox. Doses of hBNs treatment were chosen according to amount of hBNs present in hBN-Dox formulation within a) 24h, and b) 48h

Comparing uptake by PC3 and PNT1A cells in response to same treatment conditions, it can be concluded that in both of the cell's uptake of hBN-Dox was observed as higher than hBNs. It is known that, surface charge of a material has an important role in cellular physiology such as stimulation of stem cell osteogenic differentiation as well as cell-NM interactions (J. Li, X. Et al. 2015). Therefore, to gain deeper understanding of cellular uptake analysis and support existing data pH-induced zeta potential change of hBNs and hBN-Dox were measured by DLS. As mentioned before pH 3 and 5 was used to mimic acidic tumor microenvironment, pH 7.4 was used to mimic normal blood pH and cell culture conditions and pH 9 was used to see the effect in basic conditions. Results were shown in Figure 29. As seen in the Figure 29, hBNs were negatively charged in all of the experimented pH values. Due to the deprotonation at higher pH's including normal blood pH, hBNs exhibited more negative surface charge. With decreasing pH values, protonation effect causes hBNs to be less negative. As a result of the non-covalent interaction of Dox with hBNs, resulted NM-drug formulation carries more positive surface charges in all of the experimented pH values. Considering these results, it can be said that Dox loading to hBNs due to the surface charge change from negative to more positive value, will increase electrostatic interactions with negatively charged cell membrane. Moreover, in tumor microenvironment, acidity will give hBN-Dox a more positive surface charge resulting stronger electrostatic interactions with cells. Supporting that finding, a molecular dynamics study demonstrated that electrostatic interactions

between NPs and cell membrane plays more important role than hydrophobic interactions (Lin et al., 2010).

Moreover, charge density of NPs surface is directly proportional to penetration and disruption of cell membrane (Lin et al., 2010). Related to that, cationic NMs found creating more serious local damage on adhesion site of the cell membrane (Behzadi et al., 2017). A Computational experiment supporting that finding, demonstrated that NPs having positive surface charge are able to make a parallel contact with negatively charged cell membrane resulting a disruption of the bilayer by a maximal adhesion (Nangia & Sureshkumar, 2012). In detail, this change in the surface charge promotes cellular uptake by encouraging membrane-wrapping phenomena occur in positively charged NPs (Yang et al., 2016; Behzadi et al., 2017). Because, positively charged particle interacting with negatively charged cell surface heparan sulfate proteoglycans start phagocytic-like mechanisms to internalize particles (Vercauteren et al., 2010). In addition to that epithelial cell adhesion molecule is an epithelial cell biomarker exist in cell membrane having a critical role in cancer cell targeting and capture (Sun et al., 2017). And it is proved that particles with positive charge have higher binding capacity to different cancer cell lines with changing epithelial cell adhesion molecule expression levels (He et al., 2019).

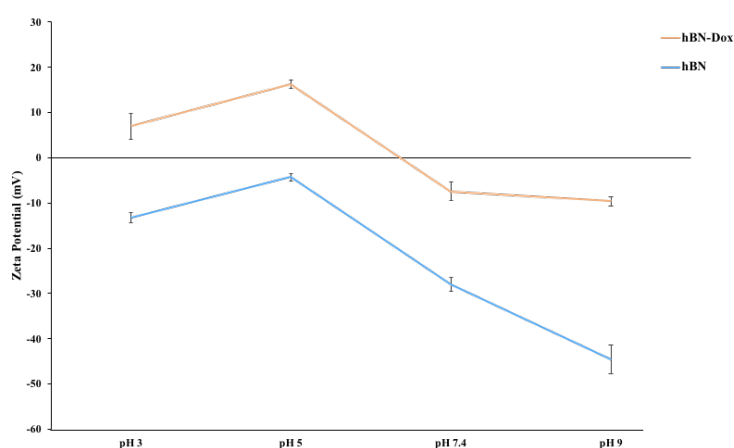


Figure 29. pH-dependent zeta potential change of hBNs and hBN-Dox

Considering all of these findings, for further experiments it was critical to assess intracellular Dox amount. And the effect of hBNs and US on that. Therefore, in next section, intracellular amount of Dox was determined.

3.7 Detection of Intracellular Concentration of Doxorubicin

An ideal drug carrier should effectively deliver its cargo inside the cell. Thus, to test hBNs further as nano-sized drug carrier, intracellular Dox amount was detected with the help of naturally fluorescent feature of Dox by FTIC channel of flow cytometer. In order to fully unravel the success of hBN-Dox to carry Dox inside the cells, Dox concentrations are tested according to amount of Dox that is found inside the hBN-Dox. Experiment was done with increasing concentrations of hBN-Dox and Dox, within 24 and 48h time intervals, with and without US exposure. In order to assess effect of US exposure, control groups did not get US. Histograms of hBN-Dox and Dox according to fluorescence signal coming from Dox inside the cells were shown in Figure 30. Calculated percentage of Dox containing PC3 cells according to untreated control group were shown as graphs in Figure 30. As seen in the graphs, in every tested time intervals and doses except for the highest dose (125 $\mu\text{g/mL}$) without US exposure in 24h and in 48h the highest dose with and without US), percentage of Dox containing cells were higher when the cells treated with hBN-Dox. With increasing time, Dox containing cells were increased in every tested concentration and tested material. Percentage of Dox containing cells were directly proportional to the treatment concentration. With increasing concentrations, Dox containing cells were increased. With US in 24h, Dox containing cells reduced compared to groups that treated same material in the same conditions without US exposure except for the lowest doses of hBN-Dox (5 $\mu\text{g/mL}$) and Dox (0.2 $\mu\text{g/mL}$). In 48h, same effect was observed except for the highest doses of hBN-Dox and Dox (5.9 $\mu\text{g/mL}$). In the lowest concentration (5 $\mu\text{g/mL}$), with percentage of Dox containing cells were higher with treatment of hBN-Dox and US increased this effect resulting with the highest percentage of Dox containing cells in that concentration in 24h. Also, PC3 cells that were exposure to US have higher amount of Dox inside when they are treated with hBN-Dox than Dox alone.

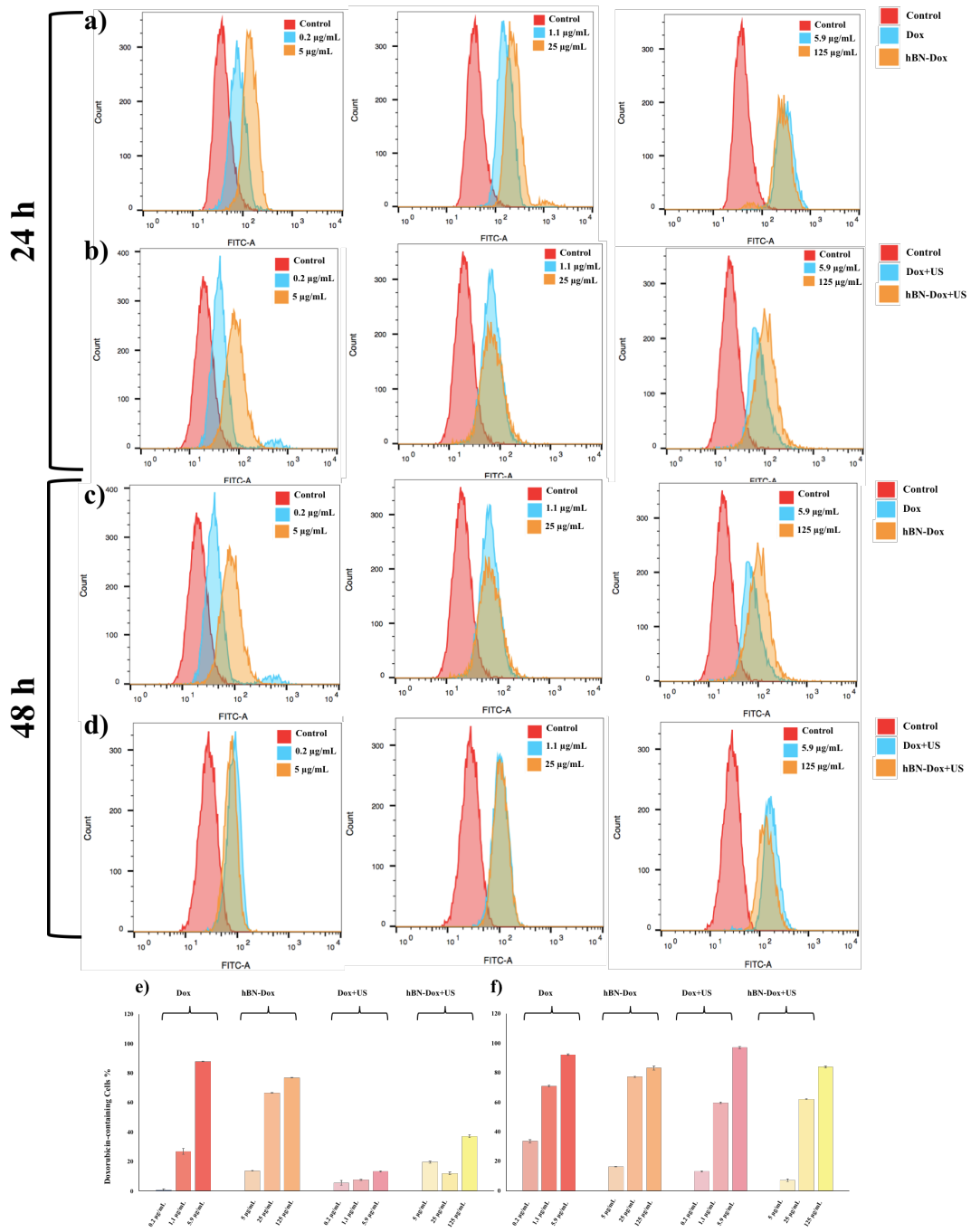


Figure 30. Detected of Dox containing cells as percentage. Histograms of hBN-Dox and Dox according to fluorescence signal coming from Dox inside PC3 cells that treated with hBN-Dox (5, 25, 125 $\mu\text{g/mL}$) and Dox (0.2, 1.1, 5.9 $\mu\text{g/mL}$) in 24h a) without US exposure b) with US exposure, in 48h c) without US exposure d) with US exposure. Calculated percentage of Dox-containing PC3 cells according to fluorescence signal of Dox after hBN-Dox and Dox treatment with and without US exposure within e) 24h f) 48h

In Figure 31, histograms of hBN-Dox and Dox according to fluorescence signal coming from Dox inside the PNT1A cells that treated with hBN-Dox and Dox were shown. According to untreated control group percentage of Dox containing cells were calculated and shown in Figure 31. In every tested time and treatment doses, percentage of the cells decreased with decreasing concentration. Also, with increasing time, percentage of Dox containing the cells decreased. Within 24h, PNT1A cells that were exposure to US have higher amount of Dox inside when they are treated with hBN-Dox instead of Dox alone with help of US. In 48h, while US almost did not change percentage of Dox containing the cells with the treatment of Dox, the cells that treated with hBN-Dox decreased with US.

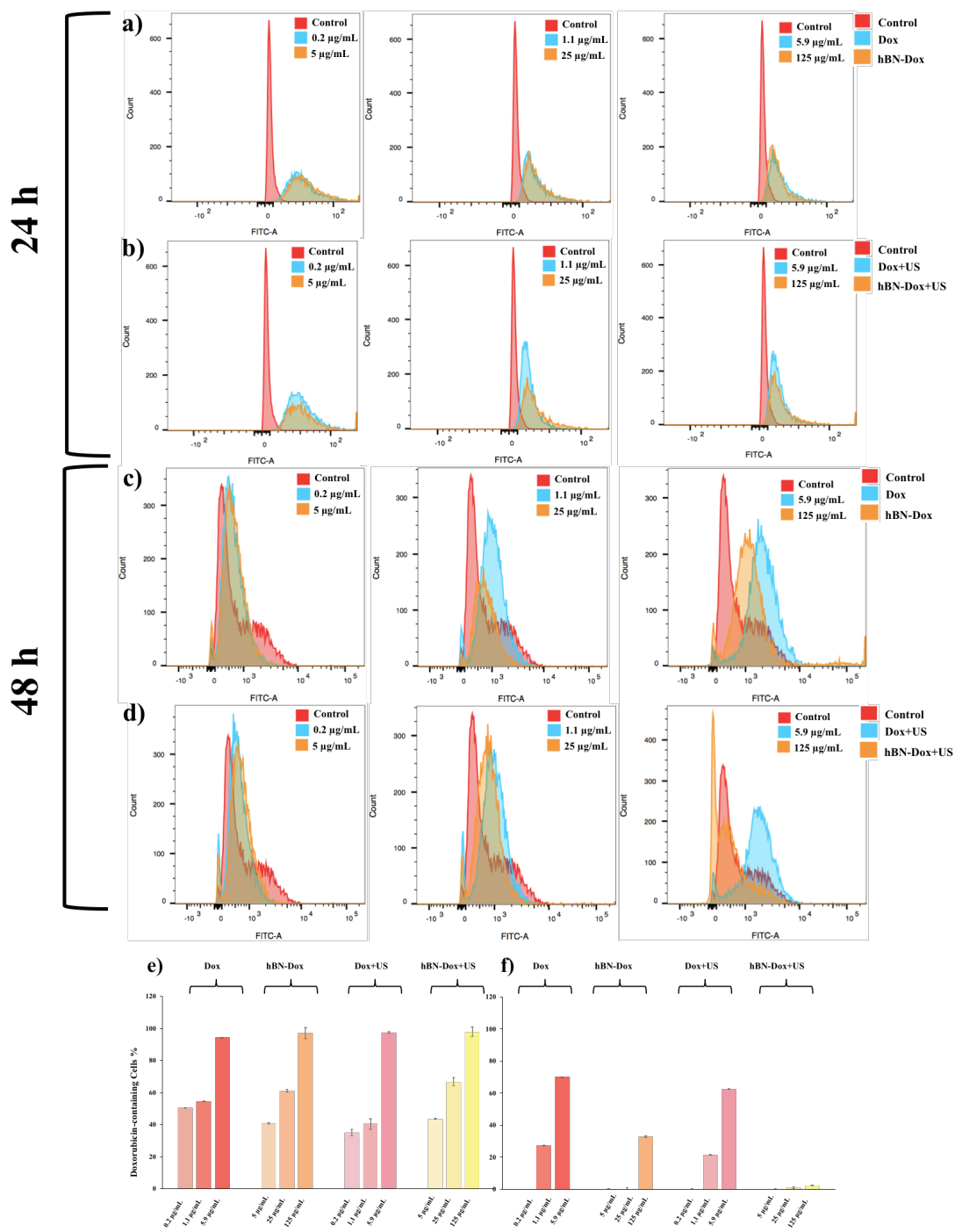


Figure 31. Detected of Dox containing cells as percentage. Histograms of hBN-Dox and Dox according to fluorescence signal coming from Dox inside the PNT1A cells that treated with hBN-Dox (5, 25, 125 $\mu\text{g/mL}$) and Dox (0.2, 1.1, 5.9 $\mu\text{g/mL}$) in 24h a) without US exposure b) with US exposure, in 48h c) without US exposure d) with US exposure. Calculated percentage of Dox-containing cells according to fluorescence signal of Dox after hBN-Dox and Dox treatment with and without US exposure within e) 24h f) 48h

3.8 Colony Formation Assay

Colony formation assay mainly test potentially lethal damages that caused by the treatment procedure. This assay carries a critical importance for the field of cancer research. Because colony formation capabilities of cancer cells are related to tumor formation ability by testing genotoxic and cytotoxic effect of a potential treatment. After exposure to hBNs, hBN-Dox and Dox with and without US stimulation; cell's reproductive death was analyzed by this assay. After all of the treatment procedures, cells that protect the ability of colony production was detected. For the accurate assessment of clonogenicity, cells were seeded at very low density. For visualization, cells were fixed with glutaraldehyde and stained with crystal violet dye to count them. In Figure 32, results of colony formation assay and calculated percentage of colony number values of hBNs, hBN-Dox and Dox in PC3 cells were shown. According to the figure, the cells that treated with increasing concentrations of hBNs were survived by forming colonies and US decreased colony number % in every tested concentration. Treatment with hBN-Dox and Dox caused significant decrease in colony number % compared to untreated control and same effect was observed with US. Moreover, while the lowest concentration of Dox treatment allows colony formation of PC3 cells 11 % without US and 10 % with US, hBN-Dox at the lowest concentration did not allow almost any colony formation. With this experiment, hBN-Dox was proved as effective by inhibiting formation of colonies on cancer cell line.

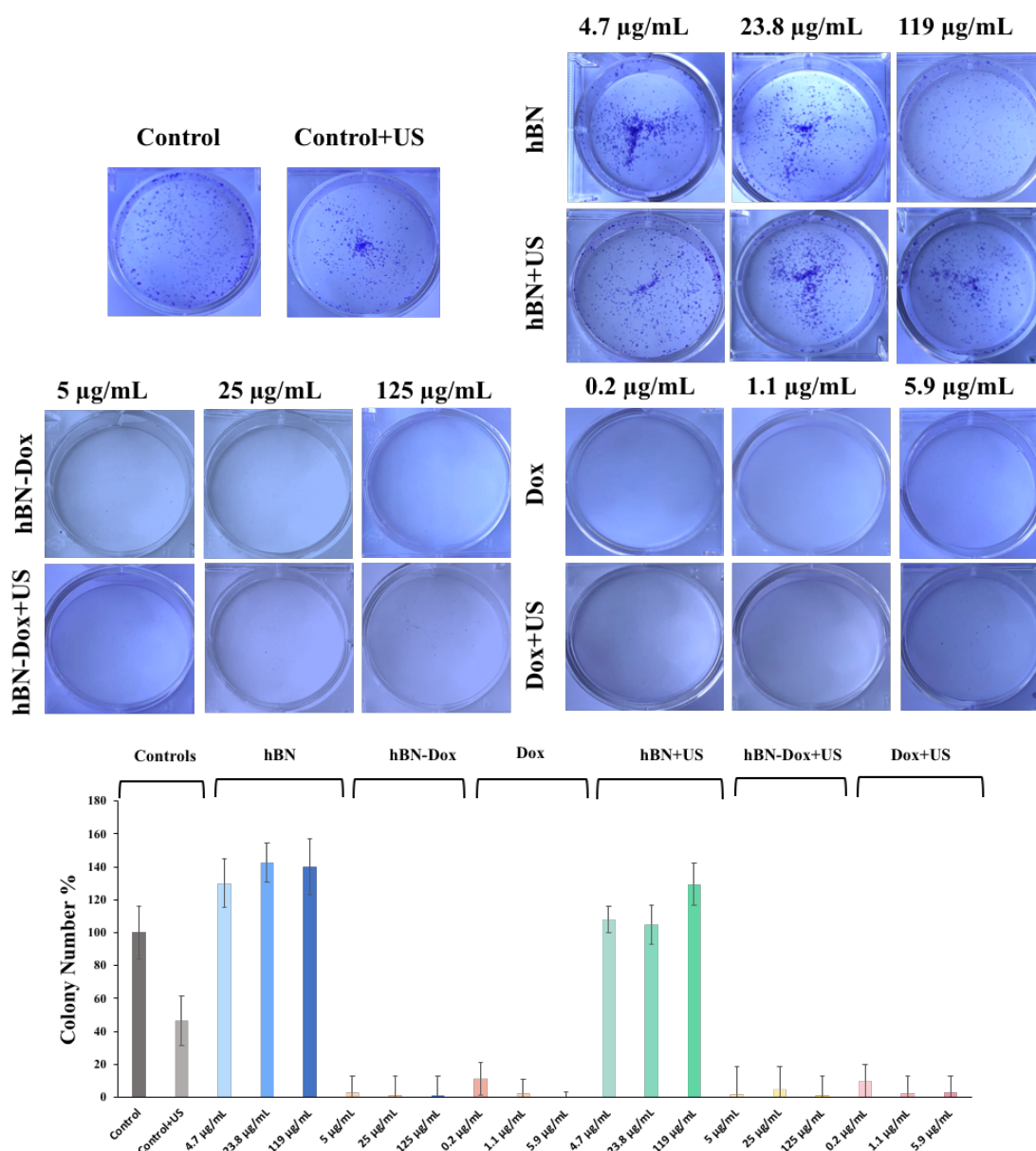


Figure 32. Results of colony formation assay and calculated colony number % values of hBNs, hBN-Dox and Dox in PC3 cells

Colony number was tested on PNT1A cell line after treatment with hBNs, hBN-Dox and Dox and the results were shown in Figure 33. Some of the PNT1A cells were survived by forming smaller-sized colonies compared to PC3 cells. According to the figure, the cells that treated with hBNs survived and formed colonies with and without US. Following to treatment with hBN-Dox and Dox, colony number % significantly reduced compared to untreated control group. But still colony numbers after treatments with these materials were higher than PC3 cell line. Also, while almost any colonies were observed after

treatment with hBN-Dox on PC3 cells, in PNT1A cells up to 22 % colony formation was observed as a promising result for survival of healthy cells in response to treatment.

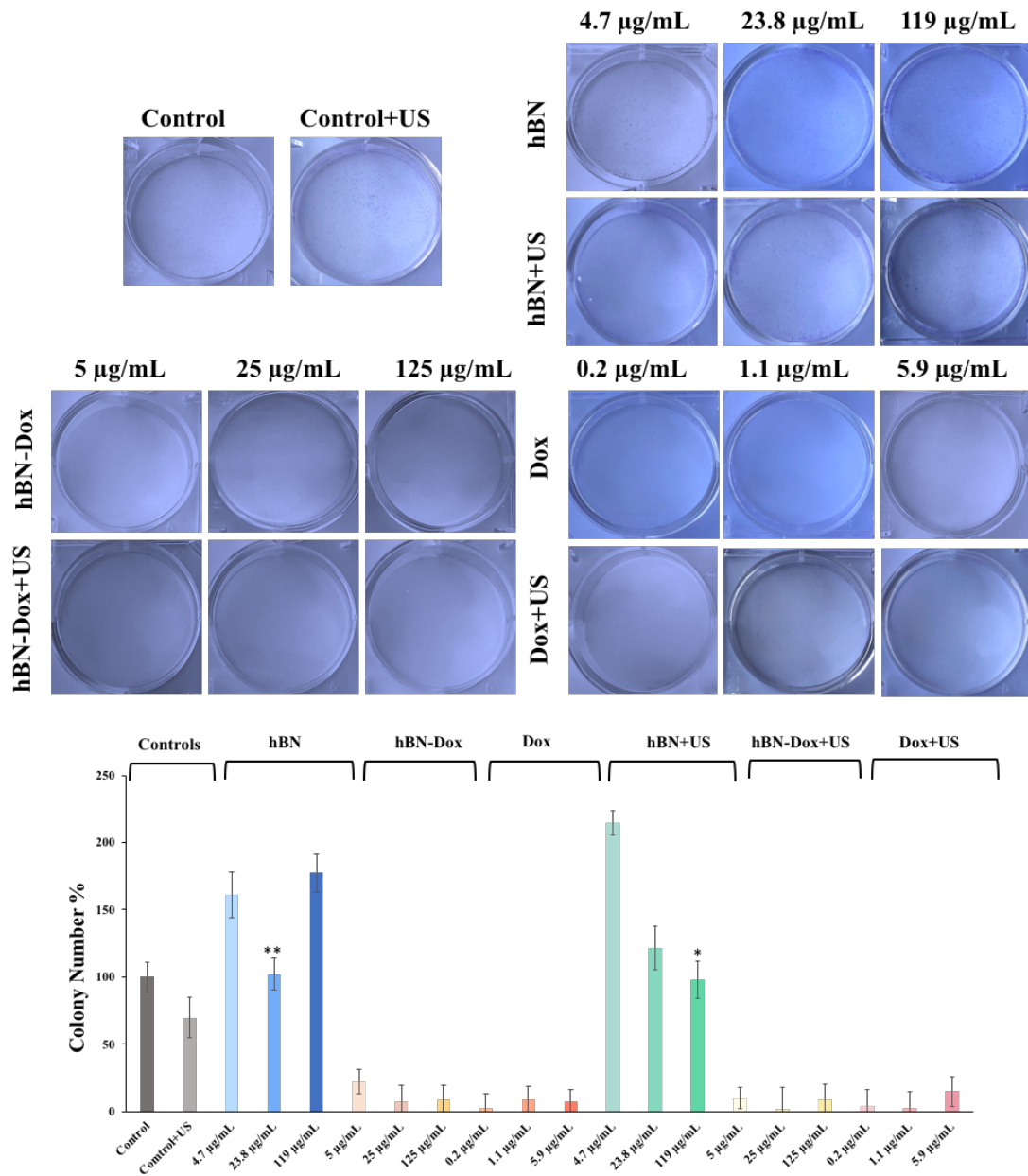


Figure 33. Results of colony formation assay and calculated colony number % values of hBNs, hBN-Dox and Dox in PNT1A cells

3.9 Identification of Apoptotic and Necrotic Cells

PI is a fluorescent dye that has ability to bind DNA, frequently used for cell viability

detection and considered as a marker of cell membrane permeability. Annexin V binds phosphatidylserine exist in outer membrane of apoptotic cells (Cummings & Schnellmann, 2004). Apoptosis necrosis assay use both of the dyes to detect death mechanism of cells by testing cells simultaneously. Cells that were both negative for PI and Annexin V are healthy cells. When the cells were both positive for PI and Annexin V, they were considered as late apoptotic cells. When these cells were negative for PI and positive for Annexin V, these cells were considered as early apoptotic cells and the cells that are positive for PI negative for Annexin V considered as necrotic cells (Lakshmanan & Batra, 2013). With this assay cell death of PC3 and PNT1A cells were measured after treatment with hBNs, hBN-Dox and Dox within 24h. Effect of US exposure was assessed, and control groups did not get US. Figure 34 represents the cell death measurement of PC3 cells after treatment with hBNs and hBN+US. According to results, hBNs without US exposure did not cause necrosis. With increasing concentrations, it caused an increase in late apoptosis and decrease in early apoptosis. In the highest concentration (119 $\mu\text{g/mL}$), percentage of early apoptosis was 47.7 %, late apoptosis was 42 %. Early apoptosis was higher in every tested concentration. When the cells were exposure US, % necrosis reached up to 11 %. Treatment with hBNs+US did not caused necrosis. But US exposure increased percentage of late apoptosis in every tested concentration. Percentage of late apoptosis was higher than percentage of early apoptosis in every tested concentration with US. In the highest concentration percentage of late apoptosis reached up to 50.5 % and early apoptosis was 46.8 %.

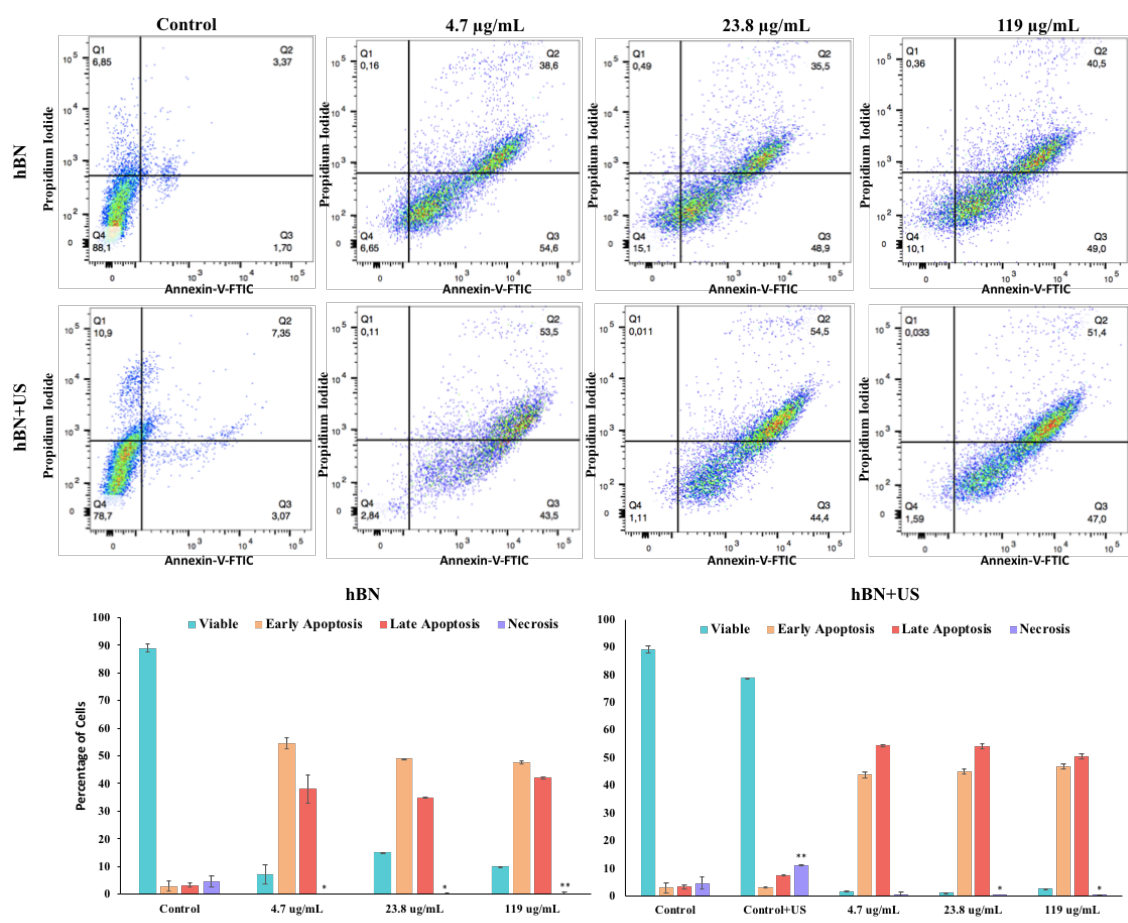


Figure 34. Results of apoptosis necrosis detection assay on PC3 cell line with increasing doses of hBNs without US stimulation and with US stimulation. Control group did not treat with hBNs and exposure US and Control+US group did not treat with hBNs but exposure US. In dot plots, Q1 zone represents necrosis, Q2 zone represents late apoptosis, Q3 zone represents early apoptosis and Q4 zone represents viability (normality)

PC3 cells treated with hBN-Dox death was measured and the results were shown in Figure 35. As seen in graphs and dot plots, hBN-Dox did not cause necrosis on PC3 cells with and without US. In concentrations of 5, 25 µg/mL, percentage of early apoptosis was higher than late apoptosis. In the highest concentration (125 µg/mL), late apoptotic cells were higher than early apoptotic cells with 56.1 %. When the cells were treated with hBNs +US, late apoptotic cells increased in every tested concentration reaching up to 61 % in the highest concentration.

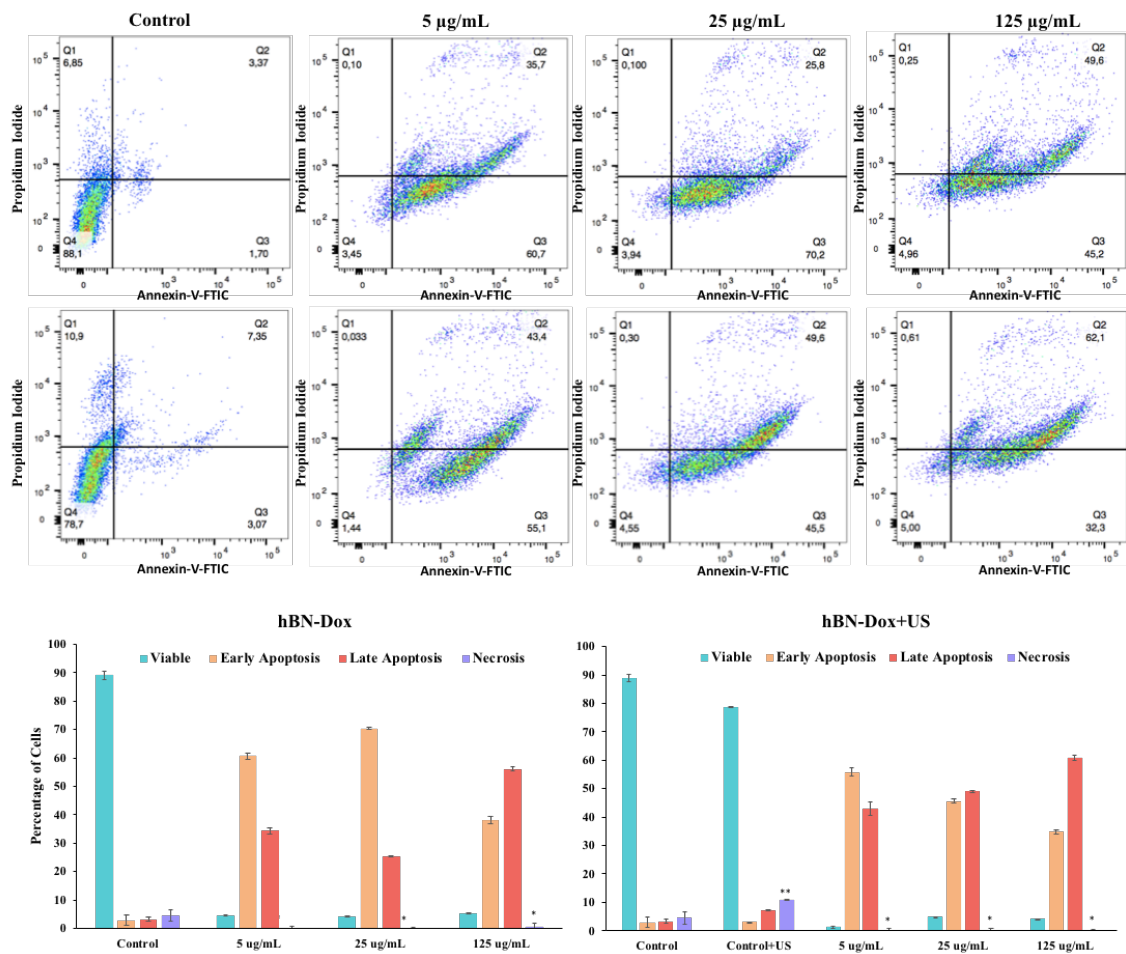


Figure 35. Results of apoptosis necrosis detection assay on PC3 cell line with increasing doses of hBN-Dox without US stimulation and with US stimulation. Control group did not treat with hBN-Dox and exposure US and Control+US group did not treat with hBN-Dox but exposure US. In dot plots, Q1 zone represents necrosis, Q2 zone represents late apoptosis, Q3 zone represents early apoptosis and Q4 zone represents viability (normality)

In Figure 36, the cell death measurement was shown after treatment with Dox and Dox US. Without US, in the highest concentration (5.9 µg/mL), Dox treatment caused 69 % early apoptotic cells, 6 % necrotic cells and 3 % late apoptotic cells formation. With decreasing dose, percentage of early apoptosis decreased and late apoptosis increased. With US, early apoptosis reached 87 % and decreased with decreasing concentrations up to 43 %. In the lowest dose (0.2 µg/mL), late apoptotic cells were higher than early apoptotic cells.

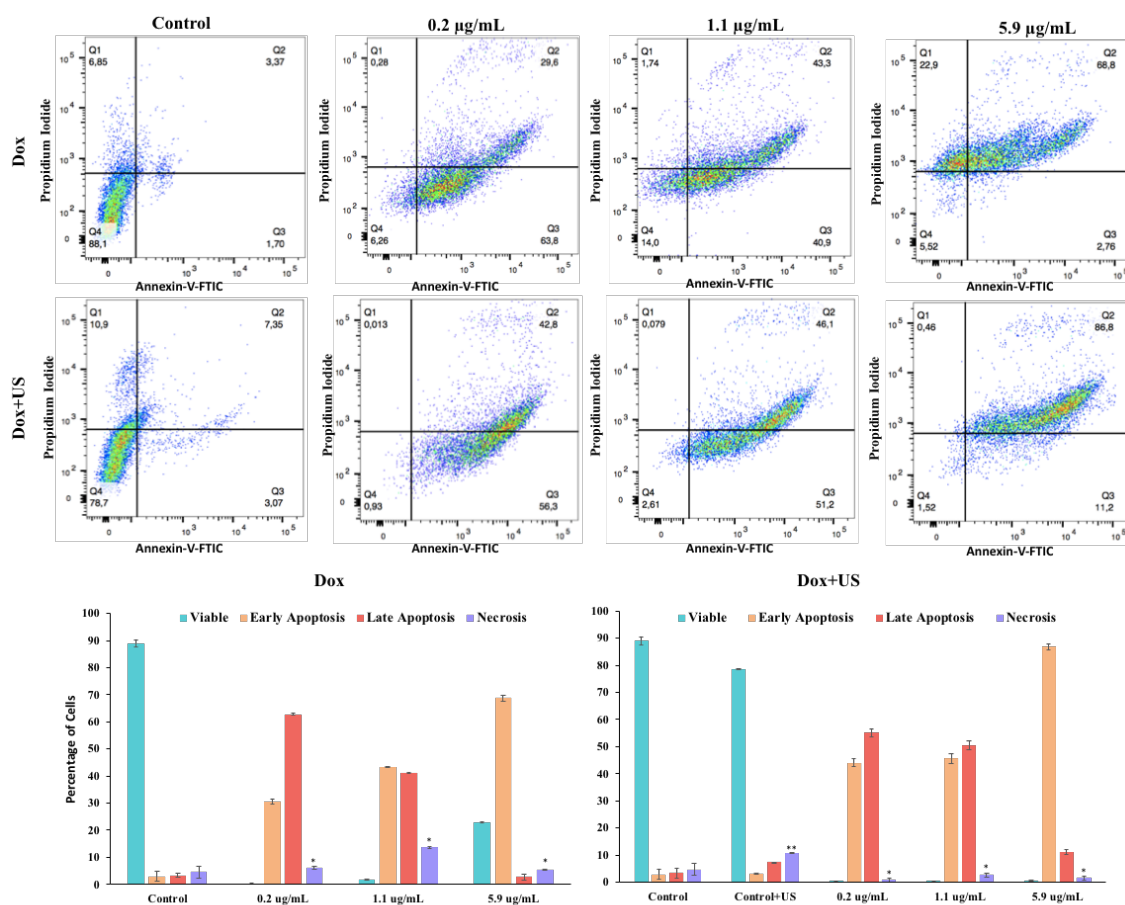


Figure 36. Results of apoptosis necrosis detection assay on PC3 cell line with increasing doses of Dox without US stimulation and with US stimulation. Control group did not treat with Dox and exposure US and Control+US group did not treat with Dox but exposure US. In dot plots, Q1 zone represents necrosis, Q2 zone represents late apoptosis, Q3 zone represents early apoptosis and Q4 zone represents viability (normality)

To test the effects hBNs and hBNs+US on PNT1A, results were calculated according to untreated control and shown in Figure 37. As seen in the graphs and dot plots, the viable cells were higher in every tested concentration, with and without US. hBNs treatment on PNT1A cells caused 27 % necrotic cell formation and this percentage of necrotic cells decreased with decreasing concentration up to 6 %. Percentage of late apoptotic cells was 4 % and early apoptotic cells were 1 % in the highest concentration. In the lowest concentration, both of them was around 2 %.

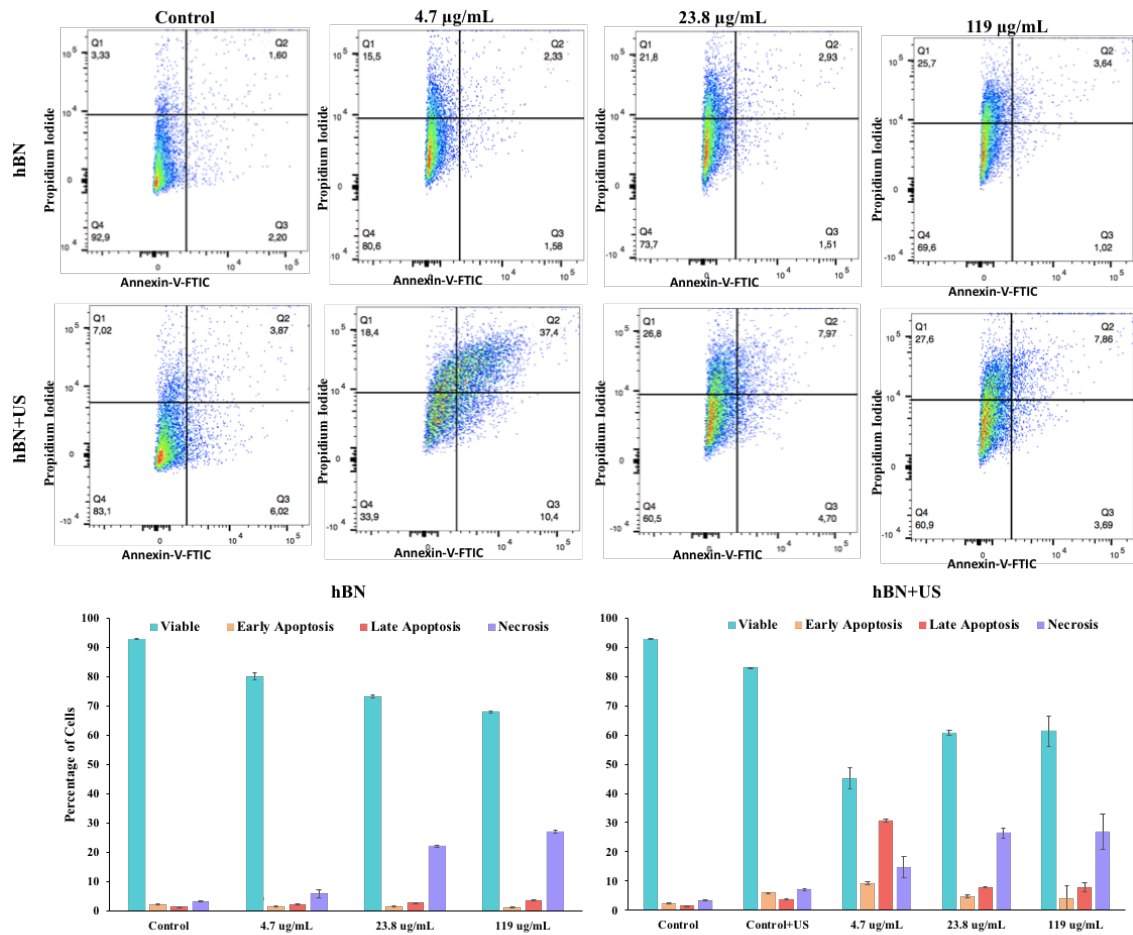


Figure 37. Results of apoptosis necrosis detection assay on PNT1A cell line with increasing doses of hBNs without US stimulation and with US stimulation. Control group did not treat with hBNs and exposure US and Control+US group did not treat with hBNs but exposure US. In dot plots, Q1 zone represents necrosis, Q2 zone represents late apoptosis, Q3 zone represents early apoptosis and Q4 zone represents viability (normality)

Figure 38 represents the results of cell death measurement of PNT1A cells after treatment with hBN-Dox and hBN-Dox+US with decreasing concentrations. According to results, percentage of early apoptotic cells was higher compared to live, necrotic and late apoptotic cells in every tested concentration, with and without US. Necrotic cells were not observed in any tested condition with hBN-Dox treatment.

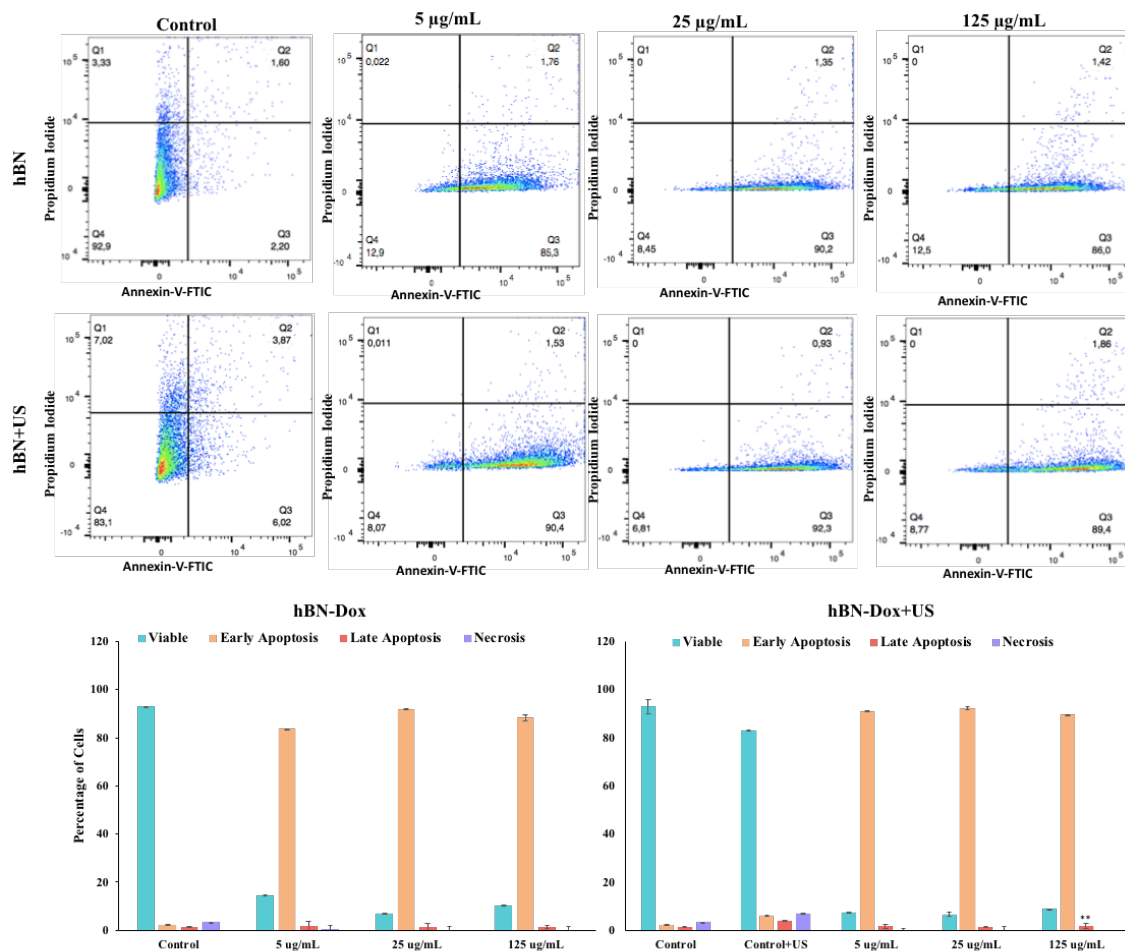


Figure 38. Results of apoptosis necrosis detection assay on PNT1A cell line with increasing doses of hBN-Dox without US stimulation and with US stimulation. Control group did not treat with hBN-Dox and exposure US and Control+US group did not treat with hBN-Dox but exposure US. In dot plots, Q1 zone represents necrosis, Q2 zone represents late apoptosis, Q3 zone represents early apoptosis and Q4 zone represents viability (normality)

Effect of Dox treatment on cell death mechanism was investigated and shown in Figure 39. Percentage of apoptotic cells were higher than live, late apoptotic and necrotic cells in every tested condition of Dox with and without US. Also, any necrotic cells were observed.

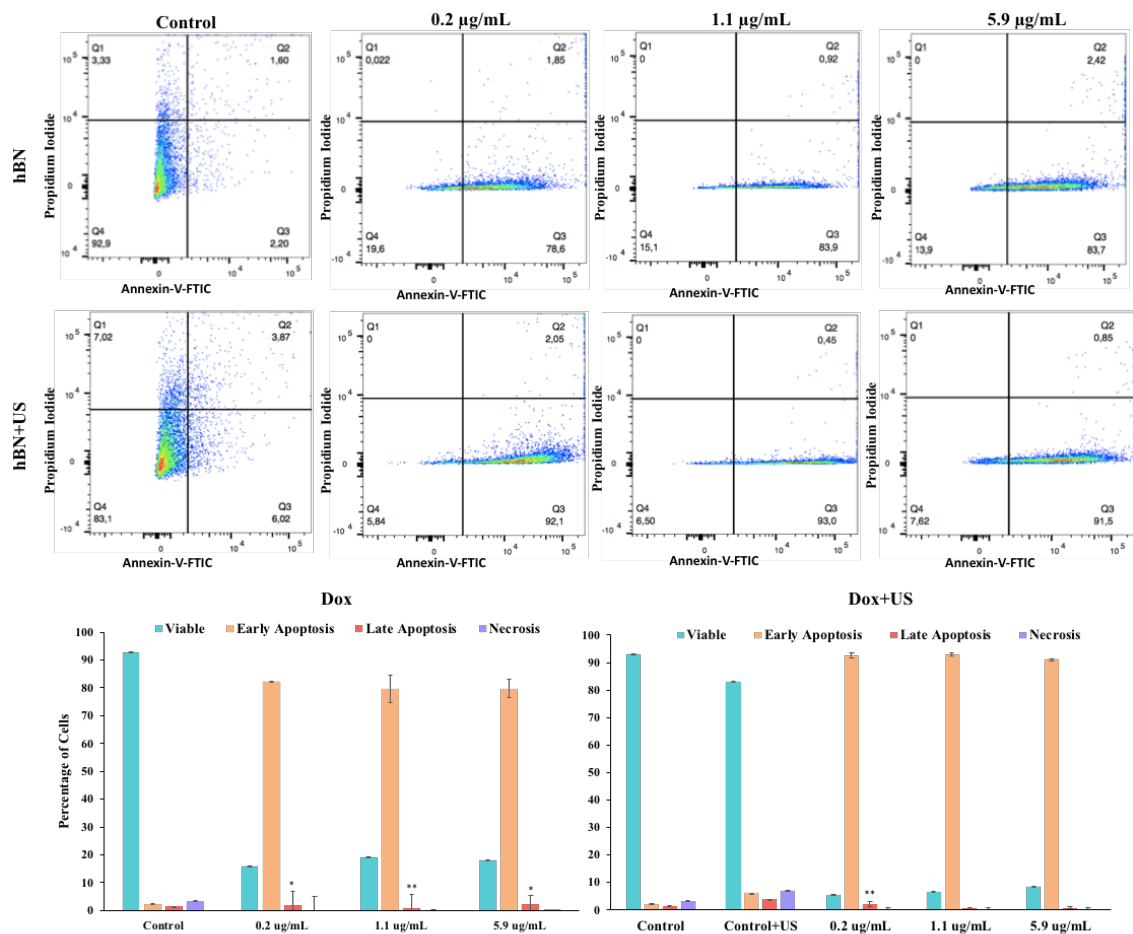


Figure 39. Results of apoptosis necrosis detection assay on PNT1A cell line with increasing doses of Dox without US stimulation and with US stimulation. Control group did not treat with Dox and exposure US and Control+US group did not treat with Dox but exposure US. In dot plots, Q1 zone represents necrosis, Q2 zone represents late apoptosis, Q3 zone represents early apoptosis and Q4 zone represents viability (normality)

4. CONCLUSION AND FUTURE PERSPECTIVES

In this thesis, the piezoelectric hBNs were synthesized successfully by CVD technique by using BA and ammonia as precursors on a SiC substrate. The piezoelectricity of synthesized hBNs was tested with PRFM measurements. The piezoelectric hBNs which was activated by US stimulation was used as a drug carrier system to inhibit prostate cancer cell proliferation. US was used as a safe and effective tool and external mechanical stimuli to active piezoelectricity of hBNs. Dox as a model anticancer drug loaded to hBNs with an efficiency of 99.8 % by through weak molecular interactions. The degradation profile of hBNs and hBN-Dox was analyzed by ICP-OES and it was found that hBN-Dox released its the B content slower than hBNs. Then, the release profiles of the loaded Dox from hBN-Dox were determined at varying pHs and US exposure. *In vitro* experiments, the potential of hBN-Dox on PC3 prostate cancer cells and PNT1A normal adult prostatic epithelial cells were tested. It was found that hBN-Dox lowered the effective dose of Dox by inhibiting proliferation of cancer cells more effectively than the case for the healthy cells. Supporting to these findings, ROS generation was found as higher in PC3 cells than PNT1A cells in the same treatment conditions and US exposure caused higher ROS generation in both of the cell lines. In the further experiments, hBN-Dox was uptaken by the cells higher than hBNs suggesting hBNs as a potential drug carrier for Dox. Moreover, hBN-Dox hindered colony formation ability of cancer cells. Cell death mechanism after treatment with hBN-Dox was detected as early and late apoptosis depending on the treatment dose and US exposure to PC3 cells caused an increase in the percentage of late apoptotic cells.

Despite many studies on the use of NMs in cancer treatment, very few of them have been found suitable for use in clinical applications. In order to improve this situation, NM-cell interaction should be studied more. Not only the cell interaction but also the interaction with the tumor microenvironment should be examined in detail. Despite the tested strategies worked successfully in the aim of creating a targeted and stimuli responsive effect, these capabilities of hBN-Dox should be further developed. On the other hand, the discovery of new physical or molecular biomarkers to better target cancer cells with NMs

could create a breakthrough in targeted therapies. In addition, potential of hBN-Dox should be tested with *in vivo* experiments including accumulation and retention of hBN-Dox in tumor site. Finally, piezoelectric effect created by hBN-Dox should be clarified on tumor growth.

BIBLIOGRAPHY

Alexe, M., Harnagea, C., & Hesse, D. (2004). Non-conventional micro-and nanopatterning techniques for electroceramics. *Journal of Electroceramics*, 12(1), 69-88.

Amjad, M. T., Chidharla, A., & Kasi, A. (2021). Cancer chemotherapy. In StatPearls [Internet]. StatPearls Publishing.

Ares, P., Cea, T., Holwill, M., Wang, Y. B., Roldán, R., Guinea, F., ... & Woods, C. R. (2020). Piezoelectricity in monolayer hexagonal boron nitride. *Advanced Materials*, 32(1), 1905504.

Aydin, N., Turkez, H., Tozlu, O. O., Arslan, M. E., Yavuz, M., Sonmez, E., ... & Mardinoglu, A. (2022). Ameliorative Effects by Hexagonal Boron Nitride Nanoparticles against Beta Amyloid Induced Neurotoxicity. *Nanomaterials*, 12(15), 2690.

Aykul, S., & Martinez-Hackert, E. (2016). Determination of half-maximal inhibitory concentration using biosensor-based protein interaction analysis. *Analytical biochemistry*, 508, 97–103. <https://doi.org/10.1016/j.ab.2016.06.025>

Baghban, R., Roshangar, L., Jahanban-Esfahlan, R., Seidi, K., Ebrahimi-Kalan, A., Jaymand, M., ... & Zare, P. (2020). Tumor microenvironment complexity and therapeutic implications at a glance. *Cell Communication and Signaling*, 18(1), 1-19.

Bagherifam, S., Skjeldal, F. M., Griffiths, G., Mælandsmo, G. M., Engebråten, O., Nyström, B., ... & Hasirci, N. (2015). pH-responsive nano carriers for doxorubicin delivery. *Pharmaceutical Research*, 32(4), 1249-1263.

Ballato, A. (1995). Piezoelectricity: old effect, new thrusts. *IEEE transactions on ultrasonics, ferroelectrics, and frequency control*, 42(5), 916-926.

Bansal, R., Singh, R., & Kaur, K. (2021). Quantitative analysis of doxorubicin hydrochloride and arterolane maleate by mid IR spectroscopy using transmission and reflectance modes. *BMC chemistry*, 15(1), 1-11.

Barranco, W. T., & Eckhert, C. D. (2004). Boric acid inhibits human prostate cancer cell proliferation. *Cancer letters*, 216(1), 21-29.

Barranco, W. T., Hudak, P. F., & Eckhert, C. D. (2007). Evaluation of ecological and *in vitro* effects of boron on prostate cancer risk (United States). *Cancer Causes & Control*, 18(1), 71-77.

Behzadi, S., Serpooshan, V., Tao, W., Hamaly, M. A., Alkawareek, M. Y., Dreaden, E. C., ... & Mahmoudi, M. (2017). Cellular uptake of nanoparticles: journey inside the cell. *Chemical Society Reviews*, 46(14), 4218-4244.

Bettinger, C. J., Bruggeman, J. P., Misra, A., Borenstein, J. T., & Langer, R. (2009). Biocompatibility of biodegradable semiconducting melanin films for nerve tissue engineering. *Biomaterials*, 30(17), 3050-3057.

Burr, H. S., & Northrop, F. S. C. (1939). Evidence for the existence of an electro-dynamic field in living organisms. *Proceedings of the National Academy of Sciences*, 25(6), 284-288.

Cafarelli, A., Marino, A., Vannozzi, L., Puigmartí-Luis, J., Pané, S., Ciofani, G., & Ricotti, L. (2021). Piezoelectric nanomaterials activated by ultrasound: the pathway from discovery to future clinical adoption. *ACS nano*, 15(7), 11066-11086.

Cerqueira, B. B. S., Lasham, A., Shelling, A. N., & Al-Kassas, R. (2015). Nanoparticle therapeutics: Technologies and methods for overcoming cancer. *European Journal of Pharmaceutics and Biopharmaceutics*, 97, 140-151.

Chamchoy, K., Pakotiprapha, D., Pumirat, P., & Leartsakulpanich, U. (2019). Application of WST-8 based colorimetric NAD (P) H detection for quantitative dehydrogenase assays. *BMC biochemistry*, 20(1)

Chen-Glasser, M., Li, P., Ryu, J., & Hong, S. (2018). Piezoelectric materials for medical applications. *Piezoelectricity-organic and inorganic materials and applications*, 125-145.

Chen, C., Bai, X., Ding, Y., & Lee, I. S. (2019). Electrical stimulation as a novel tool for regulating cell behavior in tissue engineering. *Biomaterials research*, 23(1), 1-12.

Chen, T., Li, M., & Liu, J. (2018). π - π stacking interaction: a nondestructive and facile means in material engineering for bioapplications. *Crystal Growth & Design*, 18(5), 2765-2783.

Chen, X., Wu, P., Rousseas, M., Okawa, D., Gartner, Z., Zettl, A., & Bertozzi, C. R. (2009). Boron nitride nanotubes are noncytotoxic and can be functionalized for interaction with proteins and cells. *Journal of the American Chemical Society*, 131(3), 890-891.

Chen, Y., Tan, C., Zhang, H., & Wang, L. (2015). Two-dimensional graphene analogues for biomedical applications. *Chemical Society Reviews*, 44(9), 2681-2701.

Cheng, C. C., Muhabie, A. A., Huang, S. Y., Wu, C. Y., Gebeyehu, B. T., Lee, A. W., ... & Lee, D. J. (2019). Dual stimuli-responsive supramolecular boron nitride with tunable physical properties for controlled drug delivery. *Nanoscale*, 11(21), 10393-10401.

Cheng, Z., Li, M., Dey, R., & Chen, Y. (2021). Nanomaterials for cancer therapy: Current progress and perspectives. *Journal of Hematology & Oncology*, 14(1), 1-27.

Ciofani, G., Danti, S., D'Alessandro, D., Ricotti, L., Moscato, S., Bertoni, G., ... & Menciasci, A. (2010). Enhancement of neurite outgrowth in neuronal-like cells following boron nitride nanotube-mediated stimulation. *ACS nano*, 4(10), 6267-6277.

Ciofani, G., Danti, S., Genchi, G. G., Mazzolai, B., & Mattoli, V. (2013). Boron nitride nanotubes: Biocompatibility and potential spill-over in nanomedicine. *Small*, 9(9-10), 1672-1685.

Cummings, B. S., & Schnellmann, R. G. (2004). Measurement of cell death in mammalian cells. *Current protocols in pharmacology*, Chapter 12, 10.1002/0471141755.ph1208s25. <https://doi.org/10.1002/0471141755.ph1208s25>

Curie, J., & Curie, P. (1880). Sur l'électricité polaire dans les cristaux hémihédres à faces inclinées. *CR Acad Sci Gen*, 91, 383-6.

Curie, J., & Curie, P. (1881). Contractions et dilatations produites par des tensions électriques dans les cristaux hémihédres à faces inclinées. *Compt. Rend*, 93, 1137-1140.

Dai, J., Wang, Y., Xu, Z., & He, L. (2018). Degradation of Boron Nitride Interfacial Coatings Fabricated by Chemical Vapor Infiltration on SiC Fibers under Ambient Air/Room Temperature Conditions. *Ceramics International*. doi:10.1016/j.ceramint.2018.12

Danaei, M., Dehghankhold, M., Ataei, S., Hasanzadeh Davarani, F., Javanmard, R., Dokhani, A., Khorasani, S., & Mozafari, M. R. (2018). Impact of Particle Size and Polydispersity Index on the Clinical Applications of Lipidic Nanocarrier Systems. *Pharmaceutics*, 10(2), 57. <https://doi.org/10.3390/pharmaceutics10020057>

David Foglesong, P., Reckord, C., & Swink, S. (1992). Doxorubicin inhibits human DNA topoisomerase I. *Cancer chemotherapy and pharmacology*, 30(2), 123-125.

Doan, N., Reher, P., Meghji, S., & Harris, M. (1999). *In vitro* effects of therapeutic ultrasound on cell proliferation, protein synthesis, and cytokine production by human fibroblasts, osteoblasts, and monocytes. *Journal of oral and maxillofacial surgery*, 57(4), 409-419.

Donahue, N. D., Acar, H., & Wilhelm, S. (2019). Concepts of nanoparticle cellular uptake, intracellular trafficking, and kinetics in nanomedicine. *Advanced drug delivery reviews*, 143, 68-96.

Dorak, M. T., & Karpuzoglu, E. (2012). Gender differences in cancer susceptibility: an inadequately addressed issue. *Frontiers in genetics*, 3, 268. <https://doi.org/10.3389/fgene.2012.00268>

Early Breast Cancer Trialists' Collaborative Group. (2005). Effects of chemotherapy and hormonal therapy for early breast cancer on recurrence and 15-year survival: an overview of the randomised trials. *The Lancet*, 365(9472), 1687-1717.

Eda, G., Yamaguchi, H., Voiry, D., Fujita, T., Chen, M., & Chhowalla, M. (2011). Photoluminescence from chemically exfoliated MoS₂. *Nano letters*, 11(12), 5111-5116.

Emanet, M., Şen, Ö., & Çulha, M. (2017). Evaluation of boron nitride nanotubes and hexagonal boron nitrides as nanocarriers for cancer drugs. *Nanomedicine*, 12(7), 797-810.

Eruslanov, E., & Kusmartsev, S. (2010). Identification of ROS using oxidized DCFDA and flow-cytometry. *Methods in molecular biology (Clifton, N.J.)*, 594, 57-72. https://doi.org/10.1007/978-1-60761-411-1_4

Estrella, V., Chen, T., Lloyd, M., Wojtkowiak, J., Cornell, H. H., Ibrahim-Hashim, A., ... & Gillies, R. J. (2013). Acidity Generated by the Tumor Microenvironment Drives Local Invasion Acid-Mediated Invasion. *Cancer research*, 73(5), 1524-1535.

Falconi, C., Mantini, G., D'Amico, A., & Ferrari, V. (2012). Modeling of piezoelectric nanodevices. In *Piezoelectric Nanomaterials for Biomedical Applications* (pp. 93-133). Springer, Berlin, Heidelberg.

Franken, N. (2006). AP, Rodermond, H. M, Stap, J., Haveman, J., and van Bree, C, 2315-2319.

Frei, B. L., & Soefje, S. A. (2008). A review of the cardiovascular effects of oncology agents. *Journal of Pharmacy Practice*, 21(2), 146-158.

Gallardo-Williams, M. T., Chapin, R. E., King, P. E., Moser, G. J., Goldsworthy, T. L., Morrison, J. P., & Maronpot, R. R. (2004). Boron supplementation inhibits the growth and local expression of IGF-1 in human prostate adenocarcinoma (LNCaP) tumors in nude mice. *Toxicologic pathology*, 32(1), 73-78.

Gao, W., Zhao, Y., & Yin, H. (2018). Lateral size selection of liquid exfoliated hexagonal boron nitride nanosheets. *RSC advances*, 8(11), 5976-5983.

Gatenby, R. A., & Gillies, R. J. (2004). Why do cancers have high aerobic glycolysis?. *Nature reviews cancer*, 4(11), 891-899.

Gautschi, G. (2006). *Piezoelectric Sensorics: Force Strain Pressure Acceleration and Acoustic Emission Sensors Materials and Amplifiers*. Springer Science & Business Media.

Geim, A. K., & Novoselov, K. S. (2007). The rise of graphene. *Nature materials*, 6(3), 183-191.

Goldberg, E. P., Hadba, A. R., Almond, B. A., & Marotta, J. S. (2002). Intratumoral cancer chemotherapy and immunotherapy: opportunities for nonsystemic preoperative drug delivery. *Journal of Pharmacy and Pharmacology*, 54(2), 159-180.

Goldstein, L. J., Galski, H., Fojo, A., Willingham, M., Lai, S. L., Gazdar, A., ... & Pastan, I. (1989). Expression of multidrug resistance gene in human cancers. *JNCI: Journal of the National Cancer Institute*, 81(2), 116-124.

Hanahan, D., & Weinberg, R. A. (2011). Hallmarks of cancer: the next generation. *Cell*, 144(5), 646–674. <https://doi.org/10.1016/j.cell.2011.02.013>

He, Y., Qin, J., Wu, S., Yang, H., Wen, H., & Wang, Y. (2019). Cancer cell–nanomaterial interface: role of geometry and surface charge of nanocomposites in the capture efficiency and cell viability. *Biomaterials science*, 7(7), 2759-2768.

Heller, D. A., Baik, S., Eurell, T. E., & Strano, M. S. (2005). Single-walled carbon nanotube spectroscopy in live cells: towards long-term labels and optical sensors. *Advanced materials*, 17(23), 2793-2799.

Henderson, K., Stella, S. L., Kobylewski, S., & Eckhert, C. D. (2009). Receptor activated Ca(2+) release is inhibited by boric acid in prostate cancer cells. *PloS one*, 4(6), e6009. <https://doi.org/10.1371/journal.pone.0006009>

Herd, H., Daum, N., Jones, A. T., Huwer, H., Ghandehari, H., & Lehr, C. M. (2013). Nanoparticle geometry and surface orientation influence mode of cellular uptake. *ACS nano*, 7(3), 1961–1973. <https://doi.org/10.1021/nm304439f>

Hernandez, E., Goze, C., Bernier, P., & Rubio, A. (1998). Elastic properties of C and B x C y N z composite nanotubes. *Physical Review Letters*, 80(20), 4502.

Hoop, M., Chen, X. Z., Ferrari, A., Mushtaq, F., Ghazaryan, G., Tervoort, T., ... & Pané, S. (2017). Ultrasound-mediated piezoelectric differentiation of neuron-like PC12 cells on PVDF membranes. *Scientific reports*, 7(1), 1-8.

Izyumskaya, N., Demchenko, D. O., Das, S., Özgür, Ü., Avrutin, V., & Morkoç, H. (2017). Recent development of boron nitride towards electronic applications. *Advanced Electronic Materials*, 3(5), 1600485.

Jacob, K. S., Panicker, N. R., Selvam, I. P., & Kumar, V. (2003). Sol-gel synthesis of nanocrystalline PZT using a novel system. *Journal of sol-gel science and technology*, 28(3), 289-295.

Jahanban-Esfahlan, R., Seidi, K., Monhemi, H., Adli, A. D. F., Minofar, B., Zare, P., ... & Javaheri, T. (2017). RGD delivery of truncated coagulase to tumor vasculature affords local thrombotic activity to induce infarction of tumors in mice. *Scientific Reports*, 7(1), 1-14.

Janigro, D., Perju, C., Fazio, V., Hallene, K., Dini, G., Agarwal, M. K., & Cucullo, L. (2006). Alternating current electrical stimulation enhanced chemotherapy: a novel strategy to bypass multidrug resistance in tumor cells. *BMC cancer*, 6(1), 1-12.

Janigro, D., Perju, C., Fazio, V., Hallene, K., Dini, G., Agarwal, M. K., & Cucullo, L. (2006). Alternating current electrical stimulation enhanced chemotherapy: a novel strategy to bypass multidrug resistance in tumor cells. *BMC cancer*, 6(1), 1-12.

Jedrzejczak-Silicka, M., Trukawka, M., Dudziak, M., Piotrowska, K., & Mijowska, E. (2018). Hexagonal boron nitride functionalized with Au nanoparticles—properties and potential biological applications. *Nanomaterials*, 8(8), 605.

Jedrzejczak-Silicka, M., Trukawka, M., Piotrowska, K., & Mijowska, E. (2020). Few-Layered Hexagonal Boron Nitride: Functionalization, Nanocomposites, and Physicochemical and Biological Properties. In *Biochemical Toxicology-Heavy Metals and Nanomaterials*. IntechOpen.

Kabir, K. M., & Donald, W. A. (2018). Cancer breath testing: A patent review. *Expert opinion on therapeutic patents*, 28(3), 227-239.

Kallinowski, F., Schlenger, K. H., Runkel, S., Kloes, M., Stohrer, M., Okunieff, P., & Vaupel, P. (1989). Blood flow, metabolism, cellular microenvironment, and growth rate of human tumor xenografts. *Cancer research*, 49(14), 3759-3764.

Kamel, N. A. (2022). Bio-piezoelectricity: fundamentals and applications in tissue engineering and regenerative medicine. *Biophysical Reviews*, 1-17.

- Kapat, K., Shubhra, Q. T., Zhou, M., & Leeuwenburgh, S. (2020). Piezoelectric nanobiomaterials for biomedicine and tissue regeneration. *Advanced Functional Materials*, 30(44), 1909045.
- Karukstis, K. K., Thompson, E. H., Whiles, J. A., & Rosenfeld, R. J. (1998). Deciphering the fluorescence signature of daunomycin and doxorubicin. *Biophysical chemistry*, 73(3), 249-263.
- Keeney, J. T., Miriyala, S., Noel, T., Moscow, J. A., Clair, D. K. S., & Butterfield, D. A. (2015). Superoxide induces protein oxidation in plasma and TNF- α elevation in macrophage culture: Insights into mechanisms of neurotoxicity following doxorubicin chemotherapy. *Cancer letters*, 367(2), 157-161.
- Kirson, E. D., Gurvich, Z., Schneiderman, R., Dekel, E., Itzhaki, A., Wasserman, Y., ... & Palti, Y. (2004). Disruption of cancer cell replication by alternating electric fields. *Cancer research*, 64(9), 3288-3295.
- Koo, H. Y., Jeong, S. M., Cho, M. H., Chun, S., Shin, D. W., & Park, J. (2021). Population-wide impacts of aspirin, statins, and metformin use on prostate cancer incidence and mortality. *Scientific reports*, 11(1), 1-9.
- Lakshmanan, I., & Batra, S. K. (2013). Protocol for apoptosis assay by flow cytometry using annexin V staining method. *Bio-protocol*, 3(6), e374-e374.
- Lee, N. S., Yoon, C. W., Wang, Q., Moon, S., Koo, K. M., Jung, H., ... & Shung, K. K. (2020). Focused ultrasound stimulates ER localized mechanosensitive PANNEXIN-1 to mediate intracellular calcium release in invasive cancer cells. *Frontiers in cell and developmental biology*, 8, 504.
- Lejbkowicz, F., & Salzberg, S. (1997). Distinct sensitivity of normal and malignant cells to ultrasound *in vitro*. *Environmental health perspectives*, 105(suppl 6), 1575-1578.
- Lemanov, V. V., Popov, S. N., & Pankova, G. A. (2002). Piezoelectric properties of crystals of some protein aminoacids and their related compounds. *Physics of the Solid State*, 44(10), 1929-1935.
- Li, L. H., Chen, Y., Behan, G., Zhang, H., Petravic, M., & Glushenkov, A. M. (2011). Large-scale mechanical peeling of boron nitride nanosheets by low-energy ball milling. *Journal of materials chemistry*, 21(32), 11862-11866.

Li, Q., Zhang, Q., Bai, Y., Zhang, H., Hu, P., Li, Y., & Yun, F. (2021). Deep-UV hexagonal boron nitride (hBN)/BAIN distributed Bragg reflectors fabricated by RF-sputtering. *Optical Materials Express*, 11(1), 180-188.

Li, W. D., Xiao, W., Xiao, K., Berti, L., Luo, J., Tseng, H. P., ... & Lam, K. S. (2012). Reversible boronate crosslinked nanocarriers for targeted drug delivery in response to acidic pH values and cis-diols. *Angew. Chem. Int. Ed.*, 51, 2864-2869.

Li, X., Wang, X., Zhang, J., Hanagata, N., Wang, X., Weng, Q., ... & Golberg, D. (2017). Hollow boron nitride nanospheres as boron reservoir for prostate cancer treatment. *Nature communications*, 8(1), 1-12.

Liang, J., Zhang, Z., Zhao, H., Wan, S., Zhai, X., Zhou, J., ... & Lin, G. (2018). Simple and rapid monitoring of doxorubicin using streptavidin-modified microparticle-based time-resolved fluorescence immunoassay. *RSC advances*, 8(28), 15621-15631.

Lin, J., Zhang, H., Chen, Z., & Zheng, Y. (2010). Penetration of lipid membranes by gold nanoparticles: insights into cellular uptake, cytotoxicity, and their relationship. *ACS nano*, 4(9), 5421-5429.

Lippmann, G. (1881). Principe de la conservation de l'électricité, ou second principe de la théorie des phénomènes électriques. *Journal de Physique Théorique et Appliquée*, 10(1), 381-394.

Liu, C., Wu, S., Hou, L., Wang, X., Wang, L., & Shi, Y. (2014). *Zhongguo yi liao qi xie za zhi* = Chinese journal of medical instrumentation, 38(6), 433-467.

Liu, Z., Tabakman, S., Welsher, K., & Dai, H. (2009). Carbon nanotubes in biology and medicine: *in vitro* and *in vivo* detection, imaging and drug delivery. *Nano research*, 2(2), 85-120.

Lu, F., Wang, F., Gao, W., Huang, X., Zhang, X., & Li, Y. (2013). Aqueous soluble boron nitride nanosheets via anionic compound-assisted exfoliation. *Materials Express*, 3(2), 144-150.

Lu, T., Wang, L., Jiang, Y., & Huang, C. (2016). Hexagonal boron nitride nanoplates as emerging biological nanovectors and their potential applications in biomedicine. *Journal of Materials Chemistry B*, 4(36), 6103-6110.

Manocha, B., & Margaritis, A. (2008). Production and characterization of γ -polyglutamic acid nanoparticles for controlled anticancer drug release. *Critical reviews in biotechnology*, 28(2), 83-99.

Marino, A., Battaglini, M., De Pasquale, D., Degl'Innocenti, A., & Ciofani, G. (2018). Ultrasound-activated piezoelectric nanoparticles inhibit proliferation of breast cancer cells. *Scientific reports*, 8(1), 1-13.

Marino, A., Genchi, G. G., Mattoli, V., & Ciofani, G. (2017). Piezoelectric nanotransducers: The future of neural stimulation. *Nano Today*, 14, 9-12.

Marino, A., Genchi, G. G., Sinibaldi, E., & Ciofani, G. (2017). Piezoelectric effects of materials on bio-interfaces. *ACS applied materials & interfaces*, 9(21), 17663-17680.

McKinnon, K. M. (2018). Flow cytometry: an overview. *Current protocols in immunology*, 120(1), 5-1.

Mitragotri, S. (2005). Healing sound: the use of ultrasound in drug delivery and other therapeutic applications. *Nature reviews Drug discovery*, 4(3), 255-260.

Mittelstein, D. R., Ye, J., Schibber, E. F., Roychoudhury, A., Martinez, L. T., Fekrazad, M. H., ... & Gharib, M. (2020). Selective ablation of cancer cells with low intensity pulsed ultrasound. *Applied Physics Letters*, 116(1), 013701.

Mo, S., Coussios, C. C., Seymour, L., & Carlisle, R. (2012). Ultrasound-enhanced drug delivery for cancer. *Expert opinion on drug delivery*, 9(12), 1525-1538.

Mokhtari, F., Azimi, B., Salehi, M., Hashemikia, S., & Danti, S. (2021). Recent advances of polymer-based piezoelectric composites for biomedical applications. *Journal of the Mechanical Behavior of Biomedical Materials*, 122, 104669.

Moon, O. M., Kang, B. C., Lee, S. B., & Boo, J. H. (2004). Temperature effect on structural properties of boron oxide thin films deposited by MOCVD method. *Thin Solid Films*, 464, 164-169.

Moon, O. M., Kang, B. C., Lee, S. B., & Boo, J. H. (2004). Temperature effect on structural properties of boron oxide thin films deposited by MOCVD method. *Thin Solid Films*, 464, 164-169.

Mun, E. J., Babiker, H. M., Weinberg, U., Kirson, E. D., & Von Hoff, D. D. (2018). Tumor-Treating Fields: A Fourth Modality in Cancer Treatment. *Clinical Cancer Research*, 24(2), 266-275.

Nangia, S., & Sureshkumar, R. (2012). Effects of nanoparticle charge and shape anisotropy on translocation through cell membranes. *Langmuir : the ACS journal of surfaces and colloids*, 28(51), 17666–17671. <https://doi.org/10.1021/la303449d>

Ng, N. S., & Ooi, L. (2021). A Simple Microplate Assay for Reactive Oxygen Species Generation and Rapid Cellular Protein Normalization. *Bio-protocol*, 11(1), e3877. <https://doi.org/10.21769/BioProtoc.3877>

O'Brien Jr, W. D. (2007). Ultrasound–biophysics mechanisms. *Progress in biophysics and molecular biology*, 93(1-3), 212-255.

Pacile, D., Meyer, J. C., Girit, Ç. Ö., & Zettl, A. J. A. P. L. (2008). The two-dimensional phase of boron nitride: Few-atomic-layer sheets and suspended membranes. *Applied Physics Letters*, 92(13), 133107.

Popova, V., Poletaeva, Y., Pyshnaya, I., Pyshnyi, D., & Dmitrienko, E. (2021). Designing pH-Dependent Systems Based on Nanoscale Calcium Carbonate for the Delivery of an Antitumor Drug. *Nanomaterials*, 11(11), 2794.

Puvvada, N., Rajput, S., Kumar, B. N., Sarkar, S., Konar, S., Brunt, K. R., ... & Pathak, A. (2015). Novel ZnO hollow-nanocarriers containing paclitaxel targeting folate-receptors in a malignant pH-microenvironment for effective monitoring and promoting breast tumor regression. *Scientific reports*, 5(1), 1-15.

Qian, L., Huang, Y., Spencer, C. I., Foley, A., Vedantham, V., Liu, L., ... & Srivastava, D. (2012). In vivo reprogramming of murine cardiac fibroblasts into induced cardiomyocytes. *Nature*, 485(7400), 593-598.

Rajabi, A. H., Jaffe, M., & Arinze, T. L. (2015). Piezoelectric materials for tissue regeneration: A review. *Acta biomaterialia*, 24, 12–23. <https://doi.org/10.1016/j.actbio.2015.07.010>

Rawla, P. (2019). Epidemiology of prostate cancer. *World journal of oncology*, 10(2), 63. Reinišová, L., Hermanová, S., & Pumera, M. (2019). Micro/nanomachines: what is needed for them to become a real force in cancer therapy?. *Nanoscale*, 11(14), 6519-6532.

Rejman, J., Oberle, V., Zuhorn, I. S., & Hoekstra, D. (2004). Size-dependent internalization of particles via the pathways of clathrin-and caveolae-mediated endocytosis. *Biochemical journal*, 377(1), 159-169.

Rondanelli, M., Faliva, M. A., Peroni, G., Infantino, V., Gasparri, C., Iannello, G., ... & Tartara, A. (2020). Pivotal role of boron supplementation on bone health: A narrative review. *Journal of Trace Elements in Medicine and Biology*, 62, 126577.

Roy, S., Zhang, X., Puthirath, A. B., Meiyazhagan, A., Bhattacharyya, S., Rahman, M. M., ... & Ajayan, P. M. (2021). Structure, Properties and Applications of Two-Dimensional Hexagonal Boron Nitride. *Advanced Materials*, 33(44), 2101589.

Sahay, G., & Alakhova, D. Y. (2010). V Kabanov A. Endocytosis of nanomedicines, *J. Control. Release*, 145, 182-195.

Sajid, A., Ford, M. J., & Reimers, J. R. (2020). Single-photon emitters in hexagonal boron nitride: a review of progress. *Reports on Progress in Physics*, 83(4), 044501.

Salim, M., Salim, D., Chandran, D., Aljibori, H. S., & Kherbeet, A. S. (2018). Review of nano piezoelectric devices in biomedicine applications. *Journal of Intelligent Material Systems and Structures*, 29(10), 2105-2121.

Sammon, A. M., Ndebia, E. J., Umapathy, E., & Iputo, J. E. (2015). 24-Hour Measurement of Gastric pH in Rural South Africa. *Gastroenterology research and practice*, 2015, 658106. <https://doi.org/10.1155/2015/658106>

Şen, Ö., Emanet, M., & Çulha, M. (2018). One-step synthesis of hexagonal boron nitrides, their crystallinity and biodegradation. *Frontiers in bioengineering and biotechnology*, 6, 83.

Sena, K., Leven, R. M., Mazhar, K., Sumner, D. R., & Viridi, A. S. (2005). Early gene response to low-intensity pulsed ultrasound in rat osteoblastic cells. *Ultrasound in medicine & biology*, 31(5), 703-708.

Sersa, G., Kotnik, V., Cemažar, M., Miklavcic, D., & Kotnik, A. (1996). Electrochemotherapy with bleomycin in SA-1 tumor-bearing mice—natural resistance and immune responsiveness. *Anti-Cancer Drugs*, 7(7), 785-791.

Shamos, M. H., & Lavine, L. S. (1967). Piezoelectricity as a fundamental property of biological tissues. *Nature*, 213(5073), 267-269.

Shi, Y., Hamsen, C., Jia, X., Kim, K. K., Reina, A., Hofmann, M., ... & Kong, J. (2010). Synthesis of few-layer hexagonal boron nitride thin film by chemical vapor deposition. *Nano letters*, 10(10), 4134-4139.

Shuai, C., Liu, G., Yang, Y., Qi, F., Peng, S., Yang, W., ... & Qian, G. (2020). A strawberry-like Ag-decorated barium titanate enhances piezoelectric and antibacterial activities of polymer scaffold. *Nano Energy*, 74, 104825.

Siegel, R. L., Miller, K. D., & Jemal, A. (2019). Cancer statistics, 2019. *CA: a cancer journal for clinicians*, 69(1), 7-34.

Sohaebuddin, S. K., Thevenot, P. T., Baker, D., Eaton, J. W., & Tang, L. (2010). Nanomaterial cytotoxicity is composition, size, and cell type dependent. *Particle and fibre toxicology*, 7(1), 1-17.

SreeHarsha, N., Maheshwari, R., Al-Dhubiab, B. E., Tekade, M., Sharma, M. C., Venugopala, K. N., & Alzahrani, A. M. (2019). Graphene-based hybrid nanoparticle of doxorubicin for cancer chemotherapy. *International journal of nanomedicine*, 14, 7419.

Stupp, R., Taillibert, S., Kanner, A. A., Kesari, S., Steinberg, D. M., Toms, S. A., ... & Ram, Z. (2015). Maintenance therapy with tumor-treating fields plus temozolomide vs temozolomide alone for glioblastoma: a randomized clinical trial. *Jama*, 314(23), 2535-2543.

Su, L., Zou, L., Fong, C. C., Wong, W. L., Wei, F., Wong, K. Y., ... & Yang, M. (2013). Detection of cancer biomarkers by piezoelectric biosensor using PZT ceramic resonator as the transducer. *Biosensors and Bioelectronics*, 46, 155-161.

Sun, D., Chen, Z., Wu, M., & Zhang, Y. (2017). Nanomaterial-based microfluidic chips for the capture and detection of circulating tumor cells. *Nanotheranostics*, 1(4), 389.

Swiech, O., Majdecki, M., Opuchlik, L. J., & Bilewicz, R. (2020). Impact of pH and cell medium on the interaction of doxorubicin with lipoic acid cyclodextrin conjugate as the drug carrier. *Journal of Inclusion Phenomena and Macrocyclic Chemistry*, 97(1), 129-136.

Swietach, P., Vaughan-Jones, R. D., Harris, A. L., & Hulikova, A. (2014). The chemistry, physiology and pathology of pH in cancer. *Philosophical Transactions of the Royal Society B: Biological Sciences*, 369(1638), 20130099.

Taskin, I. C., Sen, O., Emanet, M., Culha, M., & Yilmaz, B. (2020). Hexagonal boron nitrides reduce the oxidative stress on cells. *Nanotechnology*, 31(21), 215101.

Ter Haar, G., & Coussios, C. (2007). High intensity focused ultrasound: physical principles and devices. *International journal of hyperthermia*, 23(2), 89-104.

Tian, L., & Bae, Y. H. (2012). Cancer nanomedicines targeting tumor extracellular pH. *Colloids and Surfaces B: Biointerfaces*, 99, 116-126.

Torchilin, V. P. (2010). Passive and active drug targeting: drug delivery to tumors as an example. *Drug delivery*, 3-53.

Uršič, H., & Prah, U. (2019). Investigations of ferroelectric polycrystalline bulks and thick films using piezoresponse force microscopy. *Proceedings of the Royal Society A*, 475(2223), 20180782.

Vaupel, P., Kallinowski, F., & Okunieff, P. (1989). Blood flow, oxygen and nutrient supply, and metabolic microenvironment of human tumors: a review. *Cancer research*, 49(23), 6449-6465.

Vercauteren, D., Vandembroucke, R. E., Jones, A. T., Rejman, J., Demeester, J., De Smedt, S. C., ... & Braeckmans, K. (2010). The use of inhibitors to study endocytic pathways of gene carriers: optimization and pitfalls. *Molecular Therapy*, 18(3), 561-569.

Wang, G., Zhao, D., Spring, D. J., & DePinho, R. A. (2018). Genetics and biology of prostate cancer. *Genes & development*, 32(17-18), 1105-1140.

Wang, Y., Cai, R., & Chen, C. (2019). The nano-bio interactions of nanomedicines: Understanding the biochemical driving forces and redox reactions. *Accounts of chemical research*, 52(6), 1507-1518.

Wang, Z. L. (2004). Nanostructures of zinc oxide. *Materials today*, 7(6), 26-33.

Watanabe, K., Taniguchi, T., & Kanda, H. (2004). Direct-bandgap properties and evidence for ultraviolet lasing of hexagonal boron nitride single crystal. *Nature materials*, 3(6), 404-409.

Yang, K., Feng, L., & Liu, Z. (2016). Stimuli responsive drug delivery systems based on nano-graphene for cancer therapy. *Advanced drug delivery reviews*, 105, 228-241.

Yao, H. C., Xu, E. J., Zeng, W. Y., Zeng, X. Y., Zhang, M., & Chen, J. (2013). Determination of doxorubicin in pharmaceutical preparation and rat plasma with luminol-K₃Fe (CN)₆ chemiluminescence system. *Journal of food and drug analysis*, 21(3), 279-285.

Ysiwata-Rivera, A. P., Hernández-Hernández, E., Cadenas-Pliego, G., Ávila-Orta, C. A., González-Morones, P., Velásquez-de Jesús, J. A., ... & Mata-Padilla, J. M. (2020). Effect of modified hexagonal boron nitride nanoparticles on the emulsion stability, viscosity and electrochemical behavior of nanostructured acrylic coatings for the corrosion protection of AISI 304 stainless steel. *Coatings*, 10(5), 488.

Yu, T., Wang, Z., & Mason, T. J. (2004). A review of research into the uses of low level ultrasound in cancer therapy. *Ultrasonics sonochemistry*, 11(2), 95-103.

Zhang, C., Fu, L., Zhao, S., Zhou, Y., Peng, H., & Liu, Z. (2013). Controllable Co-segregation Synthesis of Wafer-Scale Hexagonal Boron Nitride Thin Films. *Advanced Materials*, 26(11), 1776–1781. doi:10.1002/adma.201304301

Zhang, J., Tan, B., Zhang, X., Gao, F., Hu, Y., Wang, L., ... & Hu, P. (2021). Atomically thin hexagonal boron nitride and its heterostructures. *Advanced Materials*, 33(6), 2000769.

Zhang, L., Xia, J., Zhao, Q., Liu, L., & Zhang, Z. (2010). Functional graphene oxide as a nanocarrier for controlled loading and targeted delivery of mixed anticancer drugs. *small*, 6(4), 537-544.

Zhang, S., Lian, G., Si, H., Wang, J., Zhang, X., Wang, Q., & Cui, D. (2013). Ultrathin BN nanosheets with zigzag edge: one-step chemical synthesis, applications in wastewater treatment and preparation of highly thermal-conductive BN–polymer composites. *Journal of Materials Chemistry A*, 1(16), 5105-5112.

Zhang, Z. F., Winton, M. I., Rainey, C., & Eckhart, C. D. (2001). Boron is associated with decreased risk of human prostate cancer. In *Faseb Journal* (Vol. 15, No. 5, pp. A1089-A1089). 9650 Rockville Pike, Bethesda, Md 20814-3998 Usa: Federation Amer Soc Exp Biol.

Zhang, Z. J., Huckle, J., Francomano, C. A., & Spencer, R. G. (2003). The effects of pulsed low-intensity ultrasound on chondrocyte viability, proliferation, gene expression and matrix production. *Ultrasound in medicine & biology*, 29(11), 1645-1651.

Zhi, C., Bando, Y., Tang, C., & Golberg, D. (2010). Boron nitride nanotubes. *Materials Science and Engineering: R: Reports*, 70(3-6), 92-111.

Zhi, C., Bando, Y., Tang, C., Kuwahara, H., & Golberg, D. (2009). Large-scale fabrication of boron nitride nanosheets and their utilization in polymeric composites with improved thermal and mechanical properties. *Advanced Materials*, 21(28), 2889-2893.

Zhou, S., Schmelz, A., Seufferlein, T., Li, Y., Zhao, J., & Bachem, M. G. (2004). Molecular mechanisms of low intensity pulsed ultrasound in human skin fibroblasts. *Journal of Biological Chemistry*, 279(52), 54463-54469.

Zhu, L., Lian, G., Tan, M., Wang, Q., Zhao, X., Cui, D., & Tao, X. (2008). Reaction of hexagonal boron nitride nano-crystals under mild hydrothermal conditions. *Zeitschrift für Naturforschung B*, 63(6), 742-746.

